Advancements in Photochemistry and Flow Systems for Synthesis and Analysis

Mahzad Yaghmaei Sabegh

Thesis submitted to the University of Ottawa
in partial fulfillment of the requirements for the degree of
Doctor of Philosophy in Chemistry

Department of Chemistry and Biomolecular Sciences
Faculty of Science
University of Ottawa

Supervisor: Juan (Tito) Scaiano

Abstract

This dissertation explores the integration of photochemistry with flow systems, demonstrating significant advancements in organic synthesis, nanomaterial production, and quantitative analysis. The research encompasses four key areas: reduction of nitro compounds with a heterogeneous catalyst in a flow system, development of a flow actinometer, scalable synthesis of silver nanoparticles (AgNPs) in flow, and selective semi-oxidation of tetrahydroisoquinoline (THIQ).

The second chapter investigates the catalytic reduction of nitro compounds to amines using palladium nanoparticles supported on glass wool (Pd@GW) under flow conditions. This work demonstrates the potential of heterogeneous catalysis in flow systems for efficient and selective organic transformations, highlighting the advantages of continuous-flow processes in terms of reaction control and scalability.

The third chapter addresses a critical gap in flow photochemistry by developing a simple Norrish Type II actinometer based on valerophenone photochemistry. This tool enables accurate measurement of light absorption in flow systems, a parameter often overlooked in photochemical reactions. The actinometer's design allows for easy implementation in organic chemistry laboratories, facilitating more rigorous and comparable studies in flow photochemistry.

The fourth chapter focuses on the scalable synthesis of AgNPs using flow photochemistry. Various Norrish Type I photoinitiators are evaluated for their efficiency in reducing silver ions to nanoparticles. The flow system allows for rapid, continuous production of AgNPs with controlled size and morphology, demonstrating the potential for industrial-scale synthesis of nanomaterials through photochemical methods.

In the fifth chapter, the selective oxidation of THIQ to dihydroisoquinoline (DHIQ) is achieved through a singlet oxygen-mediated process. Utilizing both homogeneous ($Ru(bpy)_3Cl_2$) and heterogeneous (RuB@GW, MoCo@GW) catalysts, the reaction demonstrates exceptional selectivity due to the vastly different singlet oxygen quenching rates of THIQ and DHIQ. The use of glass wool-supported catalysts facilitates easy separation and reusability while being compatible with flow systems.

Collectively, these studies display the synergistic benefits of combining photochemistry with flow systems and heterogeneous catalysis. They demonstrate improved reaction efficiency, enhanced control over reaction parameters, and potential for scalability across various chemical processes. The use of visible light, recyclable catalysts, and in some cases molecular oxygen as an oxidant aligns with green chemistry principles. These advancements open new pathways for more sustainable and efficient chemical manufacturing processes, from organic molecule synthesis to nanomaterial production.

Acknowledgements

The completion of this thesis would not have been possible without the support and guidance of numerous individuals to whom I am deeply thankful.

First and foremost, I wish to express my deep gratitude to my supervisor, professor Tito Scaiano, for his invaluable mentorship throughout my doctoral studies. His decision to welcome me into his research group has been life changing. His insightful guidance, constant support, and encouragement to explore diverse topics and learn various instruments have been key in shaping both my academic journey and personal growth. The lessons learned extend far beyond the realm of photochemistry, including valuable life experiences that I will carry forward. I loved listening to his stories - they were always fun and full of good advice. Thank you so much for everything you have done for me.

I am deeply appreciative of the research assistants in our group, particularly Anabel Lanterna, whose initial guidance was crucial in helping me establish a strong foundation in experimental techniques, data analysis, and attention to detail. The collective help of assistants Neeraj Joshi, Bowen Wang, and Betty Yakimenko has been invaluable in overcoming research challenges and speeding up progress.

My heartfelt thanks go to my colleagues in the Scaiano group. Our diverse backgrounds, representing various cultures, and regions across the world, have created a blend of experiences. I learned something valuable from each of them. Special thanks to my close friends Melissa, Daliane, and Saba, whose friendship made this journey particularly memorable. The shared experiences, both academic and personal, have created a supportive environment that has been crucial to my progress and well-being throughout these years as an international student.

I owe much gratitude to my family, especially my parents, for their steady care and encouragement. They taught me to brainstorm and seek answers and encouraged me to pursue my dreams. Their understanding and support of my decision to pursue studies far from home have been a source of strength throughout this journey. I am also deeply thankful to my siblings, Hamed and Mahsa, whose unwavering encouragement and support have meant so much to me along the way.

I am grateful to my cousins, Nasseh and Maryam, in Ottawa, whose help eased my transition to life in a new country. Their efforts in helping me adapt to a new environment by weekend invitations, preparation of traditional foods, and celebration of our shared cultural feasts helped reduce the challenges of immigration and homesickness.

Finally, I wish to express my heartfelt appreciation to my husband, Farshad, my constant listener and confidant. Sharing all my moments - good and bad, ups and downs, concerns and joys - with him has been a source of great comfort. His support, positivity, and dedication to helping me achieve my dreams and succeed have been priceless.

This work stands as proof of the collective support, guidance, and inspiration provided by all those mentioned above, as well as many others who have contributed in various ways. Their impact on both this thesis and my personal development cannot be overstated.

Contribution Statement

The research presented in this dissertation, conducted in fulfillment of the requirements for the degree of Doctor of Philosophy, was carried out under the supervision of Professor Tito Scaiano. The entirety of this work would not have been possible without Professor Scaiano's exceptional guidance and support throughout my doctoral journey.

This thesis is based on four peer-reviewed publications, for all of which I served as the first contributing author. Most of the experimental work across all chapters was completed by me, with all research performed in close consultation with Professor Scaiano.

Dr. Anabel Lanterna, former research associate in the Scaiano group, provided valuable guidance for the research reported in Chapters 2 and 5. Her insights significantly contributed to the depth and breadth of these studies.

In Chapters 2 and 3, I exclusively conducted all experimental work. Chapter 4 involved a collaborative approach: my colleague Connor R. Bourgonje conducted batch experiments, which were needed to set the controlled reaction conditions, while I performed flow experiments that allowed us to test the process in a manner suitable for potential industrial scale-up.

For Chapter 5, all experimental results presented were exclusively conducted by me under the direct supervision of Professor Tito Scaiano and with the additional guidance of Dr. Anabel Lanterna. The research in this chapter built upon initial work in the project, benefiting from the foundational efforts of earlier contributors.

List of Publications

Publications presented in this thesis:

Chapter 2:

Yaghmaei, Mahzad, Anabel E. Lanterna, and Juan C. Scaiano. "Nitro to amine reductions using aqueous flow catalysis under ambient conditions." Iscience 24, no. 12 (2021).

Scaiano, Juan C., Bowen Wang, Connor R. Bourgonje, and Mahzad Yaghmaei. "The nitro to amine reduction: from millions of tons to single molecule studies." Pure and Applied Chemistry 95, no. 8 (2023): 913-920.

Chapter 3:

Yaghmaei, Mahzad, and Juan C. Scaiano. "A simple Norrish Type II actinometer for flow photoreactions." Photochemical & Photobiological Sciences 22, no. 8 (2023): 1865-1874.

Chapter 4:

Yaghmaei, Mahzad, Connor R. Bourgonje, and Juan C. Scaiano. "Facile scale-up of the flow synthesis of silver nanostructures based on Norrish type I photoinitiators." Molecules 28, no. 11 (2023): 4445.

Chapter 5:

Yaghmaei, Mahzad, Martin Villanueva, Iris Martín-García, Francisco Alonso, Xiaocong Zhang, Neeraj Joshi, Anabel E. Lanterna, and Juan C. Scaiano. "Photosensitized selective semi-oxidation of tetrahydroisoquinoline: a singlet oxygen path." Photochemical & Photobiological Sciences 21, no. 8 (2022): 1473-1479.

Publications not discussed in this thesis:

Yaghmaei, Mahzad, Daliane RC da Silva, Nelson Rutajoga, Sara Currie, Yiran Li, Morgan Vallieres, Jasmin M Silvero, Neeraj Joshi, Bowen Wang, and Juan C. Scaiano, 2024. Innovative Black TiO_2 Photocatalyst for Effective Water Remediation Under Visible Light Illumination Using Flow Systems. Catalysts. 14(11):775.

Carly J. Frank, Connor R. Bourgonje, Mahzad Yaghmaei and Juan C. Scaiano. "Color-coordinated approach to the flow synthesis of silver nanoparticles with custom morphologies". This paper is submitted in Nanoscale Advances, 2024.

Table of Contents

List of Figures

List of Tables

List of Schemes

List of abbreviations

AcN	Acetonitrile
ACP	Acetophenone
APIs	Active Pharmaceutical Ingredients
APTES	3-Aminopropyltriethoxysilane CNB
CNFs	Carbon nanofibers
DHIQ	Dihydroisoquinoline
EDS	Energy dispersive spectrometer
EDX	Energy dispersive X-ray spectroscopy
FWHM	Full width at half maximum
GC	Gas chromatography
GC-MS	Gas chromatography-mass spectrometry
GW	glass wool
HR-XPS	High-Resolution X-ray photoelectron spectroscopy
IC	Internal Conversion
ICP-OES	Inductively Coupled Plasma Optical Emission Spectroscopy
ID	Internal diameter
INT	Integer function
IQ	Isoquinoline
IR	Infrared
ISC	Intersystem Crossing
LED	Light-emitting diode

LEDi-HBL	LEDi 450 nm
LFP	Laser flash photolysis
MDI	Methylene diphenyl diisocyanate
MeBenzoin	Alpha-methyl-benzoin phenyl ether
MeCN	Acetonitrile
MeOH	Methanol
MLCT	metal-to-ligand charge transfer
MOFs	Metal-organic frameworks
NB	Nitrobenzene
Nd-YAG	Neodymium-doped yttrium aluminum garnet; Nd:$Y_3Al_5O_{12}$
NINT	Nearest integer function
NIR	Near-Infrared
NMR	Nuclear magnetic resonance
NPs	Nano particles
OD	Outside diameter
PCET	Proton-coupled electron transfer reactions
SEM	Scanning electron microscopy
SET	Single electron transfer
SI	Supplementary information
STY	Space time yield
TCD	Thermal conductivity detectors
TEM	Transmission electron microscopy
THF	Tetrahydrofuran

THIQ	Tetrahydroisoquinoline
THQ	Tetrahydroquinolines
UV	Ultraviolet
UV-Vis	Ultraviolet- visible
XPS	X-ray Photoelectron spectroscopy
XRD	X-ray diffraction

Chapter 1. Introduction

1.1 Opening remark

This dissertation explores the increasing importance of flow methods in modern chemistry, especially in discovering new reactions, developing methods, scaling up processes, production, and fast screening and optimization. The growing field of photochemical processes has gained a lot of attention in the scientific community, and the recent use of flow methods in these processes shows the many benefits of flow chemistry. This integration highlights its vital role in advancing chemistry and technology worldwide.

The thesis is structured around four peer-reviewed publications, which form the core of Chapters 2-5. Each chapter presents the original manuscripts and supporting information, supplemented with additional commentary and modifications. The introductory chapter serves as a foundation, helping readers with essential background knowledge and setting the stage for the subsequent chapters. It also highlights key advancements in the photochemistry process, heterogeneous photocatalysts, singlet oxygen, and flow photochemistry.

1.2 Photochemistry and photocatalysis

In recent decades, synthetic organic chemistry has undergone significant changes, with light-driven processes gaining prominence in the creation of important molecules, including pharmaceuticals, agrochemicals, and materials. This growing interest in photochemistry and photocatalysis stems from the new possibilities they offer and their favorable reaction conditions. Key advantages include the use of visible light, the elimination of hazardous redox reagents, and the ability to perform reactions at room temperature, making these methods both efficient and environmentally friendly.[1]

Photochemistry focuses on chemical reactions, processes, and mechanisms initiated by the absorption of light. When molecules absorb photons, they become excited to higher energy states, potentially leading to various chemical transformations in competition with their return to their ground state. Light-induced chemical reactions are fundamental to many natural and artificial processes, including photosynthesis in plants, vision, and the synthesis of vitamin D in

humans. In industrial applications, photochemistry is utilized in areas such as the development of new materials, photodynamic therapy for cancer treatment, and the utilization of solar energy.[2,3]

The absorption of a photon by a molecule initiates a series of photophysical processes, which can be visualized using a Jablonski diagram (Figure 1.1). Named after Polish physicist Alexander Jablonski, this diagram illustrates the various electronic states of a molecule and the transitions between them.[4] The key processes involved in photoexcitation and relaxation are:

1. Absorption: The molecule absorbs a photon, promoting an electron from the ground state (S_0) to an excited singlet state (S_1, S_2, etc.). This process occurs on an extremely fast timescale, typically 10^{-15} seconds.[5]

2. Internal Conversion (IC): This non-radiative transition occurs between electronic states of the same spin multiplicity (e.g., S_2 to S_1). It happens rapidly, usually within 10^{-12} to 10^{-10} seconds, and is often followed by vibrational relaxation to the lowest vibrational level of the lower electronic state.[6]

3. Fluorescence: This radiative transition from the lowest excited singlet state (S_1) back to the ground state (S_0) typically occurs on a timescale of 10^{-9} to 10^{-7} seconds. It results in the emission of a photon with lower energy (longer wavelength) than the absorbed photon due to energy loss through vibrational relaxation.[7]

4. Intersystem Crossing (ISC): This non-radiative transition occurs between electronic states of different spin multiplicity, typically from an excited singlet state (S_1) to a triplet state (T_1). ISC is generally slower than internal conversion, occurring on a timescale of 10^{-8} to 10^{-3} seconds.[8]

5. Phosphorescence: This radiative transition from the lowest triplet state (T_1) back to the ground state (S_0) is spin-forbidden, making phosphorescence much slower than fluorescence, with lifetimes ranging from microseconds to seconds or even longer.[9]

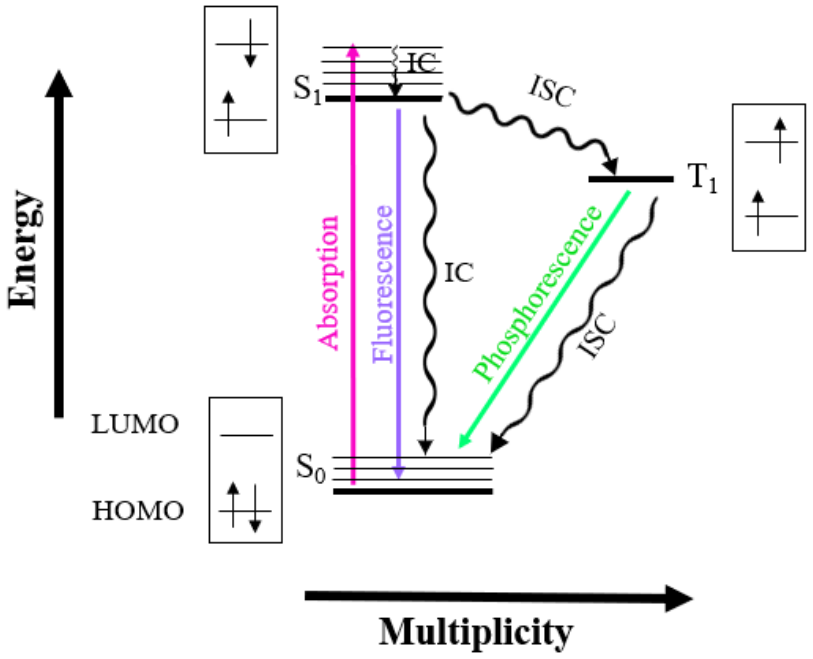

Figure 1.1. Jablonski diagram alongside the orbital occupancy and energy levels

Understanding these photophysical processes is crucial in photochemistry and photocatalysis, as they determine the fate of excited molecules and the pathways available for chemical reactions. For instance, longer-lived excited states (such as triplet states) often play key roles in photocatalytic reactions due to their increased probability of interacting with other molecules before relaxing back to the ground state.[10,11]

The first law of photochemistry, also known as the Grotthuss-Draper law, states that only absorbed photons can initiate a photochemical process.[12] This principle is fundamental to the activation of photocatalysts, which are typically activated by absorbing UV or visible light, depending on their electronic structure. In semiconductor photocatalysts, this excitation promotes electrons from the valence band to the conduction band, creating electron-hole pairs.[13] For molecular photocatalysts, such as metal complexes or organic dyes, the excitation often involves transitions between molecular orbitals.[14]

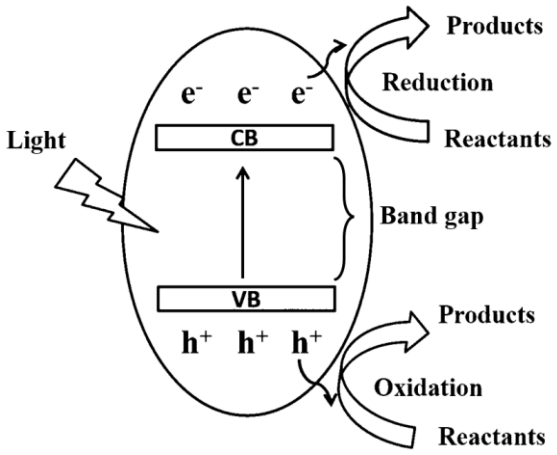

Figure 1.2. Illustration of a photocatalytic process on a semiconductor photocatalyst initiated by light absorption

The efficiency of photocatalyst activation depends on several factors, including the light absorption coefficient, quantum yield, charge carrier lifetime, and charge separation and migration efficiency.[15] Strategies such as doping, creating heterojunctions, and surface modifications aim to enhance light absorption, extend the usable light spectrum, and improve charge separation, ultimately leading to more effective photocatalytic systems.[16]

Semiconductor photocatalysts are among the most widely studied and utilized. Titanium dioxide (TiO_2) is the classic example, known for its high stability, low cost, and effectiveness in environmental remediation and water splitting.[17] Other semiconductor photocatalysts include zinc oxide (ZnO), cadmium sulphide (CdS), and tungsten trioxide (WO_3). These materials generate electron-hole pairs upon light absorption, which can then participate in redox reactions at the catalyst surface.[18]

Metal-based photocatalysts form another important category. Palladium (Pd), platinum (Pt), and gold (Au) nanoparticles exhibit plasmonic effects, enhancing light absorption and charge separation when combined with semiconductors.[19] These noble metals are particularly effective in hydrogenation reactions and C-C coupling. Transition metal oxides, such as iron oxides and cobalt oxides, also show promising photocatalytic activity, especially in water oxidation reactions.[20]

Organic photocatalysts have gained significant attention in recent years. These include organic dyes like Eosin Y and Rose Bengal, as well as more complex structures such as graphitic

carbon nitride (g-C_3N_4).[21] Organic photocatalysts often offer advantages in visible light absorption and can be easily tuned through structural modifications.

Metal-organic frameworks (MOFs) represent a unique class of photocatalysts that bridge the gap between homogeneous and heterogeneous systems. These highly porous materials combine metal nodes with organic linkers, offering significant structural versatility and high surface areas.[22] MOFs have shown promise in applications ranging from CO_2 reduction to organic transformations.

Composite photocatalysts combine two or more materials to overcome the limitations of individual components. For instance, graphene-TiO_2 composites show enhanced charge separation and increased adsorption of organic pollutants.[23] Similarly, Z-scheme systems mimic natural photosynthesis by coupling two semiconductors to achieve wider light absorption and more efficient charge separation. In a Z-scheme system, two different semiconductors with complementary band structures are combined, allowing for spatial separation of photogenerated electrons and holes. This arrangement enables the system to maintain strong redox capabilities while utilizing a broader spectrum of light, thus potentially improving overall photocatalytic efficiency.[24]

Quantum dots, such as CdS and CdSe nanocrystals, represent another emerging class of photocatalysts. Their size-dependent optical and electronic properties allow for fine-tuning of band gaps and redox potentials.[25]

Lastly, biohybrid photocatalysts integrate biological components, such as enzymes or whole cells, with synthetic materials. These systems aim to combine the selectivity of biological catalysts with the robustness of inorganic materials.[26]

Each type of photocatalyst offers unique advantages and faces distinct challenges. Ongoing research focuses on improving visible light absorption, enhancing charge separation efficiency, and increasing stability and reusability. The diverse landscape of photocatalysts provides a rich toolbox for addressing a wide range of applications, from environmental remediation to solar fuel production and fine chemical synthesis.

1.2.1 Heterogeneous catalysts

Catalysts are classified into two main categories based on the phase of the catalyst, heterogeneous and homogeneous. Homogeneous photocatalysts are in the same phase as the reactants, usually dissolved in a solution. Examples include metal complexes like $Ru(bpy)_3^{2+}$ and organic dyes. Although homogeneous catalysts offer advantages such as uniform reaction environments and faster reaction rates due to better molecular interaction, they often pose challenges in separation and reuse, which can limit their practical applications.[27]

In contrast, heterogeneous photocatalysis involves catalysts that are in a different phase than the reactants, usually a solid catalyst in contact with liquid or gaseous reactants. Heterogeneous photocatalysts are widely favored in industrial applications due to their ease of separation, reusability, and stability. Common examples include titanium dioxide (TiO_2), zinc oxide (ZnO), and various metal-loaded materials. These catalysts can be easily recovered from the reaction mixture by filtration or centrifugation, making the process more sustainable and economically viable.[28]

The supports for heterogeneous catalysts can be categorized into two main types based on their physical form and handling characteristics: powder and fibrous. Powder supports typically consist of fine particles or granules, such as metal oxides, activated carbon, and zeolites. They often provide high surface areas but can be challenging to separate from reaction mixtures. Fibrous supports, on the other hand, are composed of long, thin fibers or filaments, like glass wool, carbon fibers, or polymer fibers. These supports offer easier handling and separation and show potential for use in flow chemistry applications.[29]

In recent decades, the development of various supported nanoparticles has been an active area of research, aiming to enhance the reactivity, recoverability, and selectivity of heterogeneous catalysts. For example in the field of reduction of nitro compounds a breakthrough in selective nitro group reduction using nanoparticle catalysts was achieved in 2006.[30] They demonstrated that gold nanoparticles, when supported on TiO_2 or Fe_2O_3, could selectively reduce functionalized nitroarenes under the reaction conditions (9 bar, 120°C) without producing hazardous hydroxylamine intermediates. Another research came in 2008 and introduced a new heterogeneous catalyst consisting of palladium (0) stabilized by nanocrystalline magnesium oxide. This catalyst, synthesized from commercial NAP−Mg−$PdCl_4$. The reaction

was done in THF as a solvent through a two-step process with quantitative yield in few hourse of reaction time.[31] The catalyst could be recovered by filtration and reused multiple times. Researchers developed an alternative catalytic system using platinum and palladium nanoparticles supported on carbon nanofibers (CNFs) for nitroarene reduction. The system reduced halogen-substituted nitroarenes in 3 to 10 atm H_2 and 50 °C with high yields and selectivity in 2-4 h reaction time, while also showing chemoselectivity by reducing nitro groups without affecting terminal alkenes, nitriles, amides, esters, and benzylic alcohols. The catalyst's effectiveness was found to depend on the graphite layer orientation in the support material, with perpendicular (CNF-P) and stacked oblique (CNF-H) arrangements providing optimal results.[32]

In a separate development, a heterogeneous hydrogenation catalyst was created using Pd(0) nanoparticles stabilized on polyphenol-grafted collagen fibers. While this catalyst showed improved activity compared to traditional catalysts supported on inorganic materials, its selectivity was limited. This limitation was particularly evident in the reduction of 4-nitrochlorobenzene, which only achieved a modest 48% yield.[33]

Another research in this field developed a novel iron-based catalyst. Their catalyst consisted of Fe_2O_3 prepared through controlled pyrolysis of iron-phenanthroline (Fe-Phen) complexes supported on carbon. This catalytic system demonstrated versatility in reducing a broad range of nitroarenes with the reaction condition of 50 bar H_2, 120 °C, the mix of H_2O and THF as a solvent, and 12 to 24 h reaction time with yields ranging from 86% to 99%. The formation of FeN_X centers occurs during the catalyst synthesis when Fe-Phen complexes undergo pyrolysis on the carbon support. These critical active centers only form at temperatures of 800°C and are essential for catalytic activity - the carbon-supported material shows no catalytic activity without this pyrolysis step. The researchers found that nanoparticle size played an important role in relation to these generated active centers.[34]

Glass wool offers a combination of high surface area, chemical inertness, thermal stability, inexpensive, flexible shaping and adaptation to various reactor designs, and potential for flow chemistry applications which can be beneficial in laboratory-scale experiments or specialized industrial applications.[35] However, glass wool does have limitations as a catalyst support. It lacks the additional functional properties often provided by supports like metal oxides or zeolites, which can contribute to the overall catalytic process. To overcome this limitation, glass wool can

be treated with chemicals like APTES (3-Aminopropyltriethoxysilane) to modify its surface properties and enhance its functionality as a catalyst support. This treatment is a form of surface functionalization that can significantly alter the characteristics of glass wool.[36] APTES introduces amine groups onto the glass surface, which can serve as anchoring points for catalysts. The amine groups can coordinate with metal ions, allowing for better dispersion and anchoring of metal catalysts.[36] Various metal and metal oxide nanoparticles synthesized on glass wool (GW) supports and used to catalyze different organic reactions in batch reactors, such as Palladium (Pd@GW) used for reductive dehalogenation of aryl halides and Sonogashira C-C coupling reactions, Copper (Cu@GW) used for N-C hetero-cycloaddition "click" reactions, Cobalt oxide (Co@GW) used for reductive dehalogenation of aryl halides, Gold (Au@GW) used for reduction of nitrobenzene to azobenzene and C-C coupling (sp^3-sp^3) dimerization reactions.[37]

Photocatalysts can facilitate the generation of singlet oxygen under light irradiation, enabling green and sustainable chemical processes. These reactions often proceed under mild conditions, reducing energy input and environmental impact. Studying helps optimize the design of photocatalysts, such as transition metal complexes, organic dyes, and semiconductor materials, to enhance their efficiency and selectivity. Therefore in the next section we are going to talk about the singlet oxygen

1.2.2 Singlet oxygen

Singlet oxygen ($^1O_2$) is a higher energy state of molecular oxygen, distinct from its triplet ground state ($^3O_2$). Discovered by Kautsky in 1931, singlet oxygen has since become a crucial species in photochemistry, biology, and medical applications. Defined by its unique electronic configuration where all electron spins are paired, singlet oxygen exists primarily in two states: $^1\Delta g$ (22.5 kcal.mol^{-1} above ground state) and $^1\Sigma g+$ (31.5 kcal.mol^{-1} above ground state).[38]

The properties of singlet oxygen are noticeably different from its ground state. With a lifetime ranging from nanoseconds in cells to about 45 minutes in the gas phase, singlet oxygen exhibits high reactivity, particularly with electron-rich organic compounds.[39] Its characteristic phosphorescence emission at 1270 nm, corresponding to the $^1\Delta g \rightarrow {}^3\Sigma g-$ transition, serves as a key identifier in both natural and experimental settings.[40]

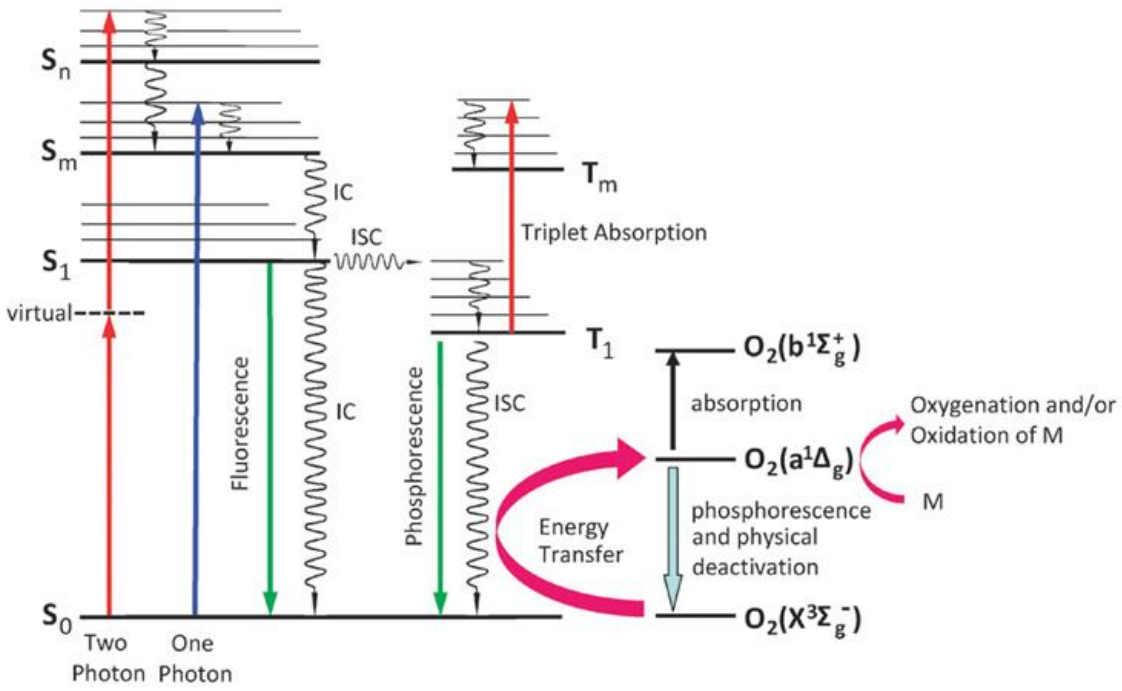

Figure 1.3. production of singlet oxygen via triplet-state photosensitization initiated by absorption of photons.[39] (reproduced with permission from Royal Society of Chemistry)

In photochemistry, singlet oxygen plays a pivotal role, often generated through photosensitization. This process involves the excitation of a photosensitizer molecule, which then transfers energy to ground state oxygen, producing singlet oxygen.[41] Common photosensitizers include porphyrins, phthalocyanines, rose bengal, and xanthon. The efficiency of singlet oxygen generation depends on factors such as the photosensitizer's quantum yield, oxygen concentration, and the surrounding medium.[40]

Singlet oxygen's high reactivity makes it a potent oxidizing agent in photochemical reactions. It participates in various transformations, including [4+2] cycloadditions (forming endoperoxides), [2+2] cycloadditions, and ene reactions. These reactions have found applications in organic synthesis, particularly in the production of complex natural products and pharmaceuticals.[42]

Beyond synthetic chemistry, singlet oxygen's role extends to environmental photochemistry. In natural waters, singlet oxygen formation through the interaction of dissolved

organic matter with sunlight contributes to the degradation of pollutants and the overall aquatic ecosystem dynamics.[43]

Singlet oxygen, with its unique properties and reactivity, continues to be a subject of intense research in photochemistry. To study the mechanism of singlet oxygen in photoreactions, it is essential to understand the relevant analytical techniques.

Laser flash photolysis coupled with Near-Infrared (NIR) detection has emerged as a powerful analytical technique for clarifying singlet oxygen-mediated oxidation mechanisms and determining associated rate constants. This method combines the high temporal resolution of laser excitation with the specificity of NIR detection, providing robust evidence for singlet oxygen involvement and detailed kinetic information.[38]

The technique typically employs a short, intense laser pulse to generate singlet oxygen via a photosensitizer. The subsequent detection of the characteristic 1270 nm emission of singlet oxygen using NIR-sensitive detectors offers direct proof of its formation and decay. This emission, resulting from the $^1\Delta g \rightarrow {}^3\Sigma g^-$ transition, serves as a unique "fingerprint" for singlet oxygen, allowing its identification in complex reaction systems.[40]

By monitoring the time-resolved intensity of this emission, researchers can quantify singlet oxygen lifetime and concentration changes. The addition of substrates often leads to a reduction in singlet oxygen lifetime, enabling the determination of quenching rate constants. Furthermore, by simultaneously tracking substrate consumption or product formation, complete kinetic studies of singlet oxygen-mediated oxidations can be achieved.[44]

By offering direct observation of singlet oxygen and enabling detailed kinetic analysis, this technique has become indispensable in fields ranging from fundamental photochemistry to biomedical applications.

1.3 Flow photochemistry

Flow photochemistry offers several advantages over traditional batch photochemistry methods, making it a better approach in many cases. Here are the key benefits:

1.3.1 Optimized photon utilization

One of the key advantages of flow photochemistry over traditional batch methods is the significant improvement in light penetration and utilization. The Beer-Lambert law is a fundamental principle that describes the attenuation of light as it travels through a material, and it is vital for reactor design considerations in photochemistry. The law is expressed as:

$$T = \frac{I}{I_0} = 10^{-A} = 10^{-\varepsilon cl} \quad , A = \varepsilon cl \qquad (1)$$

The transmission of photons (T) is correlated to the absorption of photons (A). The law states that absorbance (A) is directly proportional to the molar extinction coefficient (ε), the concentration of the absorbing species (c), and the path length (l).[45] According to this equation, as the light path length increases, light transmittance decreases exponentially.

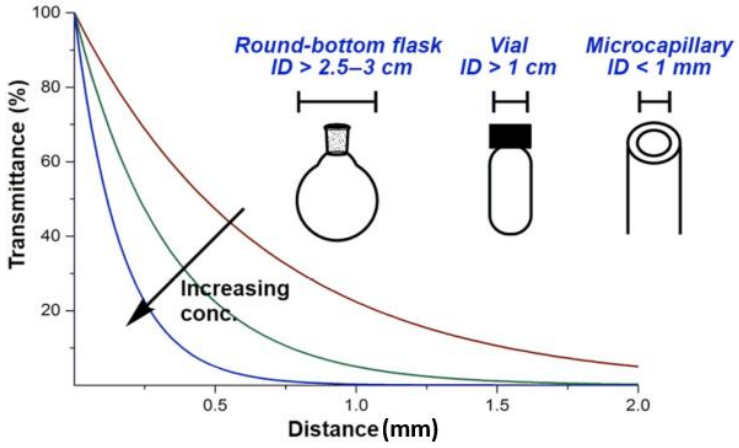

Figure 1.4. Attenuation of light irradiance with distance from light source. Transmission of light as a function of distance (mm) in a photocatalytic reaction using $Ru(bpy)_3Cl_2$ (c = 0.5 (blue), 1 (green), and 2 mM (red), ε =13000 $cm^{-1}M^{-1}$, λ ≈ 460 nm)[46]

Tris(2,2'-bipyridine) ruthenium (II) chloride ($Ru(bpy)_3Cl_2$), is widely used in photochemistry. It exhibits strong absorption in the visible region, this intensely orange-red color and high extinction coefficient are due to metal-to-ligand charge transfer (MLCT) transitions.[47] [$Ru(bpy)_3Cl_2$], with its high molar extinction coefficient, absorbs a significant amount of incident light within a short distance, Figure 1.3.[46,48] In fact, 50% of light is absorbed within just 0.5 mm.

This property highlights the importance of small dimensions of reactors and high surface-to-volume ratios in achieving nearly uniform illumination.

This is a crucial factor to consider when selecting the reaction vessel. In batch reactors, light penetration can be uneven, particularly in large volumes, as the intensity decreases exponentially due to absorption and scattering effects. This leads to inefficiencies, with only molecules near the light source receiving sufficient energy. In contrast, flow reactors are designed with narrow channels, ensuring all parts of the reaction mixture are uniformly exposed to light, thus maximizing light utilization.[49] The short and controlled path length in flow reactors allows light to reach reactant molecules more effectively, minimizing losses. This uniform exposure results in consistent reaction kinetics throughout the reactor, leading to higher efficiency, better yields, and fewer side reactions.

Decreasing path length is more beneficial in specific contexts where light penetration, mass transport, or diffusion is a limiting factor. Then in highly absorbing species, concentrated solutions, fast photochemical steps, and the reactions in which products are light sensitive and unstable, path length optimization becomes crucial.

1.3.2 Efficient mixing and temperature control

Enhanced mass and heat transfer is another significant benefit of flow systems in photochemistry. The continuous flow creates turbulent mixing, which improves mass transfer between reactants. Additionally, the high surface area-to-volume ratio in flow reactors allows for efficient heat transfer. This prevents local overheating and ensures uniform temperature throughout the reaction mixture. Better temperature control can lead to improved selectivity and yield, especially in temperature-sensitive reactions.[50,51]

1.3.3 Enhancing throughput in photochemical processes

Increased productivity is achieved through the continuous operation of flow systems, allowing for higher throughput compared to batch processes. Once optimized, these systems can run for extended periods without interruption. Steady-state conditions are easier to maintain, leading to consistent product quality over time. This continuous production model is particularly advantageous for large-scale manufacturing or when dealing with high-demand products. is

achieved through the continuous operation of flow systems, allowing for higher throughput compared to batch processes.[52]

1.3.4 Fine-tuning reaction conditions in continuous flow photoreactors

Better control over reaction parameters is a hallmark of flow chemistry. Flow rate can be precisely controlled to adjust residence time, while pressure and temperature control are more precise due to the smaller volumes being heated or cooled at any given time. Reactant concentrations can be fine-tuned by adjusting individual feed rates. This level of control allows for rapid optimization of reaction conditions, enabling researchers and process engineers to quickly find and maintain ideal reaction parameters.[53]

1.3.5 Improving reaction selectivity

Flow photochemistry often leads to improved selectivity compared to batch processes. The precise control over reaction parameters such as light intensity, exposure time, and temperature allows for fine-tuning of reaction conditions. This can favor desired pathways and minimize side reactions, leading to higher yields of the target product and reduced formation of unwanted by-products.[54,55] For example, in the photocatalytic oxidation of citronellol to rose oxide, a key fragrance compound, running the biphasic mixture in a narrow channel allowed for precise control of oxygen concentration and light exposure. This resulted in a selectivity increase to over 90% in flow, significantly improving the yield of the desired product.[56]

1.3.6 Reducing risks in large-scale photochemistry

Improved safety is a crucial aspect of flow photochemistry. Only small amounts of reactants are present in the reactor at any given time, reducing risks associated with large volumes of hazardous materials. The improved heat transfer reduces the risk of thermal runaway reactions, while closed systems minimize exposure to potentially toxic or volatile compounds.[57] These safety features make flow photochemistry an attractive option for handling dangerous or sensitive reactions.[58]

1.3.7 Scalability of photochemical reactions

Scalability is a significant advantage of flow systems. Once a reaction is optimized at a small scale, it can often be scaled up by simply increasing flow rates or running time.

Alternatively, increasing the reactor length or operating multiple reactors in parallel maintains optimal light conditions, even at larger scales. "Numbering up" - running multiple identical reactors in parallel - maintains the benefits of small-scale reactions while increasing output. This approach often requires less re-optimization compared to traditional batch scale-up, making the transition from lab to production more straightforward.[59,60]

1.3.8 Real-time monitoring and integrated purification

Compatibility with in-line analysis and purification is another benefit of flow systems. Spectroscopic techniques such as UV-Vis, IR, or Raman spectroscopy can be integrated for real-time monitoring of the reaction progress. Automated feedback loops can adjust conditions based on this in-line analysis, ensuring optimal performance. Moreover, purification steps like extraction, crystallization, or chromatography can be directly coupled to the reaction output, streamlining the overall process.[61–63]

1.3.9 Green chemistry aspects

Flow photochemistry can often be carried out under milder conditions (e.g., ambient temperature and pressure) and can make use of less toxic reagents and solvents. Reduced solvent usage is an environmental and economic advantage of flow photochemistry. More efficient reactions by increasing the concentration require less solvent per unit of product. Additionally, continuous processes allow for easier solvent recycling, reducing waste. This aligns with the principles of green chemistry by reducing energy consumption and minimizing waste. The result is improved environmental sustainability and reduced costs, making the process more economically viable and environmentally friendly.[64–66]

1.3.10 Efficient mixing of immiscible phases

Easier handling of multiphasic systems is facilitated by specialized flow reactors. These can efficiently mix immiscible liquids or gases and liquids, which is particularly useful for reactions involving gaseous reagents or products. The improved interfacial area can dramatically increase reaction rates in mass-transfer limited systems, opening possibilities for reactions that might be challenging in batch mode.[67,68]

1.3.11 Streamlining chemical synthesis

Finally, flow photochemistry offers the potential for process intensification. Multiple reactions or purification steps can be integrated into a single, continuous process. This can reduce overall processing time, equipment footprint, and intermediate handling steps. It enables novel reaction sequences that might be impractical in batch mode, potentially leading to more efficient synthetic routes or even new chemical transformations. This integration of multiple steps can significantly streamline production processes, leading to more efficient and cost-effective manufacturing.[69,70]

1.3.12 Enhancing efficiency with immobilized photocatalysts

Flow systems are particularly well-suited for reactions using immobilized catalysts. Photocatalysts can be immobilized on the reactor walls or solid supports packed into the reactor. This approach offers several benefits such as easy catalyst recovery and reuse, reduced product contamination by the catalyst, the potential for longer catalyst lifetimes due to controlled exposure conditions, and the possibility of using higher catalyst loadings without separation issues.[71,72]

The transition from batch to flow processes in photochemistry represents a significant advancement in chemical synthesis and processing. As the field continues to advance, flow photochemistry is well-positioned to play an increasingly important role in various sectors, including pharmaceuticals, fine chemicals, and materials science. The synergistic combination of these advantages not only improves existing processes but also enables the development of new reactions and products that may have been impractical or impossible in traditional batch systems.

In conclusion, the adoption of flow systems for photochemical reactions represents a paradigm shift in how we approach chemical synthesis and processing. It offers a powerful toolset for chemists and engineers to overcome longstanding challenges in photochemistry and unlock new possibilities in sustainable and efficient chemical production.

1.4 Outline of thesis

This research aims to develop innovative processes for chemical reactions by using photochemical methods and mechanisms. The work is structured across several chapters, each focusing on learning advanced photochemistry concepts and analytical techniques. These are then applied to enhance the scale-up process from laboratory to industrial production of various chemicals, addressing a critical need in contemporary industries. This comprehensive approach not only contributes to the advancement of chemical process development but also addresses the increasing demand for efficient, sustainable, and cost-effective production methods in the chemical industry. The research has significant implications for various sectors, including pharmaceuticals, materials science, and environmental technologies.

Chapter 2 explores nitro to amine reactions, a $10 billion annual business. The goal is to develop a flow system for this reaction using heterogeneous catalysis. We designed a catalyst based on palladium nanoparticles deposited on glass wool inside a glass tube as a photoreactor. While palladium is expensive, this optimized photosynthesized approach makes the process more cost-effective. The number of moles of catalyst added to the reactor for in-situ synthesis of the Pd@GW matched the number of palladium moles on the glass wool surface at the end of the synthesis confirmed with the ICP technique. This chapter examines the efficiency of the catalyst in various nitro compound reduction reactions, considering different reducing agents.

Chapter 3 addresses a significant gap in flow photochemistry by developing a reliable methodology for determining quantum efficiency in photoreactions. Despite the abundance of studies in the literature, yields of reaction products are rarely accompanied by quantum yield measurements, leaving the key reagent - light - unmeasured under experimental conditions. We designed an efficient flow reactor and proposed a flow actinometer based on the photochemistry of valerophenone, designed for easy implementation in organic laboratories for UV region irradiations. Our photoreactor design, which involves wrapping low-pressure lamps with Teflon tubing, serves as a model for this approach. The research aims to provide a standardized method for measuring light irradiance in flow systems.

Chapter 4 is built based on the gained knowledge from the previous chapter, focusing on optimizing the productivity of our designed flow system. We use the synthesis of silver nanoparticles as a case study, given their diverse applications across multiple fields including

medicine, photography, and water purification. Our primary objective was to develop a scalable and robust method for large-scale production of silver nanoparticles. This method is needed to maintain consistent quality, size distribution, and physicochemical characteristics over prolonged production cycles. We investigated various parameters such as the effect of different photoinitiators, and residence time to achieve this goal. We also explore the use of in-line monitoring techniques to ensure real-time quality control.

Chapter 5 uses photochemistry knowledge to investigate and optimize the selective semi-oxidation of tetrahydroisoquinoline (THIQ) to valuable dihydroisoquinoline (DHIQ) derivatives via singlet oxygen photooxidation. We seek to explore semiconductor photocatalysts like MoCo@GW, focusing on their efficacy under heterogeneous conditions to facilitate catalyst separation and reusability. A key aspect of our study was understanding the dual role of THIQ as both a reactant and an efficient singlet oxygen quencher, which drives reaction selectivity. Our research also investigates the formation of isoquinoline (IQ) and its function as an in situ-generated singlet oxygen catalyst. To provide empirical evidence for the proposed singlet oxygen mechanism, we employ laser flash photolysis with NIR detection, allowing us to determine rate constants for key oxidation steps and optimize the reaction conditions.

Chapter 6 outlines the summary and future directions of the research discussed in previous chapters, drawing key conclusions and emphasizing the significance of these studies at an industrial level. It highlights the impact of this work, including industrial projects that have already been initiated based on the dissertation's findings, such as the Vitamin D_2 project in collaboration with the Toronto Research Chemicals company.

1.5 References

(1) Romero, N. A.; Nicewicz, D. A. Organic Photoredox Catalysis. *Chem. Rev.* **2016**, *116* (17), 10075–10166. https://doi.org/10.1021/acs.chemrev.6b00057.

(2) Turro, N. J.; Ramamurthy, V.; Scaiano, J. C. *Principles of Molecular Photochemistry: An Introduction*; University Science Books, 2009.

(3) Ciamician, G. The Photochemistry of the Future. *Science* **1912**, *36* (926), 385–394. https://doi.org/10.1126/science.36.926.385.

(4) Jablonski, A. Efficiency of Anti-Stokes Fluorescence in Dyes. *Nature* **1933**, *131* (3319), 839–840. https://doi.org/10.1038/131839b0.

(5) Zewail, A. H. Femtochemistry: Atomic-Scale Dynamics of the Chemical Bond. *J. Phys. Chem. A* **2000**, *104* (24), 5660–5694. https://doi.org/10.1021/jp001460h.

(6) Klessinger, M. Excited States and Photochemistry of Organic Molecules. *No Title*.

(7) Valeur, B.; Berberan-Santos, M. N. *Molecular Fluorescence: Principles and Applications*; John Wiley & Sons, 2013.

(8) El-Sayed, M. A. Spin—Orbit Coupling and the Radiationless Processes in Nitrogen Heterocyclics. *J. Chem. Phys.* **1963**, *38* (12), 2834–2838. https://doi.org/10.1063/1.1733610.

(9) Baldo, M. A.; O'Brien, D. F.; You, Y.; Shoustikov, A.; Sibley, S.; Thompson, M. E.; Forrest, S. R. Highly Efficient Phosphorescent Emission from Organic Electroluminescent Devices. In *Electrophosphorescent Materials and Devices*; Jenny Stanford Publishing, 2023.

(10) Balzani, V.; Ceroni, P.; Juris, A. *Photochemistry and Photophysics: Concepts, Research, Applications*; John Wiley & Sons, 2014.

(11) Scaiano, J. C. (Tito). *Photochemistry Essentials*; American Chemical Society, 2022.

(12) Albini, A. The Framework of Photochemistry: The Laws. In *Photochemistry: Past, Present and Future*; Albini, A., Ed.; Springer: Berlin, Heidelberg, 2016; pp 9–40. https://doi.org/10.1007/978-3-662-47977-3_2.

(13) Hoffmann, M. R.; Martin, S. T.; Choi, W.; Bahnemann, D. W. Environmental Applications of Semiconductor Photocatalysis. *Chem. Rev.* **1995**, *95* (1), 69–96. https://doi.org/10.1021/cr00033a004.

(14) Ardo, S.; Meyer, G. J. Photodriven Heterogeneous Charge Transfer with Transition-Metal Compounds Anchored to TiO2 Semiconductor Surfaces. *Chem. Soc. Rev.* **2008**, *38* (1), 115–164. https://doi.org/10.1039/B804321N.

(15) Serpone, N.; Salinaro, A. Terminology, Relative Photonic Efficiencies and Quantum Yields in Heterogeneous Photocatalysis. Part I: Suggested Protocol. *Pure Appl. Chem.* **1999**, *71* (2), 303–320. https://doi.org/10.1351/pac199971020303.

(16) Wang, H.; Zhang, L.; Chen, Z.; Hu, J.; Li, S.; Wang, Z.; Liu, J.; Wang, X. Semiconductor Heterojunction Photocatalysts: Design, Construction, and Photocatalytic Performances. *Chem. Soc. Rev.* **2014**, *43* (15), 5234–5244. https://doi.org/10.1039/C4CS00126E.

(1) Romero, N. A.; Nicewicz, D. A. Organic Photoredox Catalysis. *Chem. Rev.* **2016**, *116* (17), 10075–10166. https://doi.org/10.1021/acs.chemrev.6b00057.

(2) Turro, N. J.; Ramamurthy, V.; Scaiano, J. C. *Principles of Molecular Photochemistry: An Introduction*; University Science Books, 2009.

(3) Ciamician, G. The Photochemistry of the Future. *Science* **1912**, *36* (926), 385–394. https://doi.org/10.1126/science.36.926.385.

(4) Jablonski, A. Efficiency of Anti-Stokes Fluorescence in Dyes. *Nature* **1933**, *131* (3319), 839–840. https://doi.org/10.1038/131839b0.

(5) Zewail, A. H. Femtochemistry: Atomic-Scale Dynamics of the Chemical Bond. *J. Phys. Chem. A* **2000**, *104* (24), 5660–5694. https://doi.org/10.1021/jp001460h.

(6) Klessinger, M. Excited States and Photochemistry of Organic Molecules. *No Title*.

(7) Valeur, B.; Berberan-Santos, M. N. *Molecular Fluorescence: Principles and Applications*; John Wiley & Sons, 2013.

(8) El-Sayed, M. A. Spin—Orbit Coupling and the Radiationless Processes in Nitrogen Heterocyclics. *J. Chem. Phys.* **1963**, *38* (12), 2834–2838. https://doi.org/10.1063/1.1733610.

(9) Baldo, M. A.; O'Brien, D. F.; You, Y.; Shoustikov, A.; Sibley, S.; Thompson, M. E.; Forrest, S. R. Highly Efficient Phosphorescent Emission from Organic Electroluminescent Devices. In *Electrophosphorescent Materials and Devices*; Jenny Stanford Publishing, 2023.

(10) Balzani, V.; Ceroni, P.; Juris, A. *Photochemistry and Photophysics: Concepts, Research, Applications*; John Wiley & Sons, 2014.

(11) Scaiano, J. C. (Tito). *Photochemistry Essentials*; American Chemical Society, 2022.

(12) Albini, A. The Framework of Photochemistry: The Laws. In *Photochemistry: Past, Present and Future*; Albini, A., Ed.; Springer: Berlin, Heidelberg, 2016; pp 9–40. https://doi.org/10.1007/978-3-662-47977-3_2.

(13) Hoffmann, M. R.; Martin, S. T.; Choi, W.; Bahnemann, D. W. Environmental Applications of Semiconductor Photocatalysis. *Chem. Rev.* **1995**, *95* (1), 69–96. https://doi.org/10.1021/cr00033a004.

(14) Ardo, S.; Meyer, G. J. Photodriven Heterogeneous Charge Transfer with Transition-Metal Compounds Anchored to TiO2 Semiconductor Surfaces. *Chem. Soc. Rev.* **2008**, *38* (1), 115–164. https://doi.org/10.1039/B804321N.

(15) Serpone, N.; Salinaro, A. Terminology, Relative Photonic Efficiencies and Quantum Yields in Heterogeneous Photocatalysis. Part I: Suggested Protocol. *Pure Appl. Chem.* **1999**, *71* (2), 303–320. https://doi.org/10.1351/pac199971020303.

(16) Wang, H.; Zhang, L.; Chen, Z.; Hu, J.; Li, S.; Wang, Z.; Liu, J.; Wang, X. Semiconductor Heterojunction Photocatalysts: Design, Construction, and Photocatalytic Performances. *Chem. Soc. Rev.* **2014**, *43* (15), 5234–5244. https://doi.org/10.1039/C4CS00126E.

(17) Fujishima, A.; Zhang, X.; Tryk, D. A. TiO2 Photocatalysis and Related Surface Phenomena. *Surf. Sci. Rep.* **2008**, *63* (12), 515–582. https://doi.org/10.1016/j.surfrep.2008.10.001.

(18) Kisch, H. Semiconductor Photocatalysis—Mechanistic and Synthetic Aspects. *Angew. Chem. Int. Ed.* **2013**, *52* (3), 812–847. https://doi.org/10.1002/anie.201201200.

(19) Zhang, X.; Chen, Y. L.; Liu, R.-S.; Tsai, D. P. Plasmonic Photocatalysis. *Rep. Prog. Phys.* **2013**, *76* (4), 046401. https://doi.org/10.1088/0034-4885/76/4/046401.

(20) Roger, I.; Shipman, M. A.; Symes, M. D. Earth-Abundant Catalysts for Electrochemical and Photoelectrochemical Water Splitting. *Nat. Rev. Chem.* **2017**, *1* (1), 1–13. https://doi.org/10.1038/s41570-016-0003.

(21) Wang, Y.; Wang, X.; Antonietti, M. Polymeric Graphitic Carbon Nitride as a Heterogeneous Organocatalyst: From Photochemistry to Multipurpose Catalysis to Sustainable Chemistry. *Angew. Chem. Int. Ed.* **2012**, *51* (1), 68–89. https://doi.org/10.1002/anie.201101182.

(22) Zhang, T.; Lin, W. Metal–Organic Frameworks for Artificial Photosynthesis and Photocatalysis. *Chem. Soc. Rev.* **2014**, *43* (16), 5982–5993. https://doi.org/10.1039/C4CS00103F.

(23) Xiang, Q.; Yu, J.; Jaroniec, M. Graphene -Based Semiconductor Photocatalysts. *Chem. Soc. Rev.* **2012**, *41* (2), 782–796. https://doi.org/10.1039/C1CS15172J.

(24) Low, J.; Yu, J.; Jaroniec, M.; Wageh, S.; Al-Ghamdi, A. A. Heterojunction Photocatalysts. *Adv. Mater.* **2017**, *29* (20), 1601694. https://doi.org/10.1002/adma.201601694.

(25) Zhao, J.; Holmes, M. A.; Osterloh, F. E. Quantum Confinement Controls Photocatalysis: A Free Energy Analysis for Photocatalytic Proton Reduction at CdSe Nanocrystals. *ACS Nano* **2013**, *7* (5), 4316–4325. https://doi.org/10.1021/nn400826h.

(26) Lee, S. H.; Choi, D. S.; Kuk, S. K.; Park, C. B. Photobiocatalysis: Activating Redox Enzymes by Direct or Indirect Transfer of Photoinduced Electrons. *Angew. Chem. Int. Ed.* **2018**, *57* (27), 7958–7985. https://doi.org/10.1002/anie.201710070.

(27) Pelizzette, E.; Serpone, N. *Homogeneous and Heterogeneous Photocatalysis*; Springer Science & Business Media, 2012.

(28) Ibhadon, A. O.; Fitzpatrick, P. Heterogeneous Photocatalysis: Recent Advances and Applications. *Catalysts* **2013**, *3* (1), 189–218. https://doi.org/10.3390/catal3010189.

(29) Matatov-Meytal, Y.; Sheintuch, M. Catalytic Fibers and Cloths. *Appl. Catal. Gen.* **2002**, *231* (1), 1–16. https://doi.org/10.1016/S0926-860X(01)00963-2.

(30) Corma, A.; Serna, P. Chemoselective Hydrogenation of Nitro Compounds with Supported Gold Catalysts. *Science* **2006**, *313* (5785), 332–334. https://doi.org/10.1126/science.1128383.

(31) Kantam, M. L.; Chakravarti, R.; Pal, U.; Sreedhar, B.; Bhargava, S. Nanocrystalline Magnesium Oxide-Stabilized Palladium(0): An Efficient and Reusable Catalyst for Selective Reduction of Nitro Compounds. *Adv. Synth. Catal.* **2008**, *350* (6), 822–827. https://doi.org/10.1002/adsc.200800018.

(32) Takasaki, M.; Motoyama, Y.; Higashi, K.; Yoon, S.-H.; Mochida, I.; Nagashima, H. Chemoselective Hydrogenation of Nitroarenes with Carbon Nanofiber-Supported Platinum and Palladium Nanoparticles. *Org. Lett.* **2008**, *10* (8), 1601–1604. https://doi.org/10.1021/ol800277a.

(33) Wu, H.; Zhuo, L.; He, Q.; Liao, X.; Shi, B. Heterogeneous Hydrogenation of Nitrobenzenes over Recyclable Pd(0) Nanoparticle Catalysts Stabilized by Polyphenol-Grafted Collagen Fibers. *Appl. Catal. Gen.* **2009**, *366* (1), 44–56. https://doi.org/10.1016/j.apcata.2009.06.024.

(34) Jagadeesh, R. V.; Surkus, A.-E.; Junge, H.; Pohl, M.-M.; Radnik, J.; Rabeah, J.; Huan, H.; Schünemann, V.; Brückner, A.; Beller, M. Nanoscale Fe2O3-Based Catalysts for Selective Hydrogenation of Nitroarenes to Anilines. *Science* **2013**, *342* (6162), 1073–1076. https://doi.org/10.1126/science.1242005.

(35) Barelko, V. V.; Kuznetsov, M. V.; Dorokhov, V. G.; Parkin, I. Glass-Fiber Woven Catalysts as Alternative Catalytic Materials for Various Industries. A Review. *Russ. J. Phys. Chem. B* **2017**, *11* (4), 606–617. https://doi.org/10.1134/S1990793117040030.

(36) Zucca, P.; Sanjust, E. Inorganic Materials as Supports for Covalent Enzyme Immobilization: Methods and Mechanisms. *Molecules* **2014**, *19* (9), 14139–14194. https://doi.org/10.3390/molecules190914139.

(37) Elhage, A.; Wang, B.; Marina, N.; Luisa Marin, M.; Cruz, M.; E. Lanterna, A.; C. Scaiano, J. Glass Wool: A Novel Support for Heterogeneous Catalysis. *Chem. Sci.* **2018**, *9* (33), 6844–6852. https://doi.org/10.1039/C8SC02115E.

(38) Schweitzer, C.; Schmidt, R. Physical Mechanisms of Generation and Deactivation of Singlet Oxygen. *Chem. Rev.* **2003**, *103* (5), 1685–1758. https://doi.org/10.1021/cr010371d.

(39) Ogilby, P. R. Singlet Oxygen: There Is Indeed Something New under the Sun. *Chem. Soc. Rev.* **2010**, *39* (8), 3181–3209. https://doi.org/10.1039/B926014P.

(40) DeRosa, M. C.; Crutchley, R. J. Photosensitized Singlet Oxygen and Its Applications. *Coord. Chem. Rev.* **2002**, *233–234*, 351–371. https://doi.org/10.1016/S0010-8545(02)00034-6.

(41) Ghogare, A. A.; Greer, A. Using Singlet Oxygen to Synthesize Natural Products and Drugs. *Chem. Rev.* **2016**, *116* (17), 9994–10034. https://doi.org/10.1021/acs.chemrev.5b00726.

(42) Stratakis, M.; Orfanopoulos, M. Regioselectivity in the Ene Reaction of Singlet Oxygen with Alkenes. *Tetrahedron* **2000**, *56* (12), 1595–1615. https://doi.org/10.1016/S0040-4020(99)00950-3.

(43) Latch, D. E.; McNeill, K. Microheterogeneity of Singlet Oxygen Distributions in Irradiated Humic Acid Solutions. *Science* **2006**, *311* (5768), 1743–1747. https://doi.org/10.1126/science.1121636.

(44) Wilkinson, F.; Helman, W. P.; Ross, A. B. Rate Constants for the Decay and Reactions of the Lowest Electronically Excited Singlet State of Molecular Oxygen in Solution. An Expanded and Revised Compilation. *J. Phys. Chem. Ref. Data* **1995**, *24* (2), 663–677. https://doi.org/10.1063/1.555965.

(45) Steiner, U. E. Fundamentals of Photophysics, Photochemistry, and Photobiology. In *Photodynamic Therapy: From Theory to Application*; Abdel-Kader, M. H., Ed.; Springer: Berlin, Heidelberg, 2014; pp 25–58. https://doi.org/10.1007/978-3-642-39629-8_2.

(46) Sambiagio, C.; Noël, T. Flow Photochemistry: Shine Some Light on Those Tubes! *Trends Chem.* **2020**, *2* (2), 92–106. https://doi.org/10.1016/j.trechm.2019.09.003.

(47) Kalyanasundaram, K. Photophysics, Photochemistry and Solar Energy Conversion with Tris(Bipyridyl)Ruthenium(II) and Its Analogues. *Coord. Chem. Rev.* **1982**, *46*, 159–244. https://doi.org/10.1016/0010-8545(82)85003-0.

(48) Su, Y.; Straathof, N. J. W.; Hessel, V.; Noël, T. Photochemical Transformations Accelerated in Continuous-Flow Reactors: Basic Concepts and Applications. *Chem. – Eur. J.* **2014**, *20* (34), 10562–10589. https://doi.org/10.1002/chem.201400283.

(49) Cambié, D.; Bottecchia, C.; Straathof, N. J. W.; Hessel, V.; Noël, T. Applications of Continuous-Flow Photochemistry in Organic Synthesis, Material Science, and Water Treatment. *Chem. Rev.* **2016**, *116* (17), 10276–10341. https://doi.org/10.1021/acs.chemrev.5b00707.

(50) Plutschack, M. B.; Pieber, B.; Gilmore, K.; Seeberger, P. H. The Hitchhiker's Guide to Flow Chemistry. *Chem. Rev.* **2017**, *117* (18), 11796–11893. https://doi.org/10.1021/acs.chemrev.7b00183.

(51) Boffito, D. C.; Fernandez Rivas, D. Process Intensification Connects Scales and Disciplines towards Sustainability. *Can. J. Chem. Eng.* **2020**, *98* (12), 2489–2506. https://doi.org/10.1002/cjce.23871.

(52) Loubière, K.; Oelgemöller, M.; Aillet, T.; Dechy-Cabaret, O.; Prat, L. Continuous-Flow Photochemistry: A Need for Chemical Engineering. *Chem. Eng. Process. Process Intensif.* **2016**, *104*, 120–132. https://doi.org/10.1016/j.cep.2016.02.008.

(53) Knowles, J. P.; Elliott, L. D.; Booker-Milburn, K. I. Flow Photochemistry: Old Light through New Windows. *Beilstein J. Org. Chem.* **2012**, *8* (1), 2025–2052. https://doi.org/10.3762/bjoc.8.229.

(54) Politano, F.; Oksdath-Mansilla, G. Light on the Horizon: Current Research and Future Perspectives in Flow Photochemistry. *Org. Process Res. Dev.* **2018**, *22* (9), 1045–1062. https://doi.org/10.1021/acs.oprd.8b00213.

(55) Rehm, T. H. Flow Photochemistry as a Tool in Organic Synthesis. *Chem. – Eur. J.* **2020**, *26* (71), 16952–16974. https://doi.org/10.1002/chem.202000381.

(56) Lévesque, F.; Seeberger, P. H. Highly Efficient Continuous Flow Reactions Using Singlet Oxygen as a "Green" Reagent. *Org. Lett.* **2011**, *13* (19), 5008–5011. https://doi.org/10.1021/ol2017643.

(57) Liebner, C.; Fischer, J.; Heinrich, S.; Lange, T.; Hieronymus, H.; Klemm, E. Are Micro Reactors Inherently Safe? An Investigation of Gas Phase Explosion Propagation Limits on Ethene Mixtures. *Process Saf. Environ. Prot.* **2012**, *90* (2), 77–82. https://doi.org/10.1016/j.psep.2011.08.006.

(58) Britton, J.; L. Raston, C. Multi-Step Continuous-Flow Synthesis. *Chem. Soc. Rev.* **2017**, *46* (5), 1250–1271. https://doi.org/10.1039/C6CS00830E.

(59) Amador, C.; Gavriilidis, A.; Angeli, P. Flow Distribution in Different Microreactor Scale-out Geometries and the Effect of Manufacturing Tolerances and Channel Blockage. *Chem. Eng. J.* **2004**, *101* (1), 379–390. https://doi.org/10.1016/j.cej.2003.11.031.

(60) Noël, T. A Personal Perspective on the Future of Flow Photochemistry. *J. Flow Chem.* **2017**, *7* (3), 87–93. https://doi.org/10.1556/1846.2017.00022.

(61) Yue, J.; Schouten, J. C.; Nijhuis, T. A. Integration of Microreactors with Spectroscopic Detection for Online Reaction Monitoring and Catalyst Characterization. *Ind. Eng. Chem. Res.* **2012**, *51* (45), 14583–14609. https://doi.org/10.1021/ie301258j.

(62) Jurina, T.; Cvetnić, T. S.; Šalić, A.; Benković, M.; Valinger, D.; Kljusurić, J. G.; Zelić, B.; Jurinjak Tušek, A. Application of Spectroscopy Techniques for Monitoring (Bio)Catalytic Processes in Continuously Operated Microreactor Systems. *Catalysts* **2023**, *13* (4), 690. https://doi.org/10.3390/catal13040690.

(63) McMullen, J. P.; Jensen, K. F. Integrated Microreactors for Reaction Automation: New Approaches to Reaction Development. *Annu. Rev. Anal. Chem.* **2010**, *3* (Volume 3, 2010), 19–42. https://doi.org/10.1146/annurev.anchem.111808.073718.

(64) Williams, J. D.; Kappe, C. O. Recent Advances toward Sustainable Flow Photochemistry. *Curr. Opin. Green Sustain. Chem.* **2020**, *25*, 100351. https://doi.org/10.1016/j.cogsc.2020.05.001.

(65) Fuse, S.; Tanabe, N.; Yoshida, M.; Yoshida, H.; Doi, T.; Takahashi, T. Continuous-Flow Synthesis of Vitamin D3. *Chem. Commun.* **2009**, *46* (46), 8722–8724. https://doi.org/10.1039/C0CC02239J.

(66) Oelgemöller, M. Solar Photochemical Synthesis: From the Beginnings of Organic Photochemistry to the Solar Manufacturing of Commodity Chemicals. *Chem. Rev.* **2016**, *116* (17), 9664–9682. https://doi.org/10.1021/acs.chemrev.5b00720.

(67) Nieves-Remacha, M. J.; Kulkarni, A. A.; Jensen, K. F. Hydrodynamics of Liquid–Liquid Dispersion in an Advanced-Flow Reactor. *Ind. Eng. Chem. Res.* **2012**, *51* (50), 16251–16262. https://doi.org/10.1021/ie301821k.

(68) Nieves-Remacha, M. J.; Kulkarni, A. A.; Jensen, K. F. Gas–Liquid Flow and Mass Transfer in an Advanced-Flow Reactor. *Ind. Eng. Chem. Res.* **2013**, *52* (26), 8996–9010. https://doi.org/10.1021/ie4011707.

(69) Tomarelli, E.; Cerra, B.; Mutti, F. G.; Gioiello, A. Merging Continuous Flow Technology, Photochemistry and Biocatalysis to Streamline Steroid Synthesis. *Adv. Synth. Catal.* **2023**, *365* (23), 4024–4048. https://doi.org/10.1002/adsc.202300305.

(70) Porta, R.; Benaglia, M.; Puglisi, A. Flow Chemistry: Recent Developments in the Synthesis of Pharmaceutical Products. *Org. Process Res. Dev.* **2016**, *20* (1), 2–25. https://doi.org/10.1021/acs.oprd.5b00325.

(71) Constantino, D. S. M.; Dias, M. M.; Silva, A. M. T.; Faria, J. L.; Silva, C. G. Intensification Strategies for Improving the Performance of Photocatalytic Processes: A Review. *J. Clean. Prod.* **2022**, *340*, 130800. https://doi.org/10.1016/j.jclepro.2022.130800.

(72) Van Gerven, T.; Mul, G.; Moulijn, J.; Stankiewicz, A. A Review of Intensification of Photocatalytic Processes. *Chem. Eng. Process. Process Intensif.* **2007**, *46* (9), 781–789. https://doi.org/10.1016/j.cep.2007.05.012.

Chapter 2. Nitro to amine reductions using aqueous flow catalysis under ambient conditions.

2.1 Preamble to Chapter 2

In the world of chemistry, finding ways to speed up reactions without causing extra waste is a key to success in industry. Heterogeneous catalysts, which are solid and easily separated from reactions, stand out for their recyclability, especially when materials like metal nanoparticles are attached to a support and used as a fixed bed catalyst in a continuous flow setup.

This article is my first peer-reviewed publication in Prof. Scaiano's group and started with the goal of designing a heterogeneous catalyst for a sustainable flow system. The results and outcome of this project made me more enthusiastic to work in this field and learn more about optimizing reaction conditions.

In this research, glass wool, an affordable and adaptable material with a high surface area, is used as a catalyst support. The catalyst is prepared in situ with minimal palladium loading on inexpensive glass wool (Pd@GW) and the lowest waste of Pd during catalyst synthesis. Comparing the number of moles of palladium used in catalyst preparation and experimental ICP results, after preparing the catalyst showed the effectiveness of the method used to make the catalyst.

The Pd@GW in a flow setup offers a sustainable and scalable method for nitro to amine reductions under ambient conditions. This process is highlighted for its efficiency, using water as the solvent, and operating at room temperature and atmospheric pressure which is significant for industrial applications, particularly in converting nitrobenzene to aniline which is a key chemical in the production of polyurethanes. This is important because it can lead to less waste and lower costs in making important chemicals, focusing on keeping our environment safe while still being able to do complex chemistry.

2.2 Post-print Version of the Manuscript

First published in iScience, 2021, 24, 103472

2.2.1 Abstract

A catalyst based on Pd on glass wool (Pd@GW) shows exceptional performance and durability for the reduction of nitrobenzene to aniline at room temperature and ambient pressure in aqueous solutions. The reaction is performed in a flow system and completed with 100% conversion under a variety of flow rates, 2 to 100 mL min^{-1} (normal laboratory fast flow conditions). Sodium borohydride or dihydrogen performs well as a reducing agent. Scale-up of the reaction to flows of 100 mL min^{-1} also shows high conversions and robust catalytic performance. Catalyst deactivation can be readily corrected by flowing a $NaBH_4$ solution. The catalytic system proves to be generally efficient, performing well with a range of nitroaromatic compounds. The shelf life of the catalyst is excellent and its reusability after 6-8 months of storage showed the same performance as for the fresh catalyst.

2.2.2 Introduction

The reduction of nitro compounds to the corresponding amines is important in the fine chemicals and pharmaceutical industries.[1–3] Among the many nitro compound reductions, no other compares with the conversion of nitrobenzene to aniline, responsible for over 95% of the use of nitrobenzene; in 2019 a total of 1.63 million metric tons of nitrobenzene were produced in the USA and its annual worldwide sales are rapidly approaching $10B.(2020) In turn, 80% of the aniline is used to produce methylene diphenyl diisocyanate (MDI), a key material in the production of polyurethanes.[4]

The reduction of nitrobenzene to aniline was first observed in 1843, eventually leading to the Beauchamp process (1854) using iron and hydrochloric acid,[5,6] but ultimately replaced by efficient catalytic processes employed by many of the key current producers.[7] In one research nano-Fe_3O_4@Al_2O_3 catalyst was used in the flow system at 150℃ and 30 bar back pressure.[8] There are numerous patents and reports on the subject,[9,10] one in particular, uses 5 wt% palladium on carbon and operates at temperatures and pressures as high as 225 °C and 5,000 kPa

respectively.[11] Three decades later, patents still include palladium as a catalyst and work at temperatures of 200 °C and pressures of 600 kPa.[12]

Moving forward, more sustainable processes should be developed for the reduction of nitro compounds, including some of the following advances: (i) reaction conditions close to ambient temperatures and pressures, reducing production cost and improving safety (ii) use of green solvents, such as water; and (iii) operate under flow conditions with easy-to-prepare catalysts. A recent review deals specifically with point (ii) including some examples of flow systems.[13] Other flow-compatible reactions, such as Suzuki-Miyaura coupling on Pd catalysts, have been also reported, however, high loadings of Pd (up to 7 wt%) are necessary.[14,15]

In this contribution we report on the catalytic reduction of nitro compounds (illustrated for nitrobenzene in Scheme 2.1) working at ambient temperature and pressures in an aqueous solution, using a reusable catalyst based on palladium supported on glass wool (Pd@GW), and operating under flow conditions. This follows the successful development of inexpensive glass wool as a catalyst support.[16,17] Although non-precious metals could be used in the reduction of nitro compounds, our previous results suggest that, in contrast with Pd, non-noble metals such as Cu or Co have a weak attachment to the treated glass wool support and some metal leaching cannot be easily avoided. Thus, this work achieves all the goals indicated above by utilizing a recyclable catalytic system, thereby reducing the amount of noble metal used. Additionally, the use of $NaBH_4$ as an easy-to-handle, non-explosive and non-flammable reducing agent facilitates the screening of catalytic conditions, while H_2 at atmospheric pressure is highly efficient avoiding the common need for high pressures and specialized reactors. Finally, we also report a successful attempt to scale up the process, from an initial milligram scale to multigram product formation and the handling of multi-litre volumes.

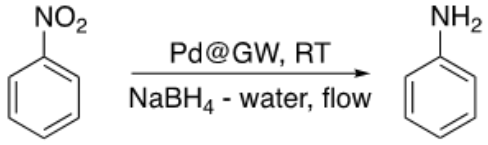

Scheme 2.1. Reduction of nitrobenzene using Pd@GW in a flow system

2.2.3 Experimental Procedure

A few preliminary batch experiments were performed in glass containers (25 mL) under gentle stirring, as strong stirring can damage the glass wool fibres. Most of the work was performed in glass tubes (borosilicate) of various diameters and lengths. The catalysts were prepared in situ in the same tubes where they would be used for catalytic nitro reduction. The solvent is water or aqueous ethanol for all the experiments described here and the maximum concentration used was 0.1M. A small amount of ethanol was used to facilitate solubilization at higher concentrations. Although surfactants have been reported to facilitate nitro compound dissolution in water,[18,19] the use of ethanol and acetonitrile minimizes product contamination.

2.2.3.1 Catalyst synthesis

The synthesis of the Pd@GW catalyst was inspired by batch experiments performed in our earlier publication and performed with some modifications.[16] In this updated method, waste generation was reduced by preparing the catalyst directly inside the reactor tube. The catalyst is prepared by photo-deposition of metallic Pd onto glass wool using a glass tube. The geometry of this tube, in line with the shape of the light source, increases the surface exposure to irradiation and the efficiency of the photodeposition process. Briefly, APTES ((3-Aminopropyl) triethoxysilane) treated glass wool (Figure S2.4) was placed inside an Ace glass 30 cm chromatographic tube with 27 cm active length and a solution of $Pd(acac)_2$ and photoinitiator (I-2959) in ethanol was added to the glass wool inside the tube and irradiated with UVA light to photo-deposit Pd on the glass wool. The washed and dried catalyst was taken out from the tube to use in batch experiments.

For flow experiments, the Pd@GW catalyst was fabricated directly in the flow catalysis tube. Two different flow systems were used: System 1 made of a borosilicate glass tube (length: 30 cm, ID 10 mm) connected through Teflon tubing (ID: 2 mm); and System 2 made of a borosilicate tube (length: 150 cm, ID: 13 mm) connected through Teflon tubing (ID: 5 mm). System 1 was used for a small-scale flow synthesis, has a useful volume of 21-24 mL and can be conveniently fitted on a hot-dog cooker adapted for the in situ photochemical synthesis of Pd@GW while the tube rotates to ensure an even exposure of the nascent catalyst. The samples

were irradiated with an Expo panel from Luzchem fitted with five UVA lamps. A photograph of the catalyst synthesis assembly has been included in the SI (Figure S2.4). A peristaltic pump (Masterflex Digi-Staltic Model # 7525-34) suitable for flow rates of up to ~30 $mLmin^{-1}$ was employed for this work; the solution of reactants was pumped over the catalyst for a single pass and samples were collected periodically at the exit from the column, and their UV-Vis spectra recorded. Some samples were analysed with GC-MS in addition to the UV-Vis spectrum.

A similar strategy was used to scale up the flow reaction. In this case, System 2 was used; once filled with catalyst (Pd@GW, 10 g), the actual free volume of the system without considering H_2 gas volume was ~150 mL. The catalyst synthesis was also performed in situ, but a different UVA exposure setup was required. Here the flow tube was surrounded by 4 UVA lamps, each 40 watts and 120 cm long; the flow tube was rotated regularly to ensure that the entire length was exposed to UVA light. Further details are available in the SI.

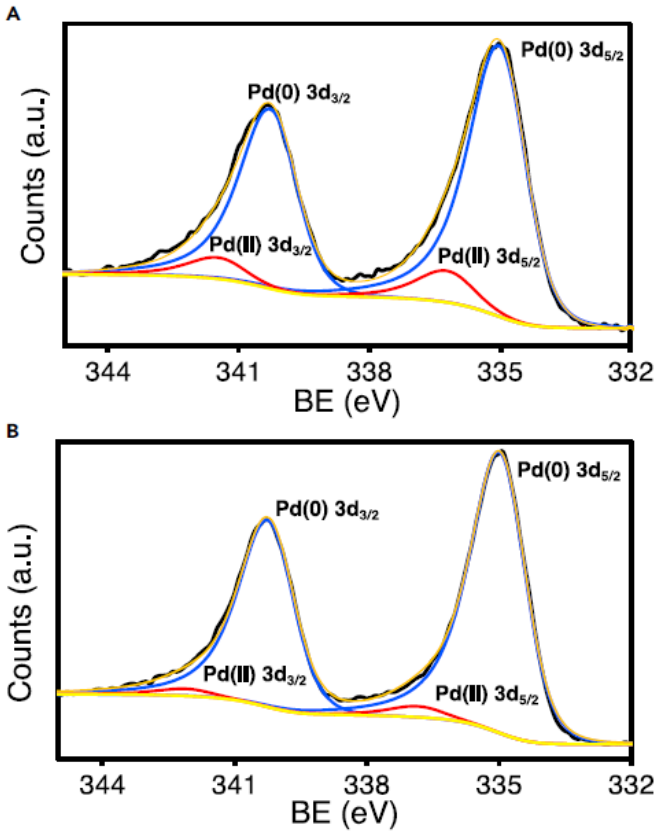

Figure 2.1. Deconvoluted Pd 3d HR-XPS spectrum of the Pd@GW catalyst (A) before treating with $NaBH_4$ (B) after treating with $NaBH_4$.

2.2.3.2 Catalyst characterization

The catalyst was characterized by X-ray Photoelectron spectroscopy (XPS), Scanning Electron Microscopy (SEM), and Inductively Coupled Plasma Optical Emission Spectroscopy (ICP-OES). Two samples of Pd@GW were analysed by XPS to determine the oxidation state of palladium. After observing some decrease in performance in the long tube under conditions of fast flow (vide infra) XPS analyses were performed to monitor possible changes in the Pd oxidation state, in particular because of $NaBH_4$ treatment. A catalyst sample was collected at the entry point of the tube before treating it with $NaBH_4$, while another catalyst sample was taken from the exit point of the long tube after treating it with $NaBH_4$. Figure 2.1 shows the deconvoluted Pd 3d HR-XPS spectrum. Characteristic peaks for Pd 3d were fitted using the spin-orbit split constituted by Pd (0) $3d_{5/2}$ (334.9 eV), Pd (0) $3d_{3/2}$ (340.2 eV), Pd (II) $3d_{5/2}$ (336.2 eV), and Pd (II) $3d_{3/2}$ (341.4 eV) separated by 5.26 eV.

Two catalysts were prepared with metal loadings of 3.5 wt% and 0.35 wt% (nominal amount) of Pd in EtOH solution. Three different catalyst samples (1) fresh 3.5 wt%, (2) fresh 0.35 wt%, and (3) used 0.35 wt% were selected to analyze the amount of Pd loaded onto the glass wool by ICP-OES, using an Agilent Vista Pro ICP Emission Spectrometer. Samples used were from the scale-up System 2 and sample (3) was collected after conversion of 47 mmol of NB into aniline. Sample replicates of 20 mg of Pd@GW were accurately weighed, digested with aqua regia, and then diluted. The samples were measured and quantified by using the Pd emission line at 340.45 nm. The average results of ICP-OES for these samples were (1) 0.96 ± 0.07, (2) 0.32 ± 0.02, and (3) 0.29 ± 0.01 wt% Pd on glass wool, respectively; this is, for high Pd loadings (sample 1), only one-third of Pd used in the synthesis can be effectively loaded onto GW; whereas low loadings (sample 2) can be prepared with over 90% yield. Interestingly, the amount of Pd in sample (3) compared to sample (2) is similar, suggesting minimal Pd loss.

For determining Pd leaching from glass wool during the reaction, the amount of Pd in the products was measured. Two samples were selected from system 2: Sample A corresponding to 150 mL of product solution collected after passing and converting 0.45 mmol of NB through 10 g of fresh catalyst (Pd = 0.35 wt%); Sample B corresponding to 500 mL of product solution collected after passing and converting 2.5 mmol of NB through 10 g of the used catalyst (i.e., catalysts has been used for conversion of 47 mmol of NB in total by the time this aliquot was

sampled). The result of ICP-OES analysis for sample A was 1.9 µg Pd in 150 mL and for sample B was 16.2 µg Pd in 500 mL products. We note that these low Pd values, while an excellent result (minimal leaching) do challenge our ICP-OES analysis and are subject to as much as 40% error.

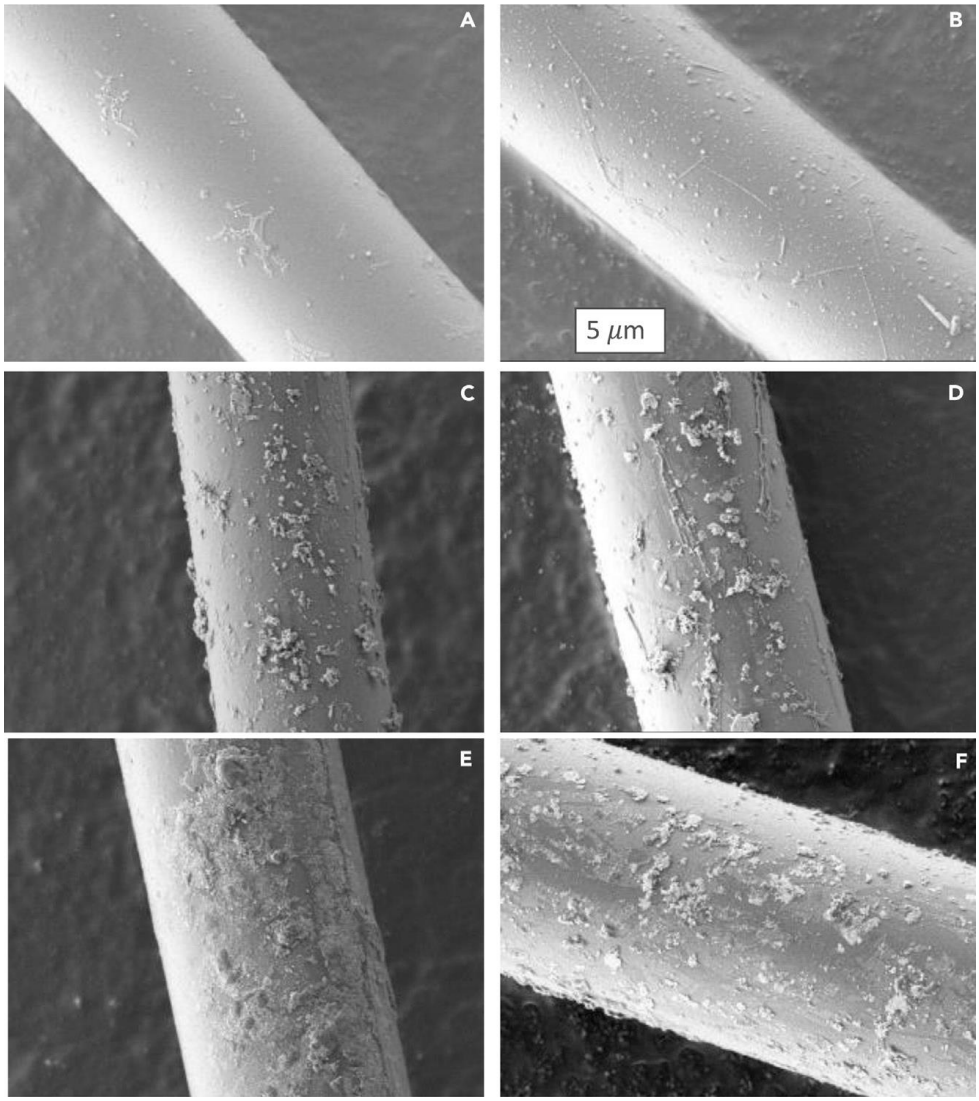

Figure 2.2 SEM images.
(A) non-treated glass fibre, (B) glass fibre treated with APTES, (C) fresh Pd@GW (0.32 wt%), (D) fresh Pd@GW (0.96 wt%), (E) used Pd@GW (0.29 wt%) at the entrance of the flow tube, and (F) used Pd@GW (0.29 wt%) at the exit of the flow tube. The size bar is 5 mm in all panels and the fibers are about 10 mm in diameter. EDS spectra are included in Figures S2.1 and S2.2.

Electron microscopy analysis of the used Pd@GW was also performed. SEM imaging and EDS analyses show that the surface of the glass fibre is covered with Pd particles or clusters even after using this catalyst to convert a total of 47 mmol of NB into aniline during 11 experiments, Figure 2.2. and S 2.1.

2.2.4 Results and Discussion

2.2.4.1 Batch experiments

The batch experiments done in 20 mL glass vials were performed to find the reaction conditions for processing and scaling up the reaction. The reduction of NB to aniline requires the use of a reducing agent as confirmed by a few control experiments. The control experiments were done with and without $NaBH_4$ and catalyst, Table 2.1. Other reductants, i.e., hydrogen and hydrazine, also work and are briefly described later. For this reduction process, $NaBH_4$ was selected as an easy-to-handle reducing agent that is a clean source of hydrogen generated in situ during the reaction.[20]

Table 2.1. Batch experiments for reduction of NB to aniline.

#	$NaBH_4$ eq.	Catalyst	Conversion%[b]
1	100	None	0
2	--	None[c]	0
3	--	Pd@GW[c]	0
4	8	APTES@GW	5
5	1	Pd@GW	9
6	2	Pd@GW	50
7	4	Pd@GW	>99
8	6	Pd@GW	>99
9	8	Pd@GW	>99

[a] Reaction conditions: 40 mg of catalyst and 10 ml of 0.23 mM NB in aqueous solution for 9 minutes (Figure S 2.6); for batch experiments the nominal Pd load was 0.5 wt%. [b] Conversions were determined by UV-Vis spectroscopy. [c] Under UV-A irradiation

The proper amount of $NaBH_4$ was established by a series of batch experiments. For a constant amount of NB (0.23 mM in 10 mL water) and Pd@GW (40 mg) different ratios, between 1 and 10, of $NaBH_4$ were considered. The results showed that the minimum amount of $NaBH_4$ required is 4 equivalents (Table 2.1). $NaBH_4$ interacts with Pd and produces H_2 gas, thus it is possible to have some consumption of reducing agent during the reaction. Therefore, a 1:8 ratio of NB to $NaBH_4$ with an excess amount of $NaBH_4$ was selected for the rest of the experiments, to compensate for H_2 generation. The results of batch experiments gave some important information about the kinetics of the reaction and the capability of moving this process from batch to flow which is illustrated in Figure 2.3.

The high conversion and excellent isosbestic point observed in Figure 2.3 is consistent with a very clean reaction, Scheme 2.1.

2.2.4.2 Flow experiments

The reduction of nitro compounds with a metallic catalyst involves important transformations by heterogeneous mechanisms, where a continuous process combining reaction and separation into one step is a desirable approach.[21] For hydrogen atom transfer from a reducing agent to nitro compounds, adequate contact time on the catalytic site is required. In our case, we designed a packed bed flow reactor by using metal-decorated glass wool that provides a high surface area and readily accessible catalytic sites. The residence time – the time a reagent spends inside the reactor – is obtained by dividing the volume of the flow chamber by the flow rate. A common parameter used for heterogeneous catalysis is the space-time yield (STY) which includes both reaction and reactor efficiency and is given in $gL^{-1}h^{-1}$. The evaluation of STY is more adequate than the comparison between yield or productivity values (yield per time) in long time processes as it incorporates product yield, reactor volume and residence time (SI 2.3.2).[22,23]

The mixing of the solution during the reaction is passive mixing and occurs while pumping of liquid and passing through the glass fibres in the packed bed. The first flow experiments were run in System 1 with 0.8 g of Pd@GW prepared in situ, low concentrations of NB (0.1 mM) and a slow flow rate (2 $mLmin^{-1}$). A 5-fold scale-up reaction (NB concentration of 0.5 mM) was run

at 7.3 mLmin^{-1} flow rate. In this case, for the 0.8 g of catalyst, the reaction STY was 1.2 gL^{-1}h^{-1} under 100% conversion conditions.

A new set-up allowed a significant scale-up of the reaction. For this purpose, two 30 cm tubes (2x System 1) were connected in series and contained a total of 2.1 g of Pd@GW catalyst. The STY of the system was 14.1 gL^{-1}h^{-1} with NB (2 mM) at a flow rate of 33 mLmin^{-1}. Although the generation of H_2 gas causes a small reduction of the effective liquid volume in the short flow tube (System 1), the effect does not cause a significant reduction in STY. In System 2, the tube cross-section is ~2.5 times larger than in System 1, allowing the facile flow of the H_2 gas generated avoiding its accumulation.

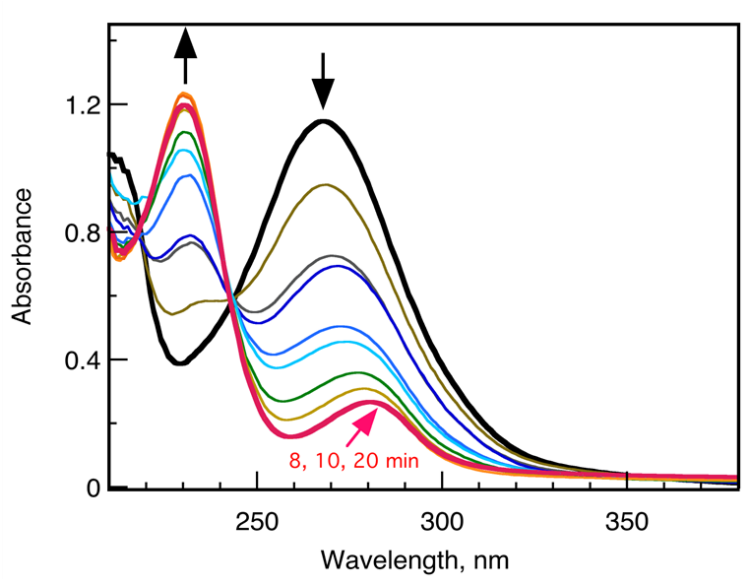

Figure 2.3. UV-Vis spectra of batch experiment
NB (0.14 mM), $NaBH_4$ (0.96 mM), Pd@GW (39.1 mg), dark (black line), and samples were taken every minute for 8 min and then at 10 and 20 min. The reaction was complete in 8 min. The space-time-yield was 0.08 gL^{-1}h^{-1}.

For comparison, two catalysts with different amounts of Pd (0.96 and 0.32 wt%) were utilized in parallel experiments under the same conditions. A high concentration of NB was selected (20 mM) to reduce with 1 g of Pd@GW and a flow rate of 3 mLmin^{-1}. NB conversion for Pd@GW 0.96 and 0.32 wt% was 45.6% and 38.3% respectively.

2.2.4.3 Reaction scale-up

In order to scale up the reaction, a new 150 cm tube with 10 g of catalyst was prepared (System 2). The tube was slightly tilted (up to ~30°) to favour the release of H_2 gas generated inside the reactor.[24] The highest STY obtained was 27.9 $gL^{-1}h^{-1}$ with 100% conversion of NB (3 mM) with a flow rate of 100 $mLmin^{-1}$. By increasing the concentration of NB solutions from 3 mM to 15 mM in System 2 the conversion to aniline was unable to reach 100%. The UV-Vis spectra obtained from reactions run between 10 to 15 mM NB showed an extra peak at 310 nm that was not related to NB (Figure S2.11). This peak was characterized as N-phenylhydroxylamine by mass spectrometry (Figure S2.12), that is, a product of incomplete NB reduction. For an experiment in which 500 mL of 10 mM NB were flowed at a rate of 53 $mLmin^{-1}$, the GC-MS result of products was 95.1% aniline, 0.9% nitrobenzene and 4% N-phenylhydroxylamine, still an excellent conversion to aniline. The appearance of a 310 nm peak in the absorption spectra (N-phenylhydroxylamine) of the products provided a sure sign of some catalyst deactivation. This incomplete reduction suggested catalyst partial deactivation. Indeed, the catalyst was readily regenerated by treatment with 24 mM $NaBH_4$ for 1 h (four 15 min treatments with fresh $NaBH_4$) and then washed with water. To test the treated catalyst, we used again a fresh 3 mM NB solution and a flow rate of 100 $mLmin^{-1}$. This time the conversion was 100% and no hydroxylamine peak at 310 nm was detected.

ICP results suggest that Pd content in the glass wool for the fresh catalyst is 0.32 wt% and after converting 47 mmol of NB (~5.8 g) is 0.29 wt%, this corresponds to 0.28 mmol of Pd. This indicates minimal amounts of Pd could be lost through leaching. Indeed, the analysis of the product solution collected from a freshly prepared catalyst (sample A) suggests only 0.012 ppm of Pd are leached. Further analysis from sample B indicates only up to 0.032 ppm of Pd were detected. Thus, the results suggest that while after multiple uses of Pd@GW, some catalytic sites were deactivated, this was not due to Pd leaching, as the treatment with $NaBH_4$ led to a full activity recovery.

We suggest that the slight performance reduction (i.e., formation of some N-phenylhydroxylamine) at high flow rates may be due to a Pd (0) – Pd (II) redox process at the catalytic centers. We speculate that the reaction of Scheme 2.1 is always accompanied by some Pd (0) →Pd (II) oxidation, which is reversed by the $NaBH_4$ present in the reaction mixture. This

reversal is determined by the $NaBH_4$ concentration and is independent of the flow of catalytic demands of the system. As the catalysis demands of the system increase (higher flow and higher nitro concentration) the in-situ catalyst recovery –regeneration of Pd (0) – fails to keep up and leads to some incomplete reduction. The recovery treatment proposed above and based on $NaBH_4$ treatment allows the Pd (II)→Pd (0) to occur without catalytic load competing with it.

2.2.4.4 Scope

While this contribution centres on commercially important NB, we decided to explore some other nitroaromatics with selected functionalities, among these, several substrates (Scheme 2.2) yielded quantitative conversion, typically in the 30 cm tube mentioned before (System 1). The conditions and flow rates utilized in each system are given in Table 2.2.

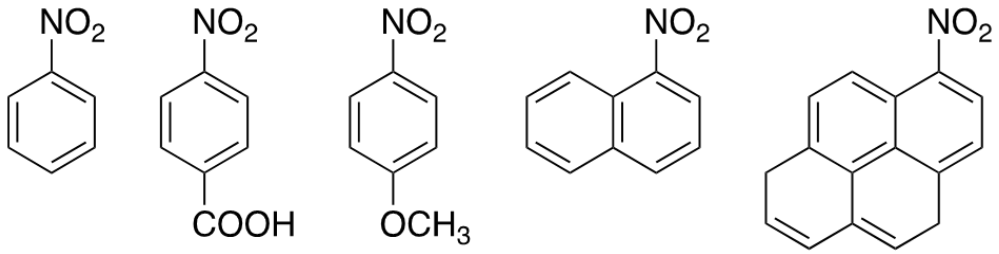

Scheme 2.2. Example of molecules that convert quantitatively to the corresponding amine under flow conditions in water, except for the pyrene derivative examined in methanol.

Table 2.2. Representative flow experiments for reduction of nitro compounds

Reagent	Initial Concentration	Pd@GW amount	Flow rate	Productivity	STY	Time of experiment
Units	mM	g	$mLmin^{-1}$	gh^{-1}	$gL^{-1}h^{-1}$	min
1) Nitrobenzene	0.5	0.8[c]	7.3	0.020	1.2	30
2) Nitrobenzene	1	1[c]	17.2	0.096	5.3	20
3) Nitrobenzene	2	2.1[d]	32.9	0.367	14.1	20
4) Nitrobenzene	3	10[e]	100	1.670	27.9	20
5) Nitrobenzene	15	10[e]	2	0.162	2.7	100
6) Nitrobenzene[f]	15	10[e]	19	1.592	26.5	30
7) Nitrobenzene[f]	100[g]	10[e,h]	3	1.626	27.1	180
8) Nitrobenzene[f]	100[g]	10[e,i]	3.2	1.537	25.6	140
9) 4-Nitrobenzoic acid	0.15	0.5[c]	3.5	0.004	0.3	30
10) 4-Nitroanisole	0.1	0.5[c]	2.3	0.0016	0.1	30

11) 1-Nitronaphthalene	0.1	0.5[c]	5.8	0.005	0.3	20
12) 1-Nitropyrene	0.25	10[e]	57.4	0.185	3.1	20

[a] Reaction conditions: solvents were 5% acetonitrile in aqueous solution except for 1-nitropyrene where the solvent was methanol. >99% conversion for all reagents. [b] Formation to the corresponding aniline determined by UV-Vis spectroscopy. [c] catalyst inside the 30 cm tube, System 1. [d] 2.1 g catalyst inside two connected 30 cm tubes. [e]10 g catalyst inside the 150 cm tube. [f] Reducing reagent is H_2 gas (no $NaBH_4$). [g] solvents were ethanol 50% in water, [h] fresh catalyst with 100% yield, [i] used catalyst with 86% yield was determined with GC-MS analysis.

The last entry in Table 2.2 provides a simple way to visualize the progress of the reaction, as 1-nitropyrene is not fluorescent, while 1-aminopyrene is strongly fluorescent. While the reaction occurs in the dark, weak UVA excitation reveals the progress of the reaction over the 30 cm trajectory of the sample. There is no emission as the sample enters from the right, but emission gradually develops as the reduction progresses and after 20 cm reaches its maximum emission, consistent with the 100% yields observed (Figure 2.4). The reduction of the p-nitrophenol derivative was also explored (Figure. S2.13). As previously reported,[25] further decompositions of the p-aminophenol product under the reaction conditions played an important role (Figure. S2.14).[26,27]

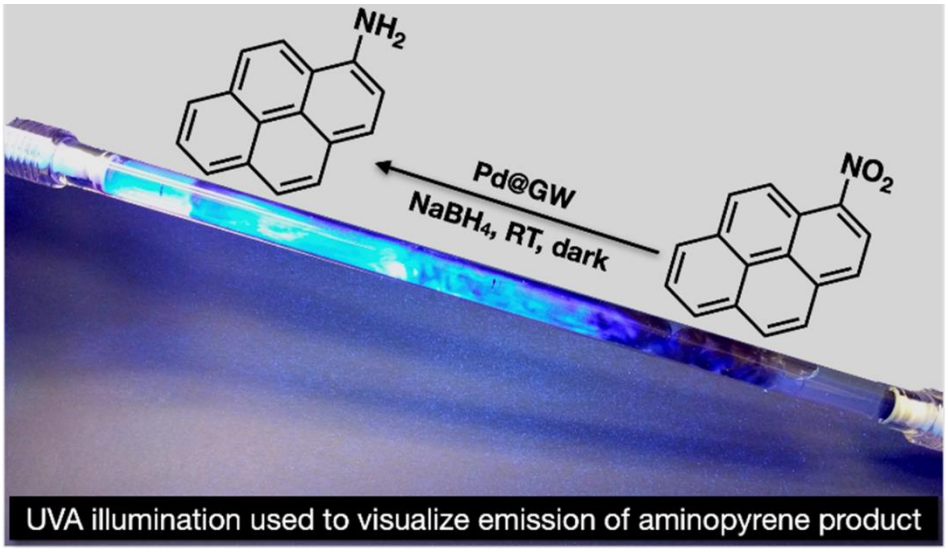

Figure 2.4. Visualized reaction progress
A solution of 0.13 mM 1-nitropyrene and 1.3 mM $NaBH_4$ flows over Pd@GW with a flow rate of 24 $mLmin^{-1}$ (30 cm tube). Weak UVA light illuminates the tube in order to visualize the reaction progress.

2.2.4.5 Beyond $NaBH_4$

Three reducing agents –sodium borohydride, hydrazine, and hydrogen– were compared in continuous flow System 1 with NB (1mM) and flow rates 4 $mLmin^{-1}$. Sodium borohydride showed better results than hydrazine in the long term because of its role in maintaining the catalyst performance. The conversion of NB with hydrazine started to decrease after 10 min (Fig. S2.7). Either hydrogen or $NaBH_4$ acted well as a reducing agent in water and room temperature, then $NaBH_4$ was selected as a safe and clean source of hydrogen generated in situ during the reaction.[20] While in academic labs sodium borohydride is convenient, given the comparable performance, hydrogen gas may be preferred in an industrial setting, as this would reduce the amount of waste generated and the reaction requires neither high pressure nor high temperature.

For higher concentrations of NB, over 12 mM, it is necessary to add cosolvent to dissolve NB in water, therefore, $NaBH_4$ could not act as efficiently as in pure water and affect the reduction process. Table 2.2, entry 4 is for 3 mM NB with STY 27.9 $gL^{-1}h^{-1}$, by increasing the concentration of NB to 15 mM (table 2.2, entry 5) STY dramatically decreased to 2.7 $gL^{-1}h^{-1}$ because $NaBH_4$ is not soluble in cosolvent, acetonitrile. In this situation, changing the reducing reagent to H_2 gas was helpful as the reaction with 15 mM NB was repeated and STY of 26.5 was obtained (table 2.2, entry 6). In another attempt to use a higher concentration of reagent, ethanol was used as a cosolvent and H_2 gas as a reducing agent; 100 mM of NB was converted with fresh catalyst and STY of 27.1 $gL^{-1}h^{-1}$ for 3h (table 2.2, entry 7 and Figure 2.5).

2.2.4.6 Catalyst stability during use and shelf life

In work of this type, typical shelf-life studies tend to be very limited. In this case, the 2020 COVID-19 pandemic forced lab closures and very limited access upon reopening. As a result, one 30 cm column was stored for about 6-8 months with no special precautions, as such storage was forced rather than planned. Solutions of 0.3 to 2 mM nitrobenzene tested after storage showed >99% conversion to aniline, just as they had before storage.

For better comparison, we used 10 g Pd@GW that had been used to convert 130 mmol of NB into aniline during a year and compared it with fresh Pd@GW 0.32 wt%. In this trial, NB 100 mM dissolved in 50 v% aqueous ethanol and was pumped with the average flow rate of 3

mLmin^{-1} in System 2 and H_2 gas as a reducing agent. The yield of aniline according to the GC-MS analysis was ~100% for the fresh catalyst and 86% for the used one, STY 27.1 and 25.6 gL^{-1}h^{-1}, respectively, see Figure 2.5.

The apparent stability of the catalyst, its longevity and performance may hide some migration of Pd atoms or clusters, as recently observed for Pd@TiO_2.[28] However, the sustained performance and minimal leaching suggest that fast Pd redeposition of glass wool minimizes catalyst losses. The GC-MS analysis for the sample of old catalyst in 140 min showed 88.2% aniline, 11.4% nitrobenzene and 0.4% Azoxybenzene. These results mean that the decrease of aniline yield is caused by the decrease of nitrobenzene conversion and by the formation of a side product.

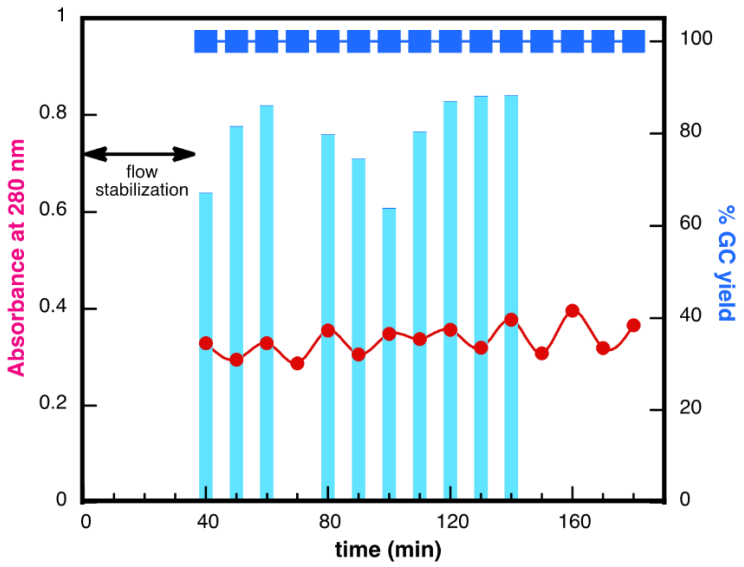

Figure 2.5. Stability in long-term reaction
Ethanol (50%) was used as a cosolvent and H_2 gas as a reducing agent; 100 mM of NB was converted with fresh catalyst and STY of 27.1 gL^{-1}h^{-1}. The graph (red, left axis) shows the stability of samples collected at different times, where most of the absorbance fluctuations (0.34 ± 0.04) are because of sampling, dilution, and measurement factors. The right axis refers to yield as determined by GC. For fresh catalyst, the yield was 100% (dark blue squares) throughout the reaction. Note that it takes about 30 min for the first drops of reaction to exit the tube while starting with a tube containing no liquid. For an old (>11 months) used catalyst, the light blue bars show the yields obtained, fluctuating between 64 and 88% while sampling at different times.

2.2.5 Conclusion

The NB to aniline reduction is a major industrial process and the main use of NB worldwide, and a key step in the production of polyurethanes. The catalytic process reported here is easily scalable, and operates under exceptionally mild conditions, such as atmospheric pressure, room temperature and aqueous solution. The process started in batch with STY 0.08 $gL^{-1}h^{-1}$ and scaled up to ~28 $gL^{-1}h^{-1}$ in the continuous flow system. While the catalyst uses Pd, its loading (0.32 wt%) is lower than usually required (as much as 7 wt%),[11,14,15] and reusable many times. Further, in our synthesis, ~92% of the Pd used is retained in the catalyst. The catalyst is also very robust, through numerous experiments, we never got to deactivate the catalyst, beyond requiring a brief recovery by flowing a $NaBH_4$ solution. While $NaBH_4$ provides a good reductant for laboratory screening, hydrogen works extremely well under the same mild conditions and should be the preferred reductant in an industrial setting. Glass wool provides a readily available and inexpensive material that can be used as a support, leading to a catalyst that permits easy flow around it, without being lost by the active flow. Further, the Pd@GW catalyst can be readily synthesized in-situ under UVA exposure, thus adding convenience to the overall process. While this contribution centers on the commercially important nitrobenzene to aniline reduction, a modest exploration of the scope (Table 2.2) shows that the reaction is quite general.

2.3 Post-print Version of Supplementary Information

Table S 2.1. Key Resources

REAGENT or RESOURCE	SOURCE	IDENTIFIER
Chemicals		
3-Aminopropyl)triethoxysilane	Sigma Aldrich	Cas# 919-30-2
Palladium(II) acetylacetonate	Sigma Aldrich	CAS# 14024-61-4
Sodium borohydride	Sigma Aldrich	CAS# 16940-66-2
Nitrobenzene	Sigma Aldrich	CAS# 98-95-3
Aniline	Sigma Aldrich	CAS# 62-53-3
4-Nitrobenzoic acid	Sigma Aldrich	CAS# 62-23-7
4-Nitroanisole	Sigma Aldrich	CAS# 100-17-4
1-Nitronaphthalene	Sigma Aldrich	CAS# 86-57-7
1-Nitropyrene	Sigma Aldrich	CAS# 5522-43-0

Nitrophenol	Sigma Aldrich	CAS# 554-84-7
Irgacure 2959	BASF	Cat# 55047962
Ethanol	Fisher chemical	CAS# 64-17-5
Acetonitrile	Fisher chemical	CAS# 75-05-8
Hydrogen	Messer	CAS# 1333-74-0
Other		
Non-treated glass wool	Sigma Aldrich	SKU-Pack Size: 20384
Glass tube 30 cm	Ace glass	5815-03
Glass tube 150 cm	Macalaster Bicknell	244140
UVA lamp 8W	Luzchem	LZC-UVA
UVA lamp 40W	General Electric	F40BLB-6PK
Pump	Masterflex	7525-34
Expo panel	Luzchem	EXPO-01

2.3.1 Method details

2.3.1.1 Glass wool pre-treatment

Non-treated glass wool from Sigma Aldrich was immersed in 1% (3-Aminopropyl) triethoxysilane (APTES) solution in toluene and refluxed overnight. After cooling down to room temperature, the glass wool was removed from the flask and rinsed with toluene (3x) and acetone (3x). The APTES treated glass wool was dried in an oven at 100 °C overnight.[16]

2.3.1.2 Synthesis of Pd@GW

APTES treated GW (1g) was placed inside a 30 cm tube (ID = 10 mm), ensuring homogeneous distribution of the GW to provide good light penetration inside the tube. A solution with 15 mg of palladium (II) acetylacetonate ($Pd(acac)_2$) – accounting for 0.5 wt% Pd@GW) and 60 mg of Irgacure 2959 (I-2959) – photoinitiator is shown in scheme S2.1 – in 26 mL of ethanol was prepared and injected inside the tube. Two sides of the tube were sealed and irradiated with a Luzchem Expo panel fitted with 5 T5 UVA bulbs (LZC-UVA, 8W each) for 210 min and rotated on a hot-dog cooker for homogeneous mixing. The obtained gray glass wool was washed with ethanol inside the tube to remove the unreacted $Pd(acac)_2$ and photoinitiator debris and dried at room temperature. The Pd@GW catalyst was characterized by SEM, XPS and ICP-OES. (See scheme S2.1, figure 2.1, 2.2, S2.1, S2.2, and S2.4)

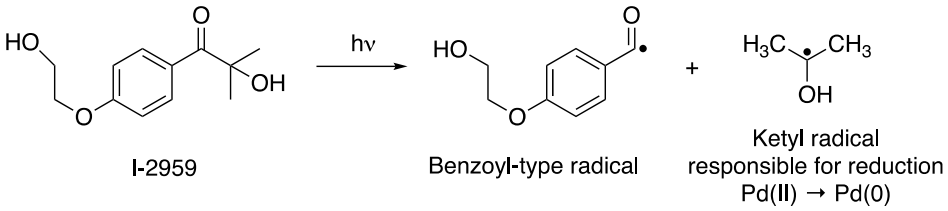

Scheme S 2.1. I-2959 photoinitiator reaction generates highly reducing species (ketyl radical) capable of reducing Pd(II).

2.3.1.3 Large-scale synthesis of Pd@GW

Using the method described above, 10 g of APTES@GW were placed inside a 150 cm tube (ID = 13 mm) and a solution with 100 mg palladium (II) acetylacetonate ($Pd(acac)_2$) – for a nominal 0.35 wt% Pd@GW, and 400 mg of I-2959 in 165 ml ethanol was prepared and injected inside the tube. Two sides of the tube were sealed and irradiated with 4 UV-A bulbs (40 W) for 270 min. The tube was manually rotated every 15 min to ensure a homogeneous mix. The obtained Pd@GW was washed with ethanol and dried at room temperature. (See figure S2.5)

A B

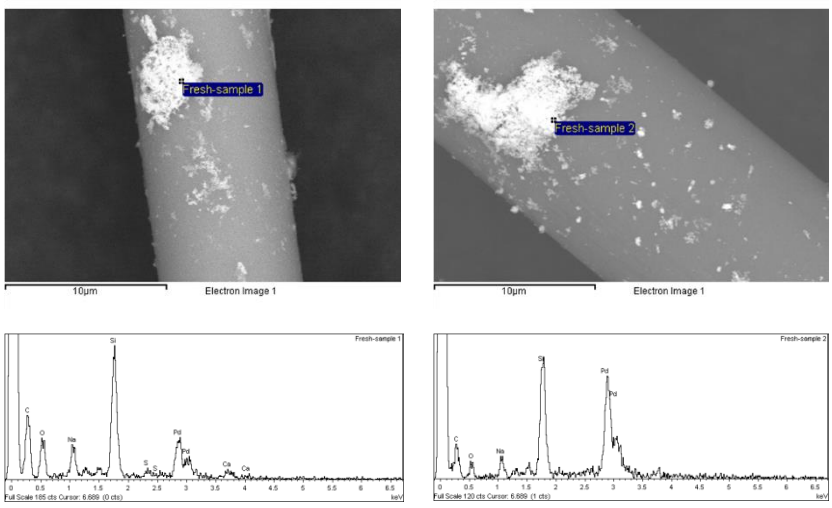

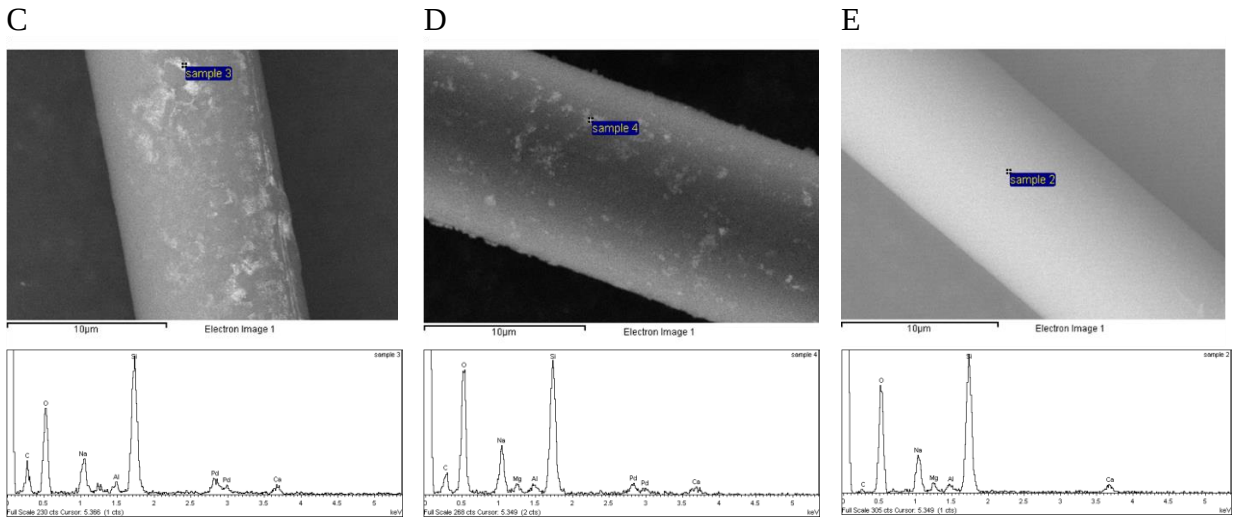

Figure S 2.1. EDS spectrum (bottom) for the selected region (top) for (A) fresh Pd@GW with 0.32 w% pd, (B) fresh Pd@GW with 0.96 w% pd, (C) used Pd@GW at the entrance of the flow tube and (D) used Pd@GW at the exit of the flow tube, (E) glass fibre treated with APTES. Related to figure 2.2.

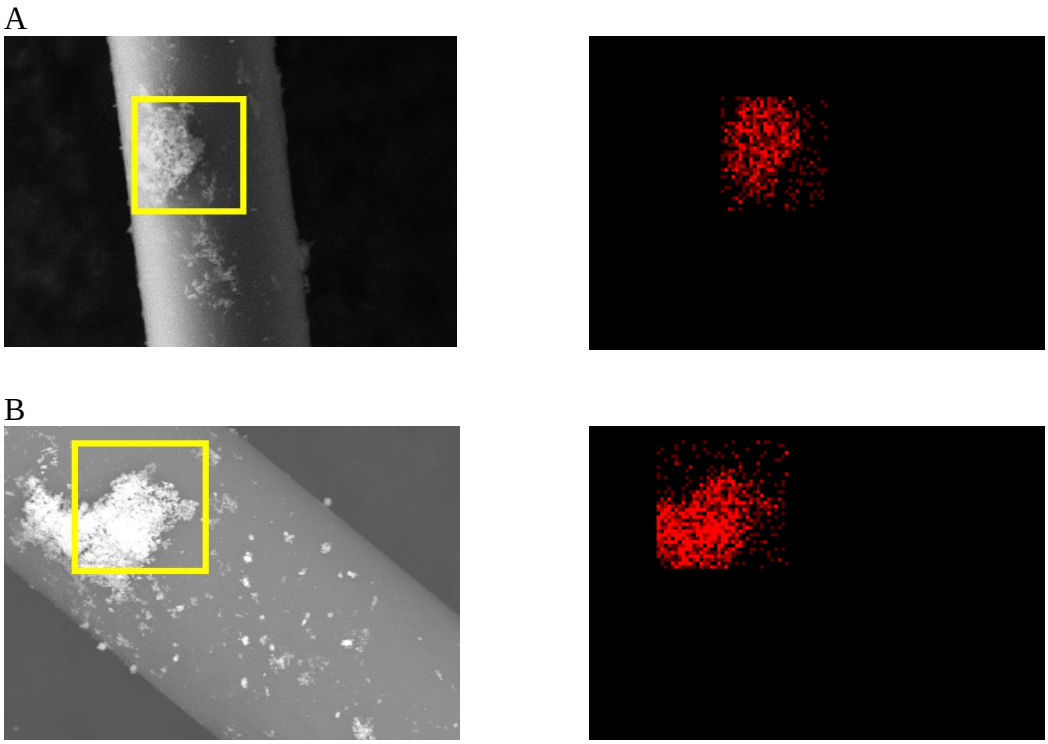

Figure S 2.2.SEM elemental mapping (A) fresh Pd@GW with 0.32 w% Pd, (B) fresh Pd@GW with 0.96 w% Pd. Related to Figure 2.2.

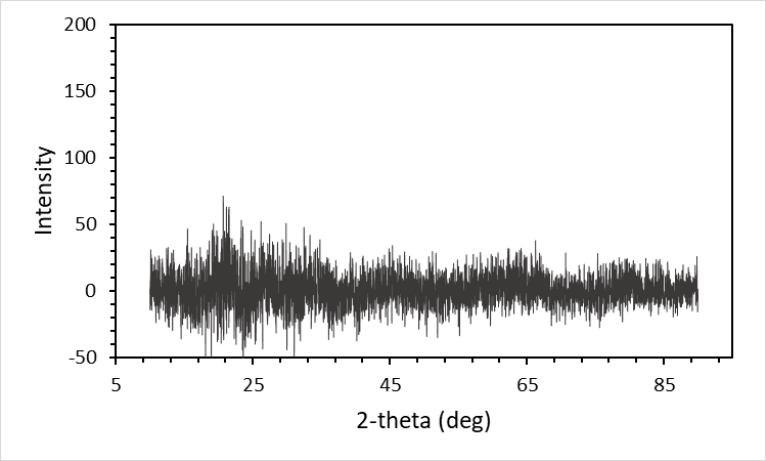

Figure S 2.3.XRD pattern of Pd@GW with 0.35 w% loading of Pd on the GW. Peaks of Pd are not detectable due to the low amount of Pd on the GW and small particle size that made the peaks very broad.

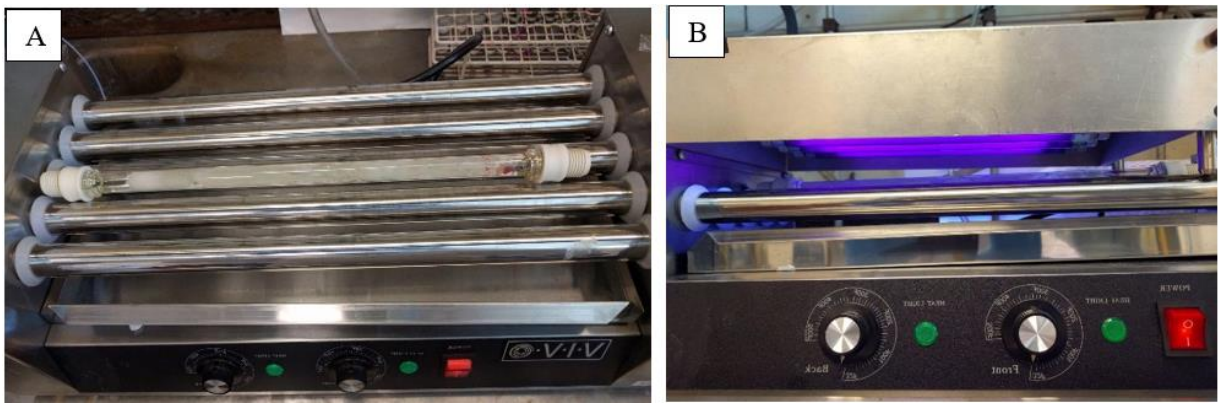

Figure S 2.4.In-situ photochemical synthesis of Pd@GW in a 30 cm tube, (A) glass wool and Pd solution inside the tube on the rotator (before irradiation), (B) irradiating with an Expo panel from Luzchem fitted with five UVA lamps.

Figure S 2.5. 150 cm length glass tube tilted at around 30◦. A miniature peristaltic pump was used for this experiment.

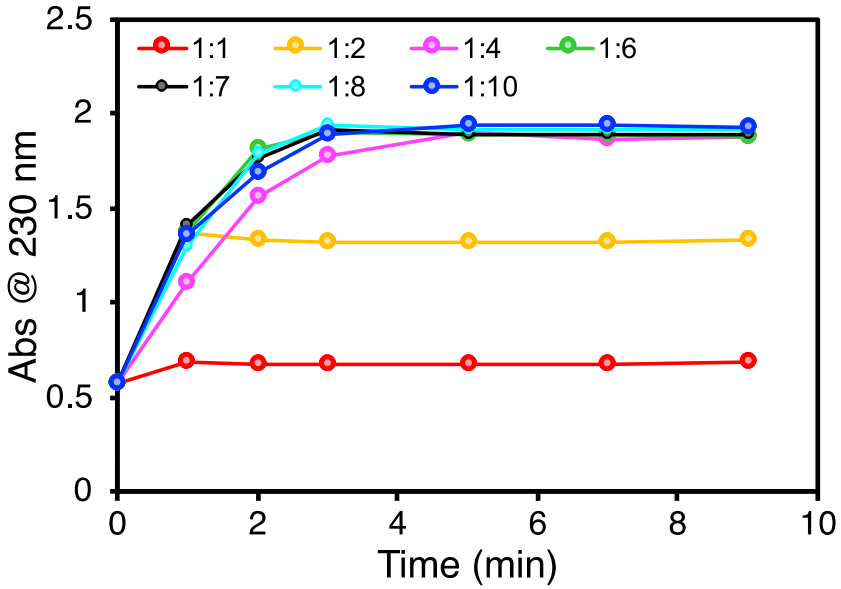

Figure S 2.6. Batch experiments of reduction of nitrobenzene (NB, 228 µM) in aqueous solution in the presence of Pd@GW and different concentrations of $NaBH_4$ (legend indicates NB: $NaBH_4$ ratio).

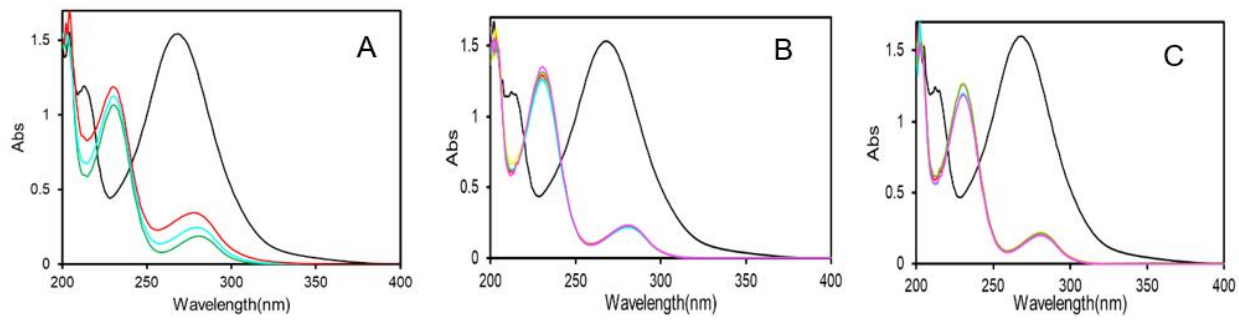

Figure S 2.7. Flow experiments of reduction of nitrobenzene (1 mM) in aqueous solution in the presence of Pd@GW (1 g) and flow rate of 4 mLmin-1 with different reducing agents: (A) N_2H_4 (10 mM) (B) $NaBH_4$ (10 mM) (C) H_2 gas. The time of the experiment was 20 min and samples were taken every 3 min. Related to Table 2.2.

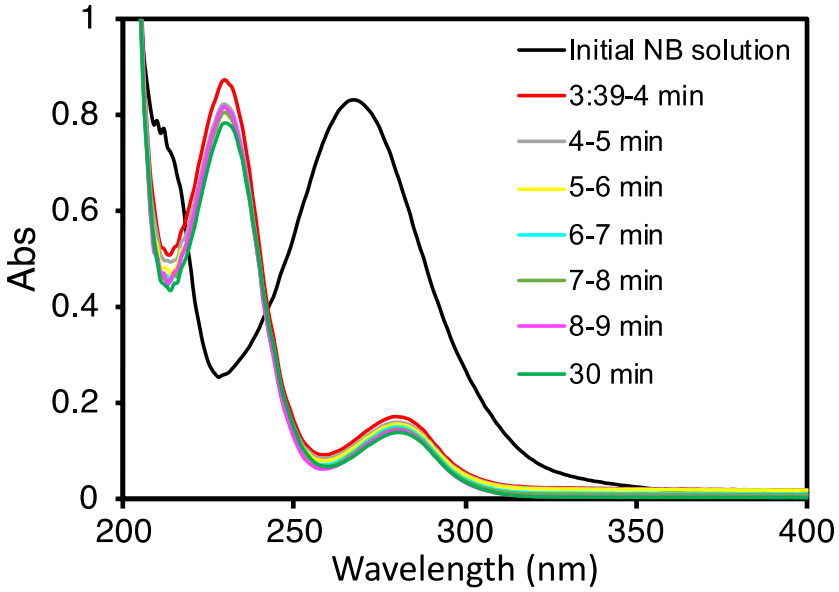

Figure S 2.8. Reduction of nitrobenzene (NB) solution (0.5 mM) under flow conditions: $NaBH_4$ (4 mM), Pd@GW (0.83 g), flow speed 7.3 mL/min in 30 cm tube. Related to Table 2.2.

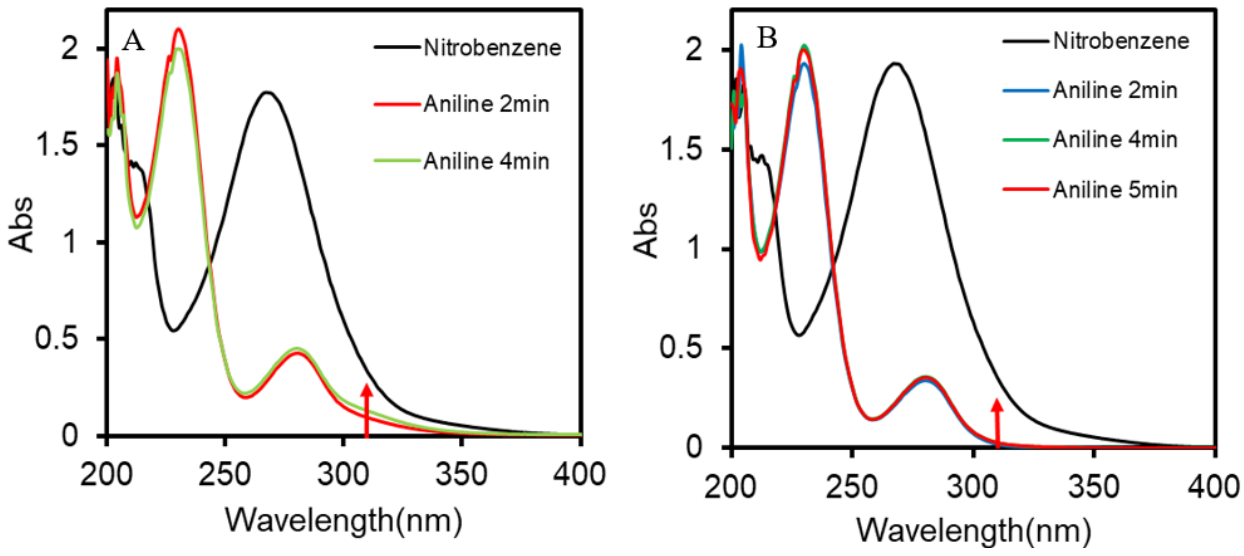

Figure S 2.9. Large-scale reduction of nitrobenzene (NB, 3 mM), $NaBH_4$ (24 mM), 150 cm tube with Pd@GW (10 g), at flow rate equals to 100 $mLmin^{-1}$; before (A) and after (B) $NaBH_4$ treatment. Samples were diluted 11 times before measuring UV-vis spectra. The first sample was taken after 2 min of pumping.

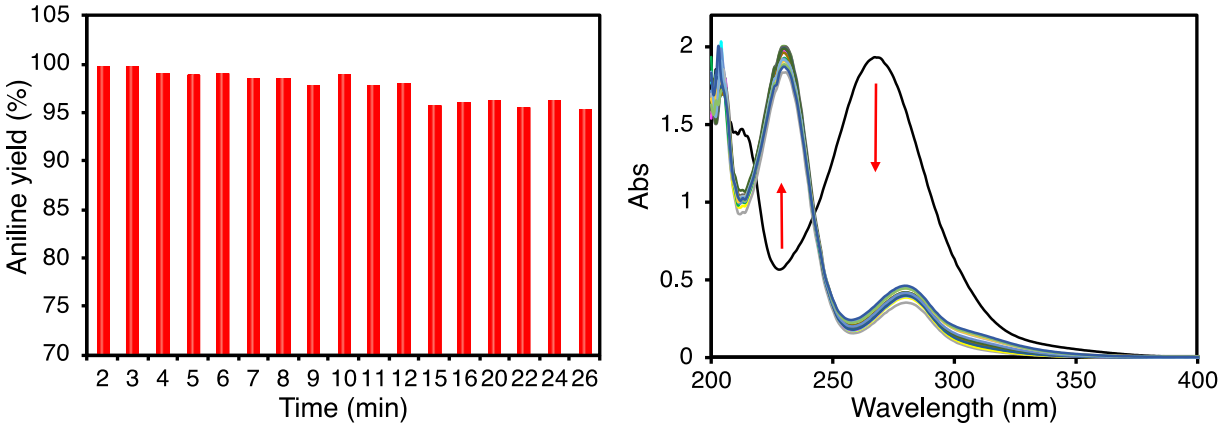

Figure S 2.10. Nitrobenzene (NB, 3 mM), $NaBH_4$ (24 mM), and Pd@GW (10 g) with a flow speed of (77 mL/min) monitored for a total volume flown of about 2 L. Samples were diluted 11 times and analyzed by UV-Vis spectroscopy. Left: Percentage of aniline yield as a function of time; right: UV-Vis spectrum during the reaction.

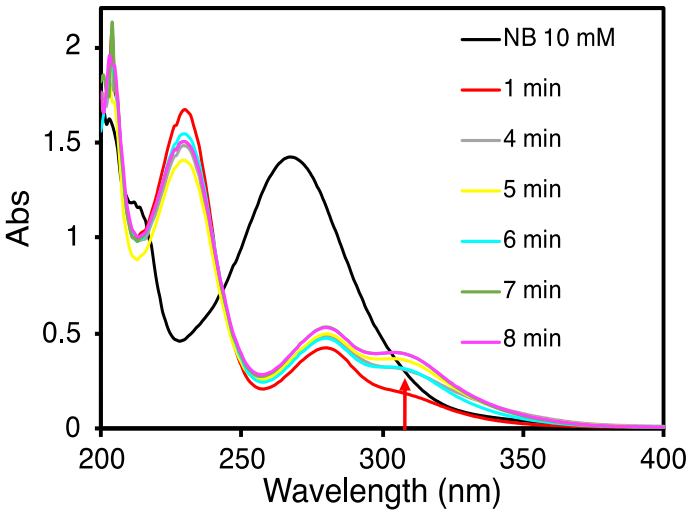

Figure S 2.11. Formation of by-product N-phenylhydroxylamine (formation of band absorption around 310 nm – red arrow) during flow experiments of catalysts used 6 times before. Nitrobenzene (10 mM), $NaBH_4$ (80 mM), Pd@GW (10 g), flow rate (53 mL/min). Single path. Samples were diluted 41 times for UV-Vis spectroscopy analysis. Related to Figure 2.1.

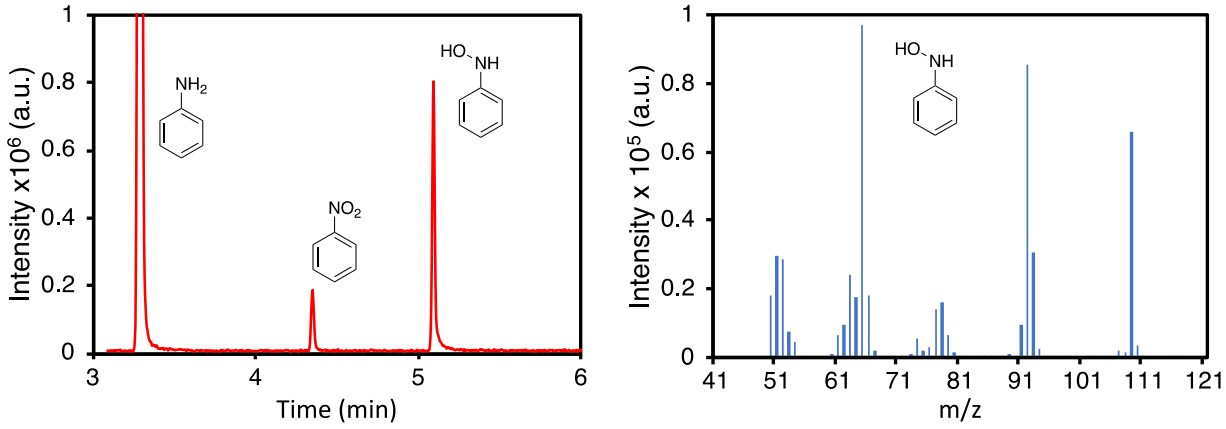

Figure S 2.12. Formation of by-product N-phenylhydroxylamine under the following flow reaction conditions: 500 ml of 10 mM nitrobenzene solution flowing at a rate of 53 mL/min using 10 g of Pd@GW catalyst. Left: GC-MS chromatograph. Right: MS spectrum.

2.3.2 Calculation of space-time yield

$$\mathrm{STY} = \frac{\mathrm{Q} \cdot \mathrm{C_{NB}} \cdot \mathrm{X_{NB}} \cdot \mathrm{S_{A,NB}} \cdot \mathrm{M_{An}}}{\mathrm{V_{reac}}} = \frac{\mathrm{C_{NB}} \cdot \mathrm{X_{NB}} \cdot \mathrm{S_{A,NB}} \cdot \mathrm{M_{An}}}{\tau}$$

Q = Volumetric flow rate ($L.h^{-1}$)

CNB = Concentration of nitrobenzene (M)

XNB = Conversion of NB

SA = selectivity to aniline

MAn = molar mass of aniline ($g.mol^{-1}$)

Vreac = reaction volume (L)

τ = residence time (h)

For example, the residence time of the solution of nitrobenzene 3 mM on the surface of a 10 g catalyst with a flow rate of 100 $mLmin^{-1}$ is roughly 0.01 h. By considering the full conversion of NB to aniline, the values of XNB and SA are 1.

$$\mathrm{STY} = \frac{0.003\ \mathrm{mol.\,L^{-1}} \cdot 93.13\ \mathrm{g.\,mol^{-1}}}{0.01\mathrm{h}} = 27.94\ \mathrm{g.\,L^{-1}.\,h^{-1}}$$

2.3.3 Scope of the reaction

Reduction of nitro compounds with Pd@GW was done successfully for nitrobenzene, 4-nitrobenzoic acid, 4-nitroanisole, 1-nitronaphthalene, and 1-nitropyrene; however, nitrophenol reduction showed different results. Reduction of nitrophenol (0.45 mM) with 40 mg of Pd@GW in batch yielded 100% conversion to aminophenol, but under flow conditions (500 mg of catalyst, flow rate 2.1 mL/min), another peak appeared, suggesting that under prolonged catalyst exposure, phenols may undergo other changes. The matter was not pursued any further (see Figure S2.13 and S2.14).[26,27]

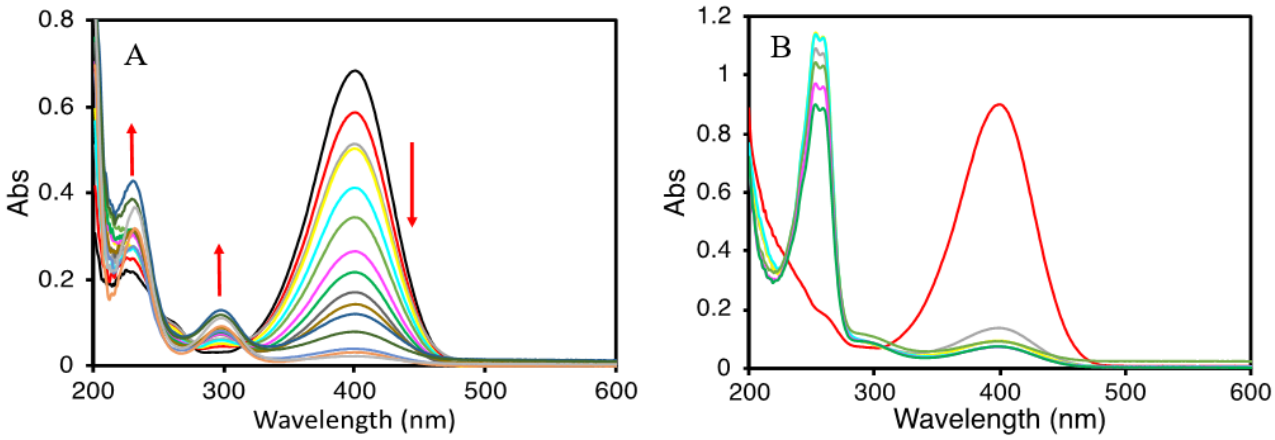

Figure S 2.13. Reduction of p-nitrophenol (0.45 mM, pH = 5.5) under batch (A) or flow conditions (B). (A) In the batch experiment, samples were taken every 10 minutes for 140 minutes. (B) flow experiment with a flow rate of 2.1 mL/min, after 10 minutes of pumping, samples were taken every 2 minutes. Residence time was 10 minutes. Related to Table 2.2.

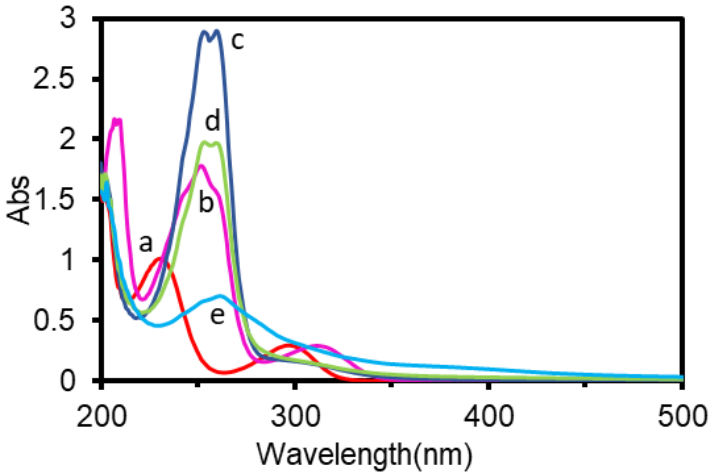

Figure S 2.14. Decomposition of p-aminophenol at pH = 10 under air. UV-Vis spectrum of p-aminophenol (0.1 mM) at pH = 5.5(a), and evolution of the UV-Vis spectra of p-aminophenol (0.1 mM) after exposure to air under pH = 10 from 0 to 150 min (b, c, d, and e). Decomposition of the p-aminophenol product in different reaction conditions has been reported in different research.[26,27]

2.4 Accompaniment to Chapter

A catalyst based on palladium supported on glass wool (Pd@GW) demonstrates exceptional performance and durability for the reduction of nitrobenzene to aniline. This reaction proceeds efficiently at room temperature and ambient pressure in aqueous solutions, highlighting the catalyst's potential for green chemistry applications.[29]

The outcomes of this project not only heightened my enthusiasm for working in this field and deepened my understanding of reaction condition optimization, but also opened new avenues for our entire research group. This breakthrough enabled the optimization of various organic reactions and antibacterial studies using flow systems.

Building upon this work, subsequent research within our group, notably by Bowen Wang and Connor Bourgonje, further advanced our understanding of the Pd@GW catalyst. Their study employed advanced microscopy techniques to observe palladium catalytic centers on fibreglass during the reduction of nitro compounds. By combining fluorescence and electron microscopy, they achieved real-time, high-resolution visualization of these catalytic centers. This approach revealed detailed insights into the behaviour and stability of the catalyst under flow conditions. Importantly, their findings demonstrated minimal palladium migration and identified specific active sites that enhance catalytic activity, contributing significantly to the improvement of heterogeneous catalysts.[30]

The synergy between the findings in Chapter 2, which explored the reduction of nitro to amine using Pd@GW in a flow system, and Bowen's microscopy studies resulted in a comprehensive publication. Titled "The Nitro to Amine Reduction: From Millions of Tons to Single Molecule Studies," this paper bridges the gap between large-scale industrial applications and molecular-level insights, highlighting the multifaceted and interdisciplinary nature of the research.[31]

2.5 References

(1) Colom, J.; Llobet, A.; Pla-Quintana, A.; Roglans, A. Preparation of Aniline Derivatives: An Advanced Undergraduate Laboratory Experiment Exploring Catalytic and Stoichiometric Reaction Methodologies. *J. Chem. Educ.* **2002**, *79* (6), 731.

(2) Fieser, L. F. *Experiments in Organic Chemistry*, 2nd ed.; Heath, 1941.

(3) Orlandi, M.; Brenna, D.; Harms, R.; Jost, S.; Benaglia, M. Recent Developments in the Reduction of Aromatic and Aliphatic Nitro Compounds to Amines. *Org. Process Res. Dev.* **2018**, *22* (4), 430–445. https://doi.org/10.1021/acs.oprd.6b00205.

(4) Amini, B.; Lowenkron, S. Aniline and Its Derivatives. In *Kirk-Othmer Encyclopedia of Chemical Technology*; John Wiley & Sons, Ltd, 2003.

(5) *Annalen der Chemie und Pharmacie: vereinigte Zeitschrift des Neuen Journals der Pharmacie für Ärzte, Apotheker und Chemiker u. des Magazins für Pharmacie und Experimentalkritik*; Winter, 1842.

(6) *Annales de chimie et de physique*. Gallica. https://gallica.bnf.fr/ark:/12148/bpt6k347830 (accessed 2024-04-14).

(7) Goszewska, I.; Giziński, D.; Zienkiewicz-Machnik, M.; Lisovytskiy, D.; Nikiforov, K.; Masternak, J.; Śrębowata, A.; Sá, J. A Novel Nano-Palladium Catalyst for Continuous-Flow Chemoselective Hydrogenation Reactions. *Catal. Commun.* **2017**, *94*, 65–68. https://doi.org/10.1016/j.catcom.2017.02.014.

(8) Moghaddam, M. M.; Pieber, B.; Glasnov, T.; Kappe, C. O. Immobilized Iron Oxide Nanoparticles as Stable and Reusable Catalysts for Hydrazine-Mediated Nitro Reductions in Continuous Flow. *ChemSusChem* **2014**, *7* (11), 3122–3131. https://doi.org/10.1002/cssc.201402455.

(9) Gholinejad, M.; Oftadeh, E.; Shojafar, M.; Sansano, J. M.; Lipshutz, B. H. Synergistic Effects of Ppm Levels of Palladium on Natural Clinochlore for Reduction of Nitroarenes. *ChemSusChem* **2019**, *12* (18), 4240–4248. https://doi.org/10.1002/cssc.201901535.

(10) Feng, J.; Handa, S.; Gallou, F.; Lipshutz, B. H. Safe and Selective Nitro Group Reductions Catalyzed by Sustainable and Recyclable Fe/Ppm Pd Nanoparticles in Water at Room Temperature. *Angew. Chem.* **2016**, *128* (31), 9125–9129. https://doi.org/10.1002/ange.201604026.

(11) Cossaboon, K. F. Hydrogenation of Mixed Aromatic Nitrobodies. US4185036A, January 22, 1980. https://patents.google.com/patent/US4185036A/en (accessed 2024-04-13).

(12) Hassan, A.; Bagherzadeh, E.; Anthony, R. G.; Borsinger, G. G.; Hassan, A. System and Process for Production of Aniline and Toluenediamine. US8153076B2, April 10, 2012. https://patents.google.com/patent/US8153076B2/en (accessed 2024-04-14).

(13) Formenti, D.; Ferretti, F.; Scharnagl, F. K.; Beller, M. Reduction of Nitro Compounds Using 3d-Non-Noble Metal Catalysts. *Chem. Rev.* **2019**, *119* (4), 2611–2680. https://doi.org/10.1021/acs.chemrev.8b00547.

(14) Yamada, T.; Jiang, J.; Ito, N.; Park, K.; Masuda, H.; Furugen, C.; Ishida, M.; Ōtori, S.; Sajiki, H. Development of Facile and Simple Processes for the Heterogeneous Pd-

Catalyzed Ligand-Free Continuous-Flow Suzuki–Miyaura Coupling. *Catalysts* **2020**, *10* (10), 1209. https://doi.org/10.3390/catal10101209.

(15) Ichitsuka, T.; Suzuki, N.; Sairenji, M.; Koumura, N.; Onozawa, S.; Sato, K.; Kobayashi, S. Readily Available Immobilized Pd Catalysts for Suzuki-Miyaura Coupling under Continuous-Flow Conditions. *ChemCatChem* **2019**, *11* (10), 2427–2431. https://doi.org/10.1002/cctc.201900085.

(16) Elhage, A.; Wang, B.; Marina, N.; Marin, M. L.; Cruz, M.; Lanterna, A. E.; Scaiano, J. C. Glass Wool: A Novel Support for Heterogeneous Catalysis. *Chem. Sci.* **2018**, *9* (33), 6844–6852. https://doi.org/10.1039/C8SC02115E.

(17) Teixeira, R. I.; Lucas, N. C. de; Garden, S. J.; Lanterna, A. E.; Scaiano, J. C. Glass Wool Supported Ruthenium Complexes: Versatile, Recyclable Heterogeneous Photoredox Catalysts. *Catal. Sci. Technol.* **2020**, *10* (5), 1273–1280. https://doi.org/10.1039/C9CY02479D.

(18) Lipshutz, B. H.; Ghorai, S.; Cortes-Clerget, M. The Hydrophobic Effect Applied to Organic Synthesis: Recent Synthetic Chemistry "in Water." *Chem. – Eur. J.* **2018**, *24* (26), 6672–6695. https://doi.org/10.1002/chem.201705499.

(19) Lippincott, D. J.; Landstrom, E.; Cortes-Clerget, M.; Lipshutz, B. H.; Buescher, K.; Schreiber, R.; Durano, C.; Parmentier, M.; Ye, N.; Wu, B.; Shi, M.; Yang, H.; Andersson, M.; Gallou, F. Surfactant Technology: With New Rules, Designing New Sequences Is Required! *Org. Process Res. Dev.* **2020**, *24* (5), 841–849. https://doi.org/10.1021/acs.oprd.9b00454.

(20) K. Kadam, H.; G. Tilve, S. Advancement in Methodologies for Reduction of Nitroarenes. *RSC Adv.* **2015**, *5* (101), 83391–83407. https://doi.org/10.1039/C5RA10076C.

(21) Plutschack, M. B.; Pieber, B.; Gilmore, K.; Seeberger, P. H. The Hitchhiker's Guide to Flow Chemistry. *Chem. Rev.* **2017**, *117* (18), 11796–11893. https://doi.org/10.1021/acs.chemrev.7b00183.

(22) Hessel, V.; Löwe, H.; Hardt, S. *Chemical Micro Process Engineering: Fundamentals, Modelling and Reactions*; John Wiley & Sons, 2004.

(23) Bayer, P.; Wangelin, A. J. von. An Entirely Solvent-Free Photooxygenation of Olefins under Continuous Flow Conditions. *Green Chem.* **2020**, *22* (8), 2359–2364. https://doi.org/10.1039/D0GC00436G.

(24) Greco, R.; Goessler, W.; Cantillo, D.; Kappe, C. O. Benchmarking Immobilized Di- and Triarylphosphine Palladium Catalysts for Continuous-Flow Cross-Coupling Reactions: Efficiency, Durability, and Metal Leaching Studies. *ACS Catal.* **2015**, *5* (2), 1303–1312. https://doi.org/10.1021/cs5020089.

(25) Mitchell, S.; Waring, R. Aminophenols. In *Kirk-Othmer Encyclopedia of Chemical Technology*; John Wiley & Sons, Ltd, 2000. https://doi.org/10.1002/0471238961.0113091413092003.a01.

(26) Ahmed, M.; Khan, Z. H. Electronic Absorption Spectra of Benzoquinone and Its Hydroxy Substituents and Effect of Solvents on Their Spectra. *Spectrochim. Acta. A. Mol. Biomol. Spectrosc.* **2000**, *56* (5), 965–981. https://doi.org/10.1016/S1386-1425(99)00190-0.

(27) de Souza, J. C.; Zanoni, M. V. B.; Oliveira-Brett, A. M. Genotoxic Permanent Hair Dye Precursors *p*-Aminophenol and *p*-Toluenediamine Electrochemical Oxidation Mechanisms and Evaluation in Biological Fluids. *J. Electroanal. Chem.* **2020**, *857*, 113509. https://doi.org/10.1016/j.jelechem.2019.113509.

(28) Costa, P.; Sandrin, D.; Scaiano, J. C. Real-Time Fluorescence Imaging of a Heterogeneously Catalysed Suzuki–Miyaura Reaction. *Nat. Catal.* **2020**, *3* (5), 427–437. https://doi.org/10.1038/s41929-020-0442-0.

(29) Yaghmaei, M.; Lanterna, A. E.; Scaiano, J. C. Nitro to Amine Reductions Using Aqueous Flow Catalysis under Ambient Conditions. *iScience* **2021**, *24* (12). https://doi.org/10.1016/j.isci.2021.103472.

(30) Wang, B.; Bourgonje, C. R.; Scaiano, J. C. Fiber-Glass Supported Catalysis: Real-Time, High-Resolution Visualization of Active Palladium Catalytic Centers during the Reduction of Nitro Compounds. *Catal. Sci. Technol.* **2023**, *13* (4), 1021–1031. https://doi.org/10.1039/D2CY01857H.

(31) Scaiano, J. C.; Wang, B.; Bourgonje, C. R.; Yaghmaei, M. The Nitro to Amine Reduction: From Millions of Tons to Single Molecule Studies. *Pure Appl. Chem.* **2023**, *95* (8), 913–920. https://doi.org/10.1515/pac-2023-0111.

Chapter 3. A simple Norrish Type II actinometer for flow photoreactions

3.1 Preamble to Chapter

In the specialized field of photochemistry, the design of a flow setup and subsequent scale-up significantly differs from traditional methods used in organic synthesis, primarily due to the critical role of light. An effective flow system optimizes the interaction between light and the reactants, ensuring maximum exposure. The ideal reactor with a large surface area is exposed to the light source, facilitating efficient photochemical reactions. Additionally, the volume of the solution positioned in front of the light source should not exceed the distance over which light intensity significantly diminishes, known as the attenuation length. This consideration is crucial for maintaining effective light penetration and ensuring that the photochemical reactions occur uniformly throughout the solution.

Furthermore, achieving optimal efficiency in a photochemical flow reactor depends on precisely managing the ratio of the reactor's exposed surface area to the volume of the reacting solution. This design strategy maximizes the utilization of photons by ensuring that more reactants come into contact with the light. The reactor geometry needs to support a thin layer of solution, effectively spreading the solution across a broader area while minimizing the depth exposed to the light. This configuration reduces the light path length through the solution, which minimizes losses due to absorption and scattering, and ensures a more uniform distribution of light.

To further enhance the effectiveness of the photochemical process, we must also consider the optical properties of the reactor materials and the solvent. These materials should be chosen not only for their chemical compatibility and durability but also for their transparency and minimal interference with light transmission. The setup of the light source itself, including its wavelength, intensity, and positioning relative to the reactor, is another critical factor that needs careful adjustment to align with the specific photochemical reaction being conducted.

By considering all those factors, we designed a flow setup that can significantly increase the efficiency and scalability of the chemistry processes. This chapter explores the specifics of the setup, and the quantum yields of several chemicals determined using a chemical actinometer.

3.2 Post-print version of the manuscript

First published in Photochemical & Photobiological Sciences. 2023;22(8):1865-74

This chapter has been adapted from Photochemical & Photobiological Sciences journal with permission as the author of this article.

3.2.1 Abstract

This contribution addresses a frequent problem in flow photochemistry, where methodologies to determine the quantum efficiency of photoreactions are totally lacking. Despite numerous studies being available in the literature, product reaction yields are never accompanied by measurements to determine their quantum yields. Frequently, the key reagent in the reaction, light, is not measured under the experimental conditions of exposure. We report here a flow actinometer based on the photochemistry of valerophenone that can be readily implemented in the organic laboratory for irradiations in the UV region. For example, for UVB lamps used in our work, the irradiance was measured as 1.1×10^{-4} einstein l^{-1} s^{-1}. Our photoreactor design involves wrapping low-pressure lamps with Teflon tubbing, where the photochemistry takes place. Similar strategies could be implemented with other geometries or with lamps (e.g. LED) and actinometers with sensitivity in other spectral regions.

3.2.2 Introduction

Actinometers are employed to determine the irradiance to which a sample is exposed, sometimes expressed per unit area and frequently based on volume.[1–3] Actinometers can be physical devices or chemical compositions that through their conversion when exposed to light can report on the “dose” received, frequently the number of einsteins per unit volume and per unit time.

In the case of chemical actinometers understanding the importance of the overlap between the emission spectrum of the light source and its overlap with the sample and actinometer composition is critical. In some special cases, this can be greatly simplified; for example, we developed an actinometer based on ruthenium-tris-bipyridyl ($Ru(bpy)_3^{2+}$) which is particularly useful for scientists researching $Ru(bpy)_3^{2+}$.[4] Thus, spectral matching between the sample and actinometer is not an issue. This may appear highly restrictive, yet the use of $Ru(bpy)_3^{2+}$ is so widespread that this unusual actinometer serves a large community. Chemical actinometers

require calibration against a physical device or a well-established chemical actinometer; among these, the ferrioxalate actinometer developed by Hatchard and Parker over 60 years ago is a frequent choice.[5]

The Norrish Type II reaction of valerophenone was studied 50 years ago by Wagner who determined quantum yields and product distributions under a variety of experimental conditions, Scheme 3.1.[3,6,7] In benzene, the quantum yield for acetophenone formation is 0.30. A minor product of the reaction is a mixture of cyclobutanols, which account for 18% of the products under the same conditions.[3]

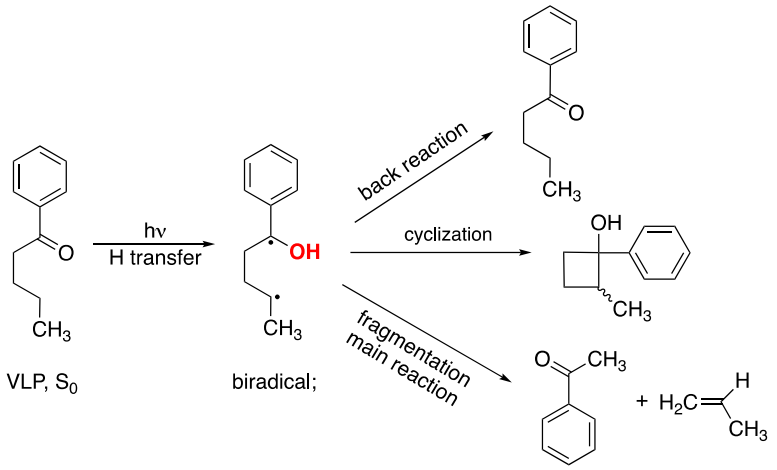

Scheme 3.1. Simplified mechanism for the Norrish Type II reaction of valerophenone. The full mechanism is available in Scheme S3.2 in the Supporting Information.

The Norrish Type II quantum yield is known to increase in hydrogen bonding solvents, as hydrogen bonding of the biradical reduces the probability of back hydrogen transfer. While many other aromatic ketones undergo the Norrish Type II reaction, one peculiarity of valerophenone is that the quantum yield is rather insensitive to the presence of oxygen,[8,9] a property that is very useful when using it as an actinometer.

A few other attempts to develop flow actinometers have been published.[10–13] In recent comprehensive reviews listing over a hundred photoreactions in flow, just one example includes irradiance measurements or chemical actinometry;[14,15] as a result, it is impossible to determine how efficient a photoreaction is. In our case, we aim at a system that is simple and that can be readily implemented in organic laboratories, as long as a UV-visible spectrometer is available.

In this study, we explore the use of valerophenone as an actinometer in flow systems, where it is normally difficult to measure quantum yields. In fact, valerophenone has been used before as an actinometer in batch systems.[3,16] Our system is not perfect and errors of 10% may be commonplace, particularly when Wagner's measurements must also incorporate some error;[3] however, this is a major improvement over the current status where simple actinometer tools are badly needed in the field of flow photochemistry.

3.2.3 Results and Discussion

A number of batch experiments were performed to verify solvent dependence and optimize analytical methods. These are included in the Supporting Information (Figures S3.4 – S3.6) and in general, they agree well with Wagner's classic studies on the Norrish Type II reaction.[7,16] We concentrate here on our flow studies.

3.2.3.1 Experimental design

Our actinometric studies concentrate on a specific geometry although the same principles could easily be applied to other light sources, flow design, and experimental geometries. In our case, we utilize as light source 8 W fluorescent tubes which are 30 cm long and with a diameter of 16 mm. Similar LED lamps (same geometry) are readily available for wavelengths of 365 nm and above. Figure 1 shows the experimental setup based on a single installed lamp on a Luzchem Expo panel with a capacity for five lamps; multiple lamps have been used successfully in some of our tests.

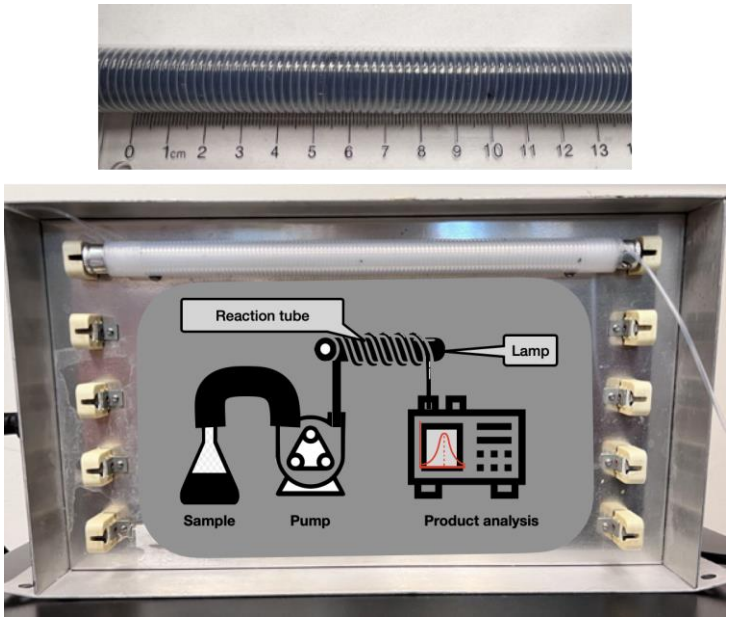

Figure 3.1. Expo panel with a single UVB lamp wrapped with Teflon tubing and within this device a diagram of the complete setup. The lamp is 30 cm long with an active part of about 26 cm; about 6.3 m of Teflon tubing with about 10 ml of solution are required to wrap each lamp. The upper part of the figure shows a segment of a UVA lamp wrapped with Teflon tubing; note that tight wrapping with no air gaps is essential.

The Teflon tubing used (see inset in Figure 3.1) has an outside diameter of 1.80 mm and an inside diameter of 1.50 mm corresponding to a wall thickness of 0.15 mm. Note that most Teflon tubing has thicker walls, however, the thin walls should be preferred as they add flexibility, minimize absorption and scattering by Teflon and facilitate the tight lamp wrapping required for the best photochemical performance. Typically, 6-7 m of tubing is needed to wrap each lamp.

Calculating the optical path for the geometry of Figure 3.1 is challenging and in our experience, a near-impossible exercise, as the optical path is different at the center or sides of the tube. A simple geometric calculation for a cylindrical shape gives an average optical path of 1.19 mm. However, the tubing (Teflon and sample) behaves as a cylindrical lens with different refractive index (Teflon vs. sample) and some light scattering in the Teflon walls. Thus, the value of 1.19 mm is a naive assumption based on perfect parallel beams that do not refract as they enter the cylindrical Teflon tube. Fortunately, we have found a simple way to determine experimentally a nominal optical path for the configuration of Figure 3.1. It is essential that the tube wrapping be very compact (as shown) with no spaces between vicinal tube turns.

3.2.3.2 Optical Path Determination

In order to estimate a nominal optical path, we used a spectroradiometer to measure the irradiance from the light source (UVB lamp used) under three conditions: (a) from the naked lamp, (b) from the lamp tightly wrapped with empty Teflon tubing and (c) from the lamp wrapped with Teflon tubing filled with a 0.1 M valerophenone solution in acetonitrile. The corresponding spectra are shown in Figure 3.2A; we note that similar spectra are usually available from lamp suppliers Remarkably, wrapping with Teflon tubing reduces the light intensity by only 22% and does not change the spectral distribution (Figure S3.7). Filling the tubing with 0.1 M valerophenone in acetonitrile causes a reduction of light of 85.5% at 310 nm with respect to the empty tube. Given that the extinction coefficient for valerophenone at 310 nm is 54.3 M^{-1} cm^{-1} (Figure 3.3), we can estimate the optical path as 1.54 mm (SI 3.3.8). This is not only a very useful number but also remarkable, as it is very close to the 1.5 mm internal diameter of the tubing. A more detailed analysis (Figure 3.2B) between 295 and 335 nm confirms a nominal optical path of 1.5 mm.

When one observes in detail the light measured at 290 nm for 0.1 M valerophenone, this is only 4.5% with respect to the empty tube, compared with ~15% at 310 nm. The difference is due to the absorption properties of valerophenone which shows a major increase below 300 nm, see Figure 3.3. The absorption change reflects the weak n,$\boldsymbol{\pi}$* transition at long wavelengths, compared with the allowed $\boldsymbol{\pi}$,$\boldsymbol{\pi}$* transition at shorter wavelengths.[17]

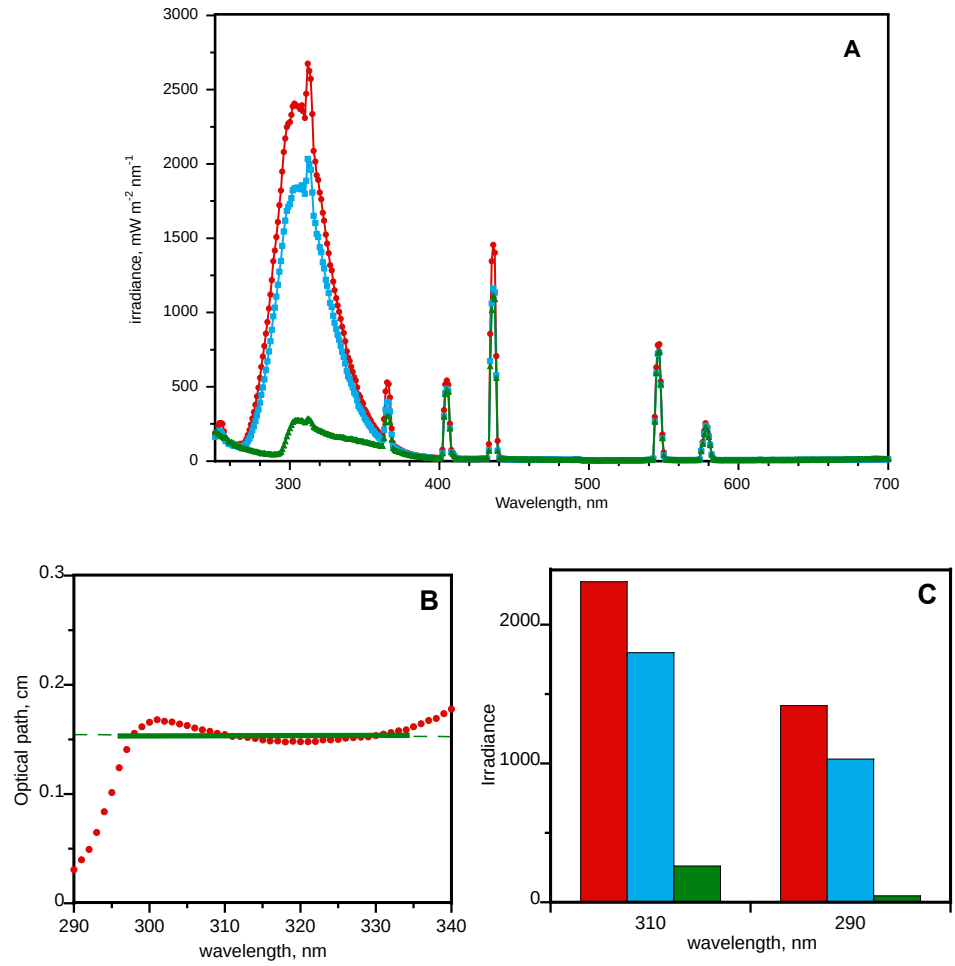

Figure 3.2. Panel A shows the spectra recorded for the UVB lamp in red; the blue spectrum is for the same lamp wrapped with empty Teflon tubing as shown in Figure 3.1, while in the green spectrum, the tubing has been filled with 0.1 M valerophenone in acetonitrile. Panel B shows the calculated optical path (see SI for details) based on the blue and green traces in panel A and knowing the extinction coefficient for valerophenone across the spectral range (Figure 3.3). Note that meaningful calculations can only be performed where the lamp has enough power ($280 \leq \lambda \leq 350$ nm) and where the sample in the tube does not block essentially all the light ($\lambda \leq$ 295 nm). The region with meaningful data is shown as a solid green line and yields an optical path of 1.5 mm. Panel C shows the irradiance measures at 290 and 310 nm (same colour code as Panel A). Note that at 290 nm the tube filled with valerophenone solution transmits essentially no light.

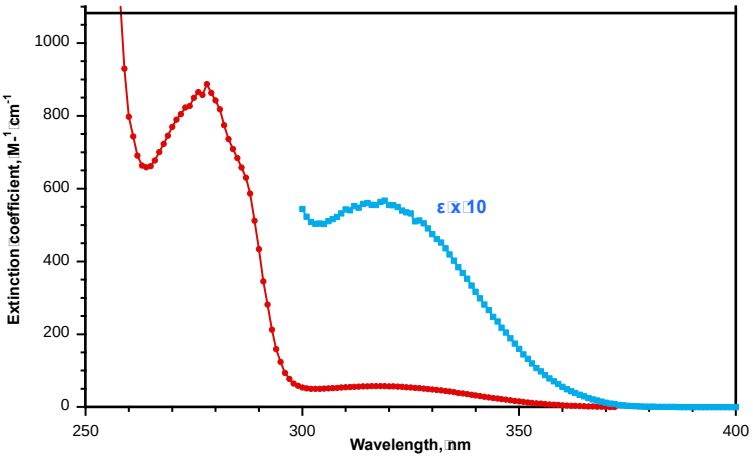

Figure 3.3. Extinction coefficient of valerophenone in acetonitrile. See SI for calibration plots for different valerophenone concentrations (Figure S3.8). The blue plot shows the same data as the red spectrum but multiplied x10 to facilitate visualization of the n,$\boldsymbol{\pi}^*$ transition.

3.2.3.3 Counting einsteins

Many actinometric applications involve competitive systems where the actual dose received by the sample is not actually calculated or required. In fact, the main output of actinometry is the einsteins received by a sample per unit volume and unit time, where an "einstein" corresponds to a mole of photons. In actinometry, the rate of loss of a product or formation of a product depends on quantum yield (**Φ**), incident light intensity (I_0) and a fraction of light absorbed by the compound (f).

$$\frac{d[All\ Product(s)]}{dt} = \frac{-d[Reagent]}{dt} = \Phi \times I_0 \times f \qquad (1)$$

Equation 1 is quite general and becomes very simple for systems where a single reagent gives a single product or where the sum of all products is used in the numerator. In the Norrish Type II reaction, this does not apply because the formation of cyclobutanols makes the consumption of reagents faster than the formation of acetophenone. Thus, in our case, we use the simplified form of equation 2 relying only on acetophenone.

$$\frac{d[Product]}{dt} = \Phi_{acetophenone} \times I_0 \times f \qquad (2)$$

Where I_0 x f corresponds to the light intensity or irradiance actually absorbed, or more correctly defined as absorbed photon flux density, I_a.[18]

$$I_a = I_0 \times f \quad (3)$$

Where, for simple systems, f can be readily calculated from the absorbance of the sample.

$$f = 1 - T = 1 - 10^{-A} \qquad (4)$$

Where A is the absorbance and T is the transmittance. Of course, things are somewhat more complicated when the sample is not contained in a simple cuvette with flat walls, but rather in a Teflon tube with scattering properties and formally a cylindrical lens. This makes the nominal optical path calculated above extremely useful.

While calculating I_0 can be challenging (vide infra) the determination of I_a is very simple, as it is exclusively based on the chemistry of the actinometer. For example, Figure 3.4 shows the formation of acetophenone in acetonitrile when a 0.1 M solution of valerophenone is irradiated with UVB light.

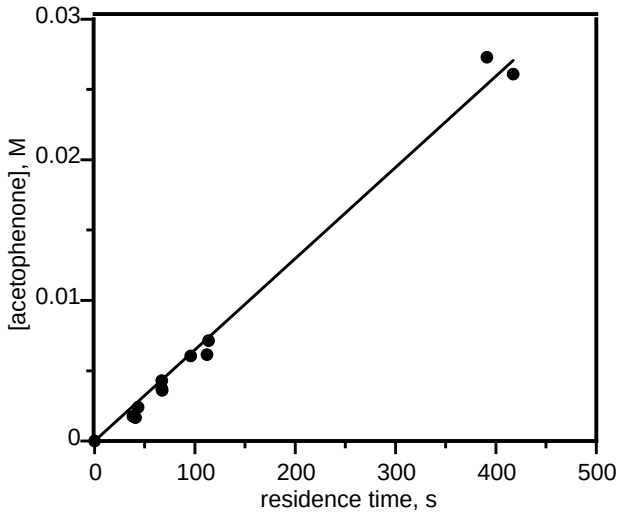

Figure 3.4. Formation of acetophenone during UVB photolysis of 0.1 M valerophenone in acetonitrile. The value of **Φ** acetophenone in acetonitrile has been determined as 0.60, See SI for batch data on this system (Figure S3.4). Correlation coefficients 0.997.

The graph of Figure 3.4 has a slope of 6.5 x 10^{-5} M s^{-1}, corresponding to the rate of acetophenone (ACP) formation. Since we know that the quantum yield for acetophenone formation in acetonitrile is 0.60, a simple calculation yields for the light absorbed by valerophenone, I_a = 1.1 x 10^{-4} einstein L^{-1} s^{-1}.

$$I_a = \frac{d_{ACP}/_{dt}}{\Phi_{ACP}} = \frac{6.5 \times 10^{-5}}{0.60}\ Ms^{-1} = 1.08 \times 10^{-4} einstein\ L^{-1}\ s^{-1} \qquad (5)$$

It is important to note that the calculation of I_a does not require any knowledge of the spectrum or irradiance of the light source, or the fraction of light absorbed.

Obtaining I_0 from I_a presents different levels of complexity depending on the characteristics of the light source, the properties of the solution and the geometry for irradiation. In an ideal case, the light source is perfectly monochromatic (as for lasers), the sample is contained in a spectrometer cuvette and the absorbance at the excitation wavelength (λ) is known (and preferably is high). Under these simple spectroscopic conditions, we have,

$$I_0 = \frac{I_a}{(1 - T_\lambda)} \qquad (6)$$

Unfortunately, the situation just described is rarely encountered in the organic laboratory, particularly if flow studies are involved. The system of Figure 3.1 is complex and thus an experimentally determined optical path is useful, but not enough to convert I_a into I_0. For polychromatic light sources, the conversion from I_a to I_0 is dependent on the overlap of the emission from the light source and the absorption spectrum of the actinometer and/or sample. This is illustrated for the UVB lamps used in this work and a solution on valerophenone in acetonitrile, Figure 3.5. Thus at λ<300 nm valerophenone will absorb ≥ 90% of the incident light, but this is not true at longer wavelengths where a significant fraction of the light will not be absorbed. For each wavelength in the emission spectrum of the lamp, one can calculate the number of photons (or einstein) absorbed, I_a^{λ}, or the fraction of photons absorbed, f_a^{λ}.

$$f_a^{\lambda} = 1 - T_\lambda \qquad (7)$$

In most modern instruments it is easy to export a spectrum at 1.0 nm intervals and it is thus simple to either integrate or sum the incident light at each wavelength (I_λ) and the light absorbed. That is:

$$I_0 = \sum_{\lambda} I_\lambda \qquad (8)$$

$$I_a = \sum_{\lambda} I_\lambda \times (1 - T_\lambda) \qquad (9)$$

The fraction of light absorbed across the spectral region examined (f_λ^{all}) is:

$$f_\lambda^{all} = \frac{I_a}{I_0} = \frac{\sum_\lambda I_\lambda \times (1 - T_\lambda)}{\sum_\lambda I_\lambda} \quad (10)$$

Fortunately, these equations convert to a simple graphic approach (Figure 3.5B) that does not require the absolute value of irradiance from the source at each wavelength, but rather simply the spectral light distribution. To emphasize this we use normalized lamp spectra in our calculations.

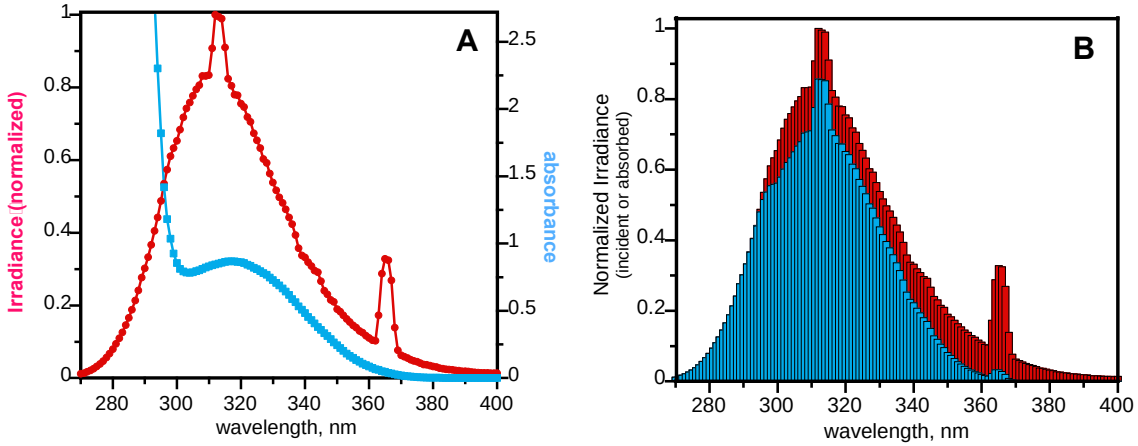

Figure 3.5. Panel A (right axis) shows the absorbance of a 0.1 M solution of valerophenone in acetonitrile contained in a system (Teflon tubing) with an effective optical path of 1.5 mm, while the left axis shows the normalized spectral distribution of the UVB lam used. Panel B shows the spectral distribution of the UVB lamp (normalized, red) and the fraction of light absorbed by the valerophenone solution. (blue). No red curve is seen below ~300 nm because the light is quantitatively absorbed by valerophenone.

In the case of Figure 3.5, the value of f_λ^{all} is 0.771, or 77.1% of the photons would be absorbed by the valerophenone solution. While for valerophenone the absorption spectrum is required for the sample used, for the light source spectrum, only the intensity distribution is required but not the actual irradiance under the conditions of the experiment. In order to emphasize this, the lamp spectrum has been normalized before the detailed calculation. This is important as many organic laboratories do not have a spectroradiometer on hand; this is not required, as the spectral distribution of the light source is usually available from the suppliers and

readily accessible. As illustrated in the SI, the Teflon tubing affects the power, but not the spectral distribution of the lamp.

If we now return to the data in Figure 3.4 we determined above that $I_a = 1.08 \times 10^{-4}$ einstein L^{-1} s^{-1}, which given that 77.1 % of the light was absorbed leads to $I_0 = 1.4 \times 10^{-4}$ einstein L^{-1} s^{-1} for the incident light between 270 and 400 nm. Thus the valerophenone actinometer can yield both the values of I_a and I_0 based on a product analysis, the spectrum of the actinometer solution and the relative spectral distribution for the light source.

When performing actinometry it is preferable to work at a relatively low conversion.[19] This is important as overlap graphs, such as Figure 3.5, are based on initial conditions. The sample spectrum will likely change as the reaction progresses and in some cases, products may compete for the incident photons. The case of valerophenone is rather forgiving as the acetophenone produced can absorb photons where the energy can then be transferred to valerophenone,[20] thus allowing higher conversions to be used. This may not be true for other materials under study, where low conversions should be preferred.

3.2.3.4 Examples of applied actinometry

Actinometry requires that the absorbance of the actinometer solution and that of the sample be matched, or that the differences are such that a quantitative correction can be readily introduced. This is relatively simple with monochromatic light sources, but somewhat more difficult with lamps that are intrinsically polychromatic. There is one situation when these restrictions can be easily overcome, and that is when the sample and actinometer absorb all or most of the incident light. In this work, we use UVA and UVB lamps, and in the case of organic photochemistry, high light absorption is more easily achieved with UVB lamps (red spectrum in Figure 3.5A). Our work does not rely on complete light absorption but rather quantifies the overlap between lamp emission and absorbance by both, actinometer and sample. Both must have some spectral overlap (not the same) with the light source used.

It should be noted that while narrowband LEDs are readily available for the visible and NIR spectral regions, the same is not true for ultraviolet light where LEDs around 365 nm with good power output are commercially available, the same is not true for shorter wavelengths.

3.2.3.4.1 Valerophenone *vs*. quenched valerophenone

This example is specifically introduced to show a case of low absorbance at the UVA lamp wavelength and poor sample absorbance matching with the lamp spectrum (see inset in Figure 3.6 and Figure S3.11). This case is made simple (and quite accurate) by the perfect matching of sample and actinometer, something that is true because the sample is also valerophenone and the quencher, naphthalene, does not absorb significantly in the spectral region of interest at the concentrations used.

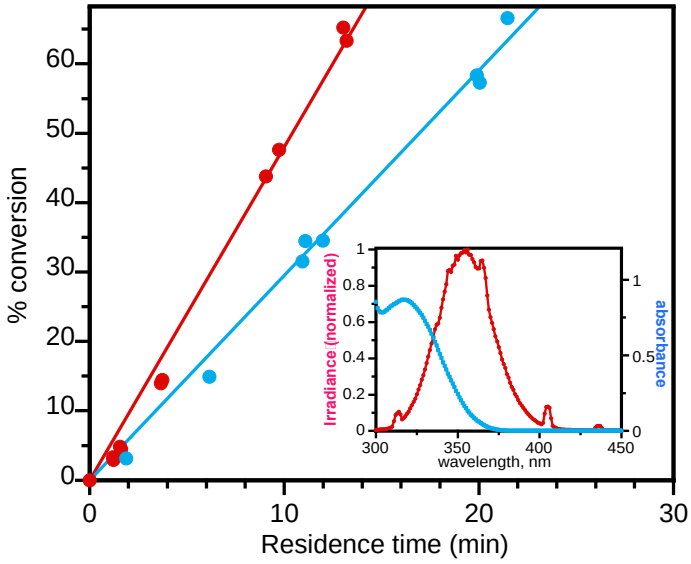

Figure 3.6. Conversion as a function of residence time for 0.1 M valerophenone in acetonitrile (red) and the same composition containing 0.01 M naphthalene (blue). The emission shows the spectrum of the UVA lamp (irradiance normalized, left axis, red), and the absorbance spectrum of the valerophenone solution for a 1.5 mm optical path (right axis, blue). Correlation coefficients 0.998 (red) and 0.997 (blue).

The results are shown in Figure 3.6, where 0.01 M naphthalene reduces the rate of conversion slope from 4.80 to 2.95 min^{-1}, that is quenching just under 50% of the valerophenone triplets. In this case, the valerophenone concentration is the same with and without the quencher, and the spectral matching between the actinometer and sample is perfect, equation 11, which also includes the numeric data for the system of Figure 3.6.

$$\Phi_{\mathrm{sq}} = \Phi_{\mathrm{Act}} \frac{Slope_{sq}}{Slope_{Act}} = 0.60 \frac{2.95}{4.80} \sim 0.37 \qquad (11)$$

Where the subscripts 'Act' and 'sq' refer to the actinometer solution and the sample containing the quencher, respectively. In this case, an analysis such as shown in Figure 3.5B is unnecessary. Note that in this case a UVA lamp is preferred, as naphthalene is transparent in this region, but partially absorbing in the UVB region.

3.2.3.4.2 Benzoin photochemistry

α-Phenylbenzoin (benzoin) undergoes Norrish Type I reaction involving C-C bond cleavage,[21,22] scheme 3.2.

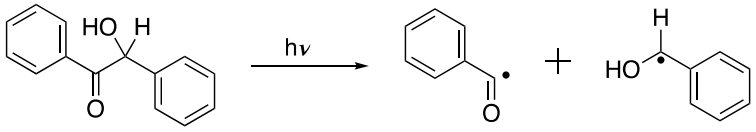

Scheme 3.2. Simplified mechanism for the Norrish Type I reaction of benzoin

From the actinometry perspective, the fate of the radicals is not important in the context of this contribution, as the photochemistry is complete once the radicals have been formed; suffice to say that benzaldehyde is a common product.

We studied the photolysis of benzoin in acetonitrile under nitrogen and using the same UVB light source as in Figure 3.2. This led to the graphs of Figure 3.7, where valerophenone (0.1 M and adjusted for a 1.5 mm optical path) absorbs 77.8% of the incident light, while benzoin (0.02 M) absorbs 77.1 %, based on the same analysis as in Figure 3.5. The integration was performed from 270 to 400 nm.

In the actual actinometric experiment, the conversion of the sample and actinometer was determined as a function of the residence time in the Teflon tubing (6.3 m wrapping over the 26 cm where active emission of the lamp takes place), Figure 3.7.

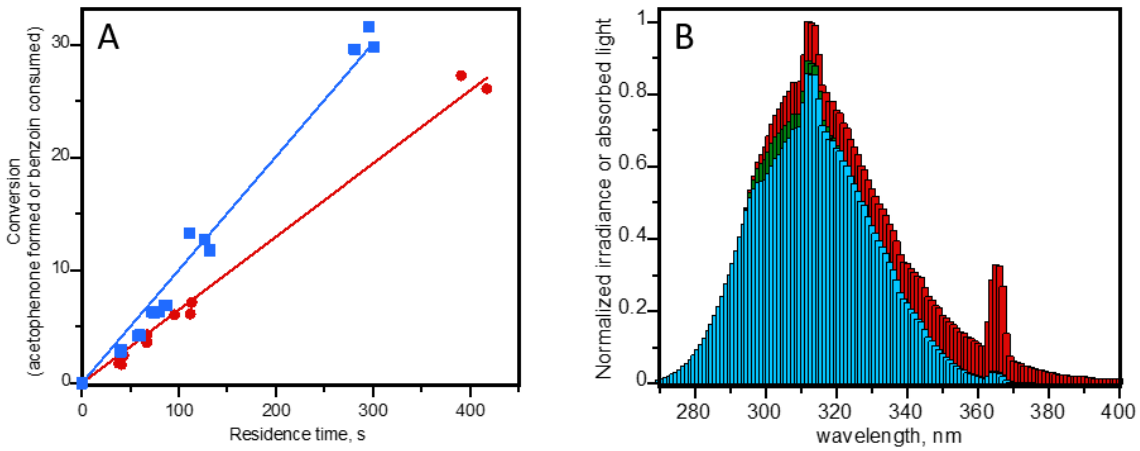

Figure 3.7. (A) Acetophenone formation from valerophenone 0.1 M in acetonitrile (red circles) and benzoin 0.02 M conversion in acetonitrile (blue squares). Both experiments are done in a flow system with 6.3 m Teflon tubing around a UVB lamp. Correlation coefficients 0.998 (red) and 0.994 (blue). (B) Spectral distribution of the UVB lamp (normalized, red), the fraction of light absorbed by the valerophenone acetonitrile solution (0.1 M, blue) and the fraction of light absorbed by benzoin (0.02 M, green). Calculations based on a 1.5 mm optical path.

In Figure 3.7A the valerophenone actinometer and benzoin give a reasonably linear plot even at conversions around 25%. The slopes obtained are 0.0649 s^{-1} for acetophenone and 0.100 s^{-1} for benzoin. As a general rule, product measurements (as for acetophenone) yield less error than consumption measurements (e.g., benzoin), particularly at very low conversions.

In principle, the ratio of the two slopes, multiplied by the actinometer quantum yield ($\mathbf{\Phi}_{Act}$) gives the quantum yield for the sample, $\mathbf{\Phi}_{sm}$. However, two corrections are needed, one to account for the different concentrations of sample and actinometer (C_{sm} and C_{Act}), as the plot of Figure 3.8 is based on conversions, and second, the sample and actinometer may absorb a different fraction of the lamp light, see Figure 3.7. This leads to equation 13.

$$\Phi_{sm} = \Phi_{Act} \frac{Slope_{sm}}{Slope_{Act}} \times \frac{C_{sm}}{C_{Act}} \times \frac{f_{\lambda}^{Act}}{f_{\lambda}^{sm}} \quad (13)$$

Which in numeric form for the system of Figures 7 and 8 converts to:

$$\Phi_{sm} = 0.60 \frac{0.100}{0.0649} \times \frac{0.02}{0.1} \times \frac{77.8}{77.1} = 0.19$$

Where the values of f^{Act}_{λ} and f^{sm}_{λ} derived from Figure 3.7 are 0.778 and 0.771, respectively, for an integration range of 270 to 400 nm.

Equation 13 provides a general expression for quantum yields based on the consumption of a reagent (sm) or the production of a product. When all relevant numbers are entered for the system of Figure 3.7, the quantum yield is $\mathbf{\Phi}_{sm} = 0.19$. For comparison, reported values are 0.33 based on transient studies[21] and 0.41 in benzene based on product studies.[22] We were surprised by our low value in acetonitrile and decided to repeat the complete study in benzene, where the simple approach used by Lewis and co-workers appears quite robust.[22] These studies are very similar to those just presented for acetonitrile and are described in detail in the SI and yield a quantum yield of 0.43 in complete agreement with the reported value in benzene (figure S3.9 and equation S3.4). This makes us confident that the actinometer presented here is reliable. Further, we believe that the value of 0.19 in acetonitrile is correct. It should be noted that in benzene the integration was performed between 280 and 400 nm, that the start (280 nm) is 10 nm longer than in all other UVB studies in this work. This reflects that the high absorption of benzene below 280 nm would shield absorption by benzoin in this range. While a double correction is possible using the same strategy as in Figure 3.7, it is not justified in this case given the small range of sample-solvent overlap.

3.2.3.4.3 Studies of Irgacure-2959

Irgacure-2959 (I2959) is a commercial benzoin sold as a photoinitiator. Our interest in I2959 relates to its high efficiency in producing strongly reducing ketyl radicals that can be used in the reductive synthesis of metal nanoparticles.[23,24] The mechanism of photodecomposition[25] is shown in Scheme 3.3.

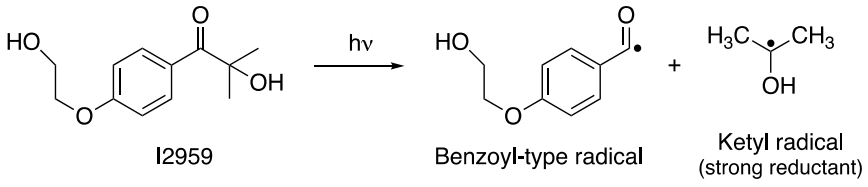

Scheme 3.3. Photodecomposition of I2959 under UV irradiation.

As in the case of benzoin above, the fate of the radicals is not critical although it usually depends on other substrates present, with the ketyl radical usually seeking an electron acceptor and the benzoyl-type radical ultimately leading to the benzoic acid derivative if oxygen is present. In any event, conversion was measured based on the consumption of I2959 and compared with acetophenone produced from valerophenone. These results are shown in Figure 3.8A, where in the case of I2959 we include three sets of data run on three different days; the slopes are 0.149 s^{-1} and 0.138 s^{-1} for all data and low conversion data, respectively. From this, we adopt a value of 0.14 s^{-1}, which should be compared with the value of 0.065 s^{-1} for valerophenone.

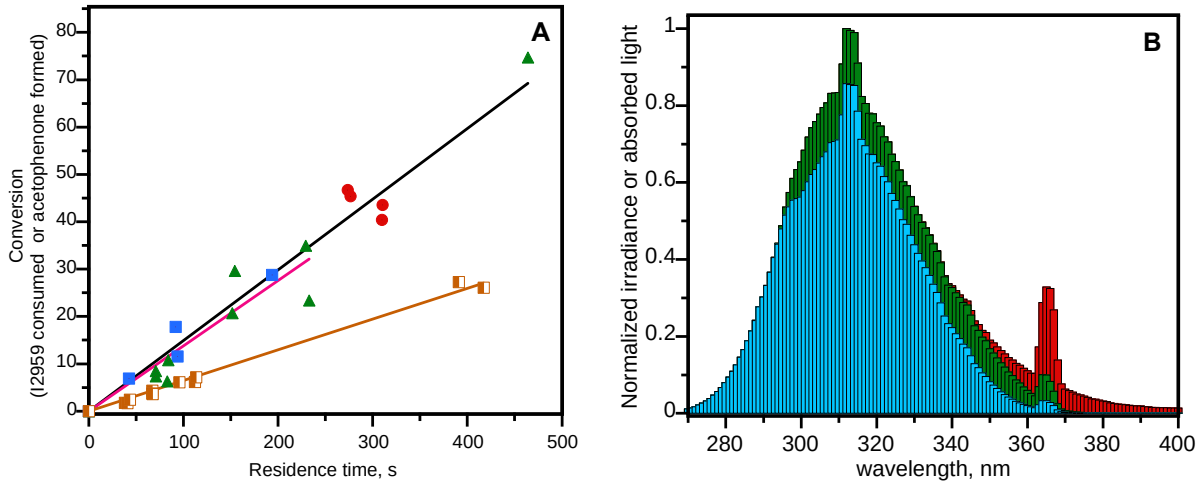

Figure 3.8. (A) Acetophenone formation from valerophenone 0.1 M in acetonitrile (red/white squares) and three experiments showing I2959 0.1 M conversion in acetonitrile (blue squares, green triangles and red circles). Both experiments are done in a flow system with 6.3 m Teflon tubing around a UVB lamp and containing about 10.2 ml of irradiated sample; Correlation coefficients 0.936 (red, low conversion data), 0.976 (all data, black line) and 0.997 (valerophenone). (B) Spectral distribution of the UVB lamp (normalized, red), the fraction of light absorbed by the valerophenone acetonitrile solution (0.1 M, blue) and the fraction of light absorbed by I2959 (0.1 M, green). Calculations based on a 1.5 mm optical path.

Given slopes in Figure 3.8A of 0.065 and 0.14 s^{-1}, for acetophenone formation and I2959 consumption, respectively. Figure 3.8B leads to 77.1% light absorbed by valerophenone and 93.5% by I2929 based on the integration between 270 and 400 nm.

Which in numeric form for the system of Figure 3.8 and using equation 7 converts to:

$$\Phi_{sm} = 0.60 \frac{0.14}{0.065} \times \frac{0.1}{0.1} \times \frac{77.1}{93.5} = 1.06$$

This suggests a quantum yield of 1 within experimental error and is consistent with the short lifetime of the I2959 triplet[25] and the high efficiency of this initiator.

3.2.3.5 Experimental

All chemicals and solvents were purchased from Sigma-Aldrich and used as received. The light source was an EXPO panel from Luzchem fitted with lamps from the same supplier. The Teflon tubing has an outside diameter of 1.80 mm and an inside diameter of 1.50 mm corresponding to a wall thickness of 0.15 mm. It is important that the experimental optical path of 1.5 mm was quite reproducible for various lamp wrappings and different batches of the same product, but it may have to be re-measured if different types of tubbing are used.

Various peristaltic pumps were used in this work, with a flow rate ranging from ~1.5 to 200 mL/min. Product studies were performed by GC-MS.

3.2.4 Conclusions

The valerophenone flow actinometer developed in this work provides for the first time a convenient tool to perform quantitative flow photochemistry studies. The widespread use of flow photochemistry[14] requires tools that allow the key reagent in the system, light, to be quantitatively measured, and thus, not just measure product yields, but also quantum yields. This will make results from different laboratories comparable, otherwise “better yields” may simply mask different illumination conditions.

The valerophenone actinometer does not require spectro-radiometric measurements and only the shape of the lamp emission is required, something that is normally available from the supplier. The normalized lamp emission spectrum is combined with the absorption spectra of the sample and actinometer to determine the fraction of light absorbed by each one. We believe that this work finally enables organic chemists doing flow photochemistry to determine and report “light”, both incident and absorbed, using standard irradiance measurements.

3.3 Post-print version of supplementary information

3.3.1 Materials and Instruments

Most of the compounds for doing experiments such as valerophenone, acetophenone, and benzoin, were purchased from Sigma Aldrich and Irgacure 2959 was from BSAF. The solvents were from Fisher Chemical. UVA and UVB lamps (8W), and Expo panel (EXPO-01) were from Luzchem Research, Inc. Teflon tubing (STT-15) was purchased from Component supply company and the pump (minipuls 3) was from Gilson.

All samples were analysed by GC-MS analyses from Agilent 6890-N Gas Chromatograph with an Agilent 5973 mass selective detector. For the UV-Vis spectrum, Cary 60 UV-Vis spectrophotometer from Agilent was used.

3.3.2 UVA and UVB lamp spectra

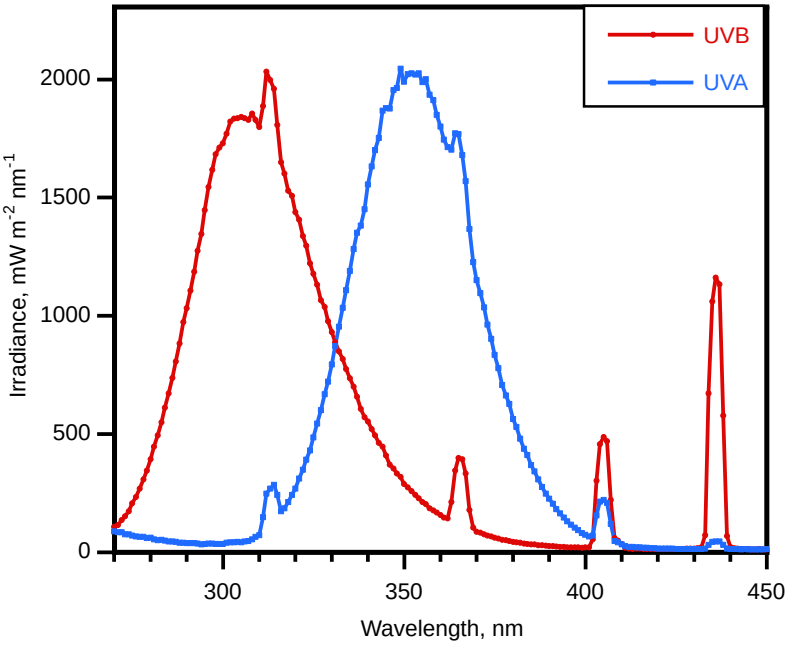

Figure S 3.1. Spectra recorded for the lamps used. The spectra were recorded with the Teflon tubing installed and the spectroradiometer detector head in close proximity to the tubing surface.

3.3.3 Detailed mechanism for the Norrish Type II reaction of Valerophenone

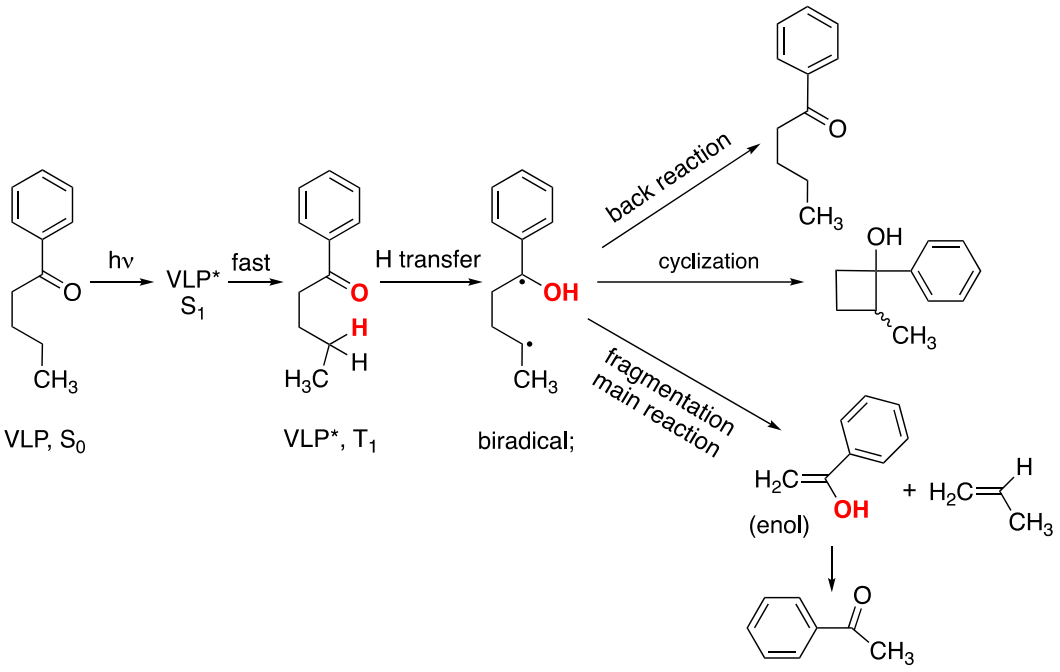

Figure S 3.2. Detailed mechanism for the photodecomposition of valerophenone. Important details (compare with Scheme 3.1) are the explicit involvement of a short-lived triplet state and the fact that the product acetophenone is initially produced in its enol form.

3.3.4 Flow experiments

First, the lamp was turned on for around 10 min to make sure that the intensity of the lamp was stable. In the second step, the solution of reactants was pumped over the Teflon tubing with a single pass. For every flow rate, 2 to 3 samples were collected periodically at the exit of the tubing after pumping at least 2 times more volume than a tubing capacity. The flow rate was calculated accurately by using the weight of collected samples and converting them to the volume by using the density of the solvent. The residence time is obtained by dividing the volume of the tubing around the lamp by the flow rate. Then samples were analyzed by GC-MS to have precise data for the compounds analyzed.

3.3.5 GC-MS analysis

All the samples from batch and flow experiments were analyzed with GC-MS. For example, 20 µL of valerophenone 0.1 M, diluted with 1 ml CH_2Cl_2 contained 0.064 mM tert-butylbenzene as a standard Figure S3.3.

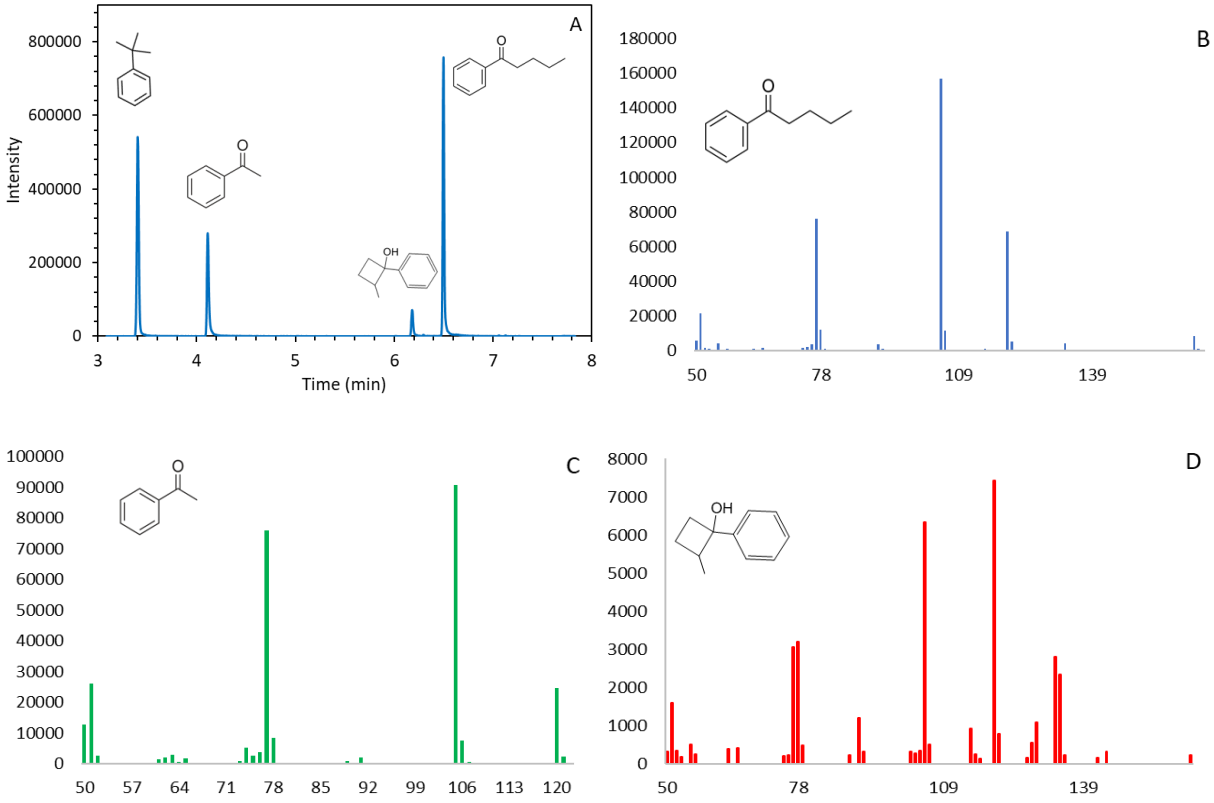

Figure S 3.3. GC-MS analysis. (A) Gas Chromatography peaks related to a sample with 62.3% valerophenone, 30.37% acetophenone, and 7.33% 2-methyl-1-phenyl-1-cyclobutanole. (B) Mass spectrum of valerophenone, (C) acetophenone, and (D) 2-methyl-1-phenyl-1-cyclobutanols. The two isomeric cyclobutanols are not separated in this column.

3.3.6 Batch experiments performed in preliminary work

To optimize the reaction conditions, a few preliminary batch experiments were done in different solvents and concentrations. Experiments were performed in quartz tubes that were located parallel in touch with an 8 w lamp (UVA or UVB). Samples were taken continuously and analyzed by GC-MS.

Valerophenone 0.1 M in 10 ml acetonitrile or benzene was irradiated with a UVA lamp at room temperature to understand the effect of different solvents on the reaction rate Fig S3.4. Rate of the valerophenone consumption or acetophenone formation in acetonitrile is around 2 times faster than the same reaction in benzene.

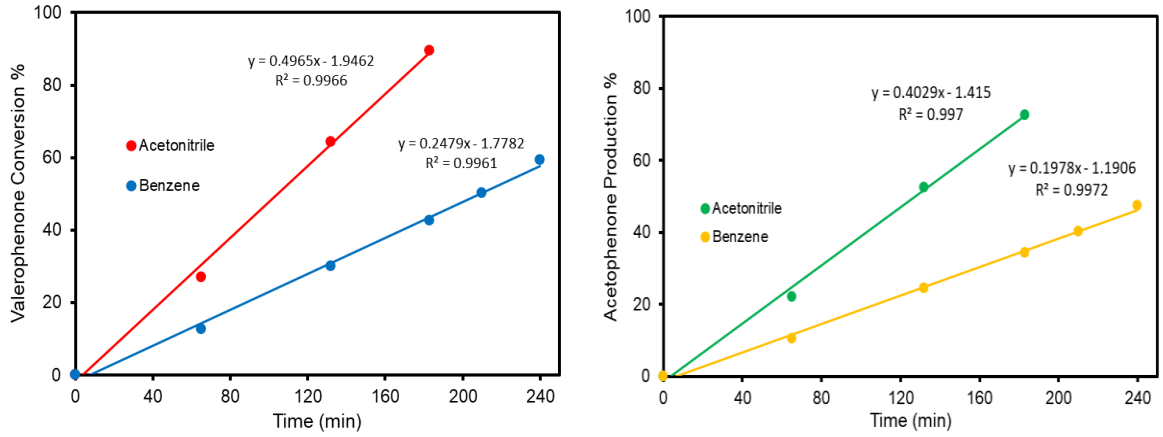

Figure S 3.4. The batch experiment of valerophenone 0.1M in acetonitrile and benzene 10 ml, irradiated with a UV-A lamp. (A, left) is the valerophenone consumption and (B, right) is the acetophenone formation rate.

Note that the rate of valerophenone consumption is higher than that of acetophenone formation. This is expected as the former includes the formation of cyclobutanol products, see Figure S3.2. Given the reported quantum yield of 0.3 for acetophenone in benzene, the value in acetonitrile is 0.6.

The effect of a quencher on the quantum yield was studied by running the same batch experiment of valerophenone 0.1M in acetonitrile 10 ml irradiated with UVA. This time naphthalene 0.01 M was added to the solution Figure S3.5.

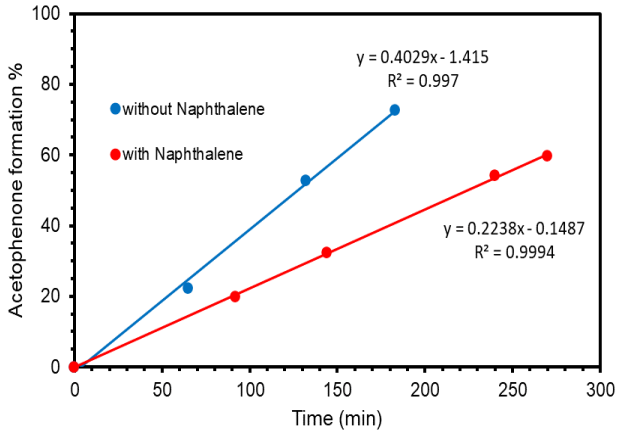

Figure S 3.5. The batch experiment of valerophenone 0.1M in acetonitrile 10 ml with naphthalene 0.01 M, irradiated with a UVA lamp.

Appropriate concentration for doing experiments with every compound was selected by considering the lamp spectrum and absorption spectrum of the actinometric system. The concentration should be high enough to absorb the most incident light and low enough to run fast in our flow setup. For example, 10 ml of valerophenone 0.1 M and 0.3 M in acetonitrile were irradiated with a UVB lamp in two quartz test tubes at the same time. The results of GC analysis for batch experiments (Figure S3.6) and UV-Vis spectrum showed that 0.1 M is a convenient concentration for valerophenone to follow the actinometric reactions.

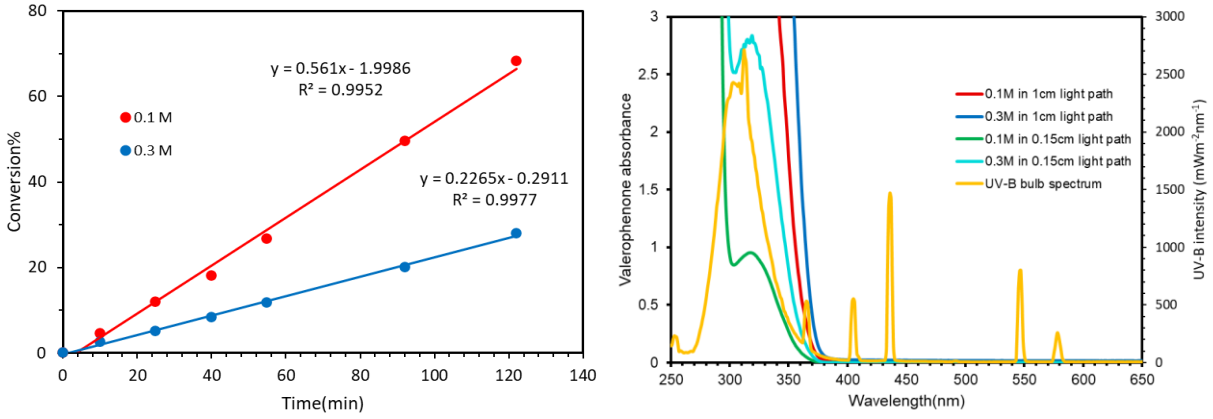

Figure S 3.6. (A) Batch experiments of 10 ml valerophenone 0.1 M and 0.3 M in acetonitrile with a UVB lamp. (B) Absorbance spectrum of valerophenone with different concentrations in acetonitrile (left axis) and UVB lamp emission spectrum (right axis).

3.3.7 Effect of Teflon tubing on the spectral shape

The actinometer developed here requires knowledge of the spectral distribution of the light source used, but not the actual irradiance values. We show here actual irradiance values simply to familiarize the reader with typical irradiance values (frequently referred to as "intensity"). This means that users of this actinometer do not need to have a spectroradiometer on hand as lamp spectral distributions are normally available from the lamp supplier.

It is important that the Teflon tubing should not alter significantly the lamp spectrum, although irradiance changes are of course expected when Teflon tubing surrounds the lamp. The spectra below show that Teflon tubing has no significant effect on the spectral distribution of the lamp. This observation legitimizes the use of reported lamp spectra, with no need for this to be remeasured locally.

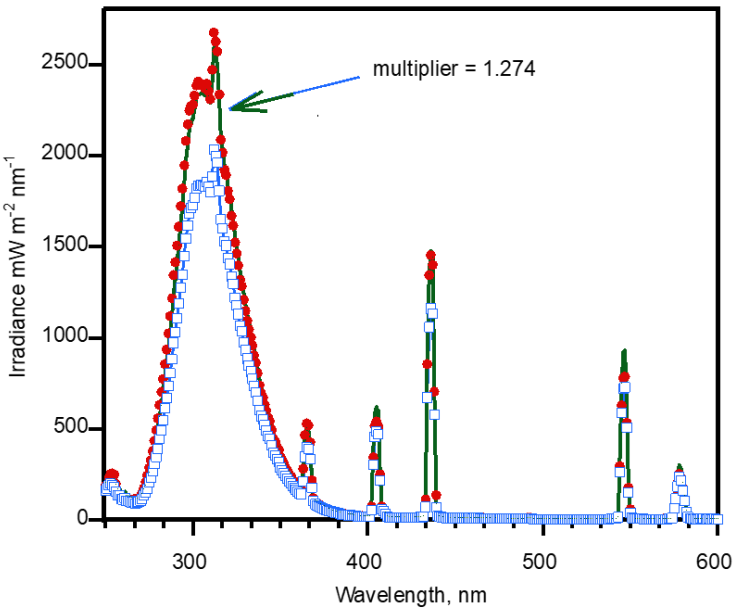

Figure S 3.7. Based on Figure 2 in the main article, shows (red dots) the spectrum of the naked UVB lamp and in blue the spectrum recorded for a lamp with Teflon tubing installed, as shown in Figure 1. The green line corresponds to the blue spectrum multiplied by 1.274; this value is the ratio of the integrals under the curves for the naked lamp and the one coated with Teflon tubing. Integration was performed between 250 and 600 nm.

3.3.8 Optical path calculation

The flow setup was prepared by the tight wrapping of Teflon tubing (OD = 1.8 mm and ID = 1.5 mm) around a lamp. The amount of light was measured by using a spectroradiometer. The light intensity of the lamp was measured in three different conditions, (a) the naked lamp, (b) the lamp tightly wrapped with empty Teflon tubing and (c) the lamp wrapped with Teflon tubing filled with a 0.1 M valerophenone solution in acetonitrile. In all three measurements lamp was on for 10 minutes before recording the spectrum to make sure that the intensity is stable and the slit of the spectroradiometer was in touch with the lamp.

Comparing the results of (b) and (c) as mentioned in the manuscript, Figure 3.2A, showed that 85.5% of light at 310 nm is reduced when we pumped the valerophenone 0.1 M inside the empty Teflon tubing. This means that only 14.5 % of light is transmitted at 310 nm. The absorbance (A) of a solution has a logarithmic relation with a transmittance (T) (equation S1).

$$A = -log_{10} T = -\log 14.5 \quad A = 0.839 \qquad \text{(S1)}$$

According to the Beer-Lambert law absorbance has a linear relationship with the concentration (c), molar absorption coefficient ($\boldsymbol{\varepsilon}$), and optical path (b) (equation S2).

$$A = \varepsilon bc \qquad \text{(S2)}$$

To find an optical path in our flow setup, we need to determine the molar absorption coefficient by using the calibration curve of the valerophenone at 310 nm Figure S3.8.

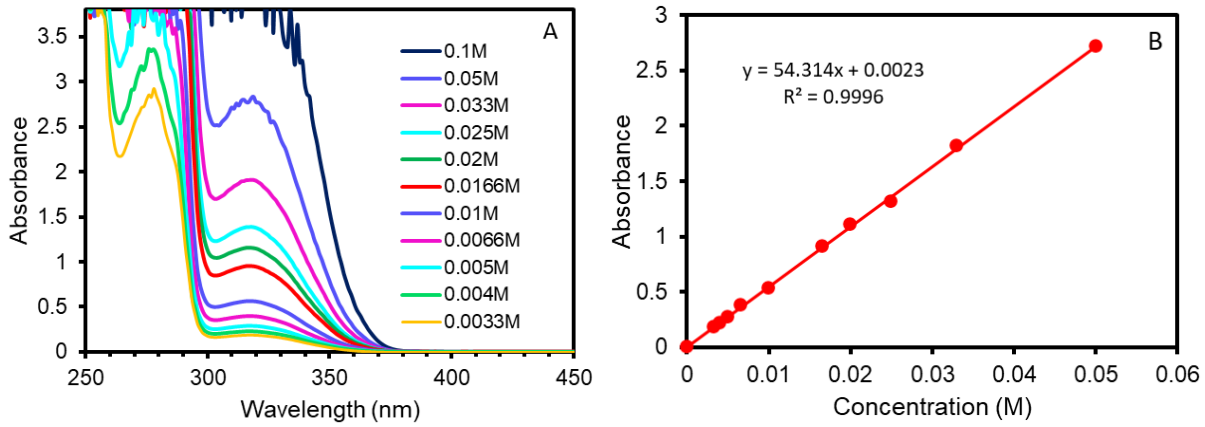

Figure S 3.8. (A) UV-Vis spectrum of valerophenone in acetonitrile was done in a Cary 60 spectrophotometer. (B) Calibration curve of valerophenone at 310 nm. These data were used to determine the extinction coefficient for valerophenone.

The calibration curve at 310 nm gives a molar absorption coefficient of 54.3 $M^{-1}cm^{-1}$. Now optical path can be calculated by the Beer-Lambert equation (S3).

$$b = \frac{A}{\varepsilon c} = \frac{0.838}{54.3 \times 0.1} = 0.154\ cm \cong 1.5\ mm \qquad (S3)$$

3.3.9 Benzoin photodecomposition in benzene

In another attempt, the whole actinometric process was repeated in benzene to compare this research results with the literature.[3] For this aim, the acetophenone formation from valerophenone 0.1 M in benzene by a UVB lamp flow setup was studied and compared with the conversion of benzoin 0.02 M in benzene Figure S3.9.

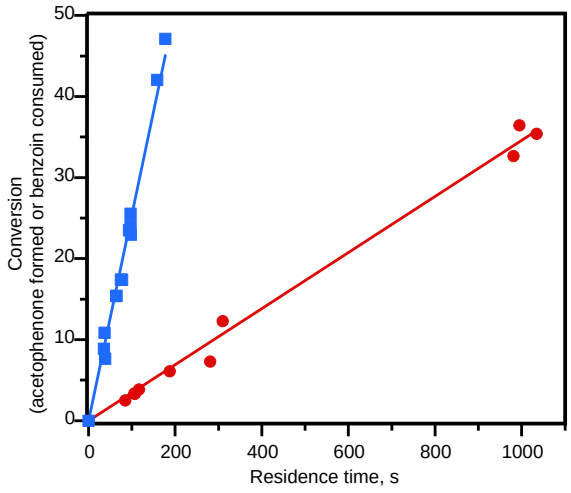

Figure S 3.9. Acetophenone formation from valerophenone 0.1 M in benzene (red circles) and benzoin 0.02 M conversion in benzene (blue squares). Both experiments were done in a flow system with 6.3 m Teflon tubing around a UVB lamp and samples were analyzed with GC-MS.

The rate of conversion was 0.0346 s^{-1} for acetophenone and 0.254 s^{-1} for benzoin. The spectral overlap is shown in Figure S3.10. In this case, the integration starts at 280 nm, as benzene has extensive absorption below this wavelength.

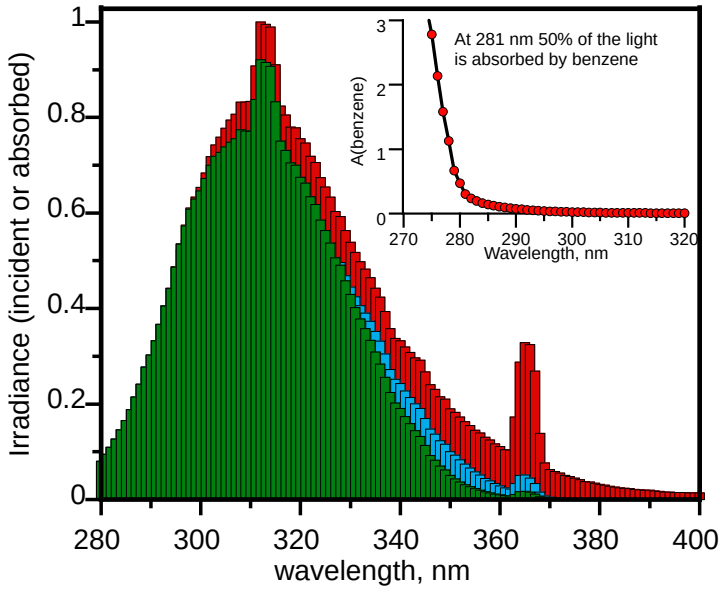

Figure S 3.10. Overlay of the spectrum of the UVB lamp (red) with the spectra of valerophenone (blue) 0.1 M and of benzoin (green) 0.02 M, all calculated for a 1.5 mm optical path. The inset shows the spectrum of pure benzene in a 1 cm cuvette.

From Figure S3.10, the fraction of UVB light absorbed is 77.4% for valerophenone and 78.6% for benzoin. Since the quantum yield of acetophenone formation in benzene is 0.3 according to the Wagner report.[3] Then the quantum yield of benzoin in benzene can be calculated as equation (S5).

$$\Phi_{\text{sm}} = \Phi_{\text{Act}} \frac{Slope_{sm}}{Slope_{Act}} \times \frac{C_{sm}}{C_{Act}} \times \frac{f_{\lambda}^{Act}}{f_{\lambda}^{sm}} \qquad \text{(S4)}$$

$$\Phi_{\text{sm}} = 0.30 \frac{0.254}{0.0346} \times \frac{0.02}{0.1} \times \frac{77.4}{78.6} = 0.43 \qquad \text{(S5)}$$

The obtained quantum yield is 0.43, in agreement with the reported data of Lewis and co-workers.[22]

Limited absorption for valerophenone in the UVA regionThe inset spectrum in Figure 3.6 shows the spectrum of valerophenone compared with that of the UVA lamp used. The overlap is adequate, but limited compared to the UVB lamp used in other experiments. Figure S3.11 shows this overlap in the same format used throughout this paper, leading to 34.7% light absorption by

valerophenone 0.1 M corrected for a 1.5 mm optical path and integrated between 300 and 420 nm.

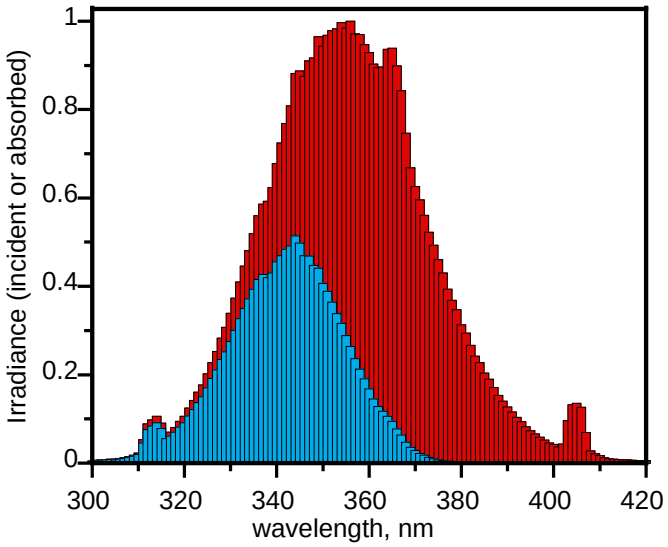

Figure S 3.11. Normalized UVA emission spectrum (red) and a fraction of the light absorbed by 0.1 M valerophenone in acetonitrile (blue).

3.3.10 Detailed procedure for overlap calculations

Figure S3.11 is used as an example to explain the detailed procedure to determine the fraction of light absorbed by a given sample or actinometer solution. The procedure is the same for both. To start, the spectrum of the light source is needed, in this case, lamps supplied by Luzchem, a standard 8 W UVA lamp. The spectra determined with a spectroradiometer or by the supplier will resemble the one shown in Figure S3.1 for a UVA lamp. Notice that the units are typically either mW m^{-2} nm^{-1} or W m^{-2} nm^{-1}. We could use these units directly, but in reality, we only need the spectrum shape, not the absolute values, and normalization is convenient. This simply requires finding the value at the maximum and dividing the spectral data by that number, so that the maximum now has an amplitude of 1.0. In our example, the maximum is at 365 nm, a typical line in the mercury spectrum.

It is convenient to have spectral data for every nanometer (x-axis). Emission data can be determined with a spectroradiometer or from the lamp supplier (in the case of Luzchem:

https://www.luzchem.com/ExposureStandards.php). If only graphic data is available, either digitize it or more easily request the digital data from the supplier.

If data are not at exactly integer wavelength values you can either apply the nearest integer function (NINT) or use the integer function (INT) on "value + 0.5", to generate a convenient wavelength array. Once you have these data, you do not need to redo this for every experiment, as the spectral shape does not change.

For the liquid actinometer or sample solution, you need the absorbance spectrum for the actual solution to be used in the experiment. Most likely, you will be using a 1 cm cuvette. You need to convert the absorbance to the actual optical path of your flow system; if you use the same Teflon tubing as in this report, the experimentally determined optical path is 0.15 cm. Simply multiply your spectral data by 0.15. Many spectrometers do not provide the data at integer wavelength values. You can conveniently use the same procedure described above, that is: apply the nearest integer function (NINT) or use the integer function (INT) on "value + 0.5", to generate a convenient wavelength array. At least one of these should be available in your graphing software.

The spectrum for valerophenone will not look like the one shown in Figure S3.11, but rather like the one shown in Figure 3.5A. Figure S.11 (in blue) shows the fraction of the light absorbed by the valerophenone solution at each wavelength. To convert to this format a few simple calculations are required. In our case, we use Kaleidagraph as our graph software, but other common applications, such as Origin will have similar capabilities. Excel or Numbers can also be used but they lack the convenience of scientific software.

• Convert the data to transmittance (T); $T = 10^{-A}$.

• The fraction of light absorbed at each wavelength will be: '1 – T'

• At each wavelength the fraction of lamp light absorbed by your solution will be given by:

Fraction of light absorbed at λ = (1-T) x normalized light intensity at λ.

This is the blue plot in Figure S3.11.

• Now plot in the same graph the lamp spectrum and the fraction of light absorbed and you have the plot of Figure S3.11 (lamp in red, sample in blue)

• Finally, you need to integrate or use the sum function to determine the fraction of lamp light absorbed by your sample, that is divide the two areas under the curves obtained from the sums (Σ) of the two plots in Figure S3.11. If your data is perfectly spaced at integer values wavelength, then the sum function is more convenient (and equivalent) to the integral.

$$fraction\ of\ light\ absorbed = \frac{\sum_\lambda Light\ fraction\ absorbed\ by\ sample\ (blue)}{\sum_\lambda Normalized\ irradiance\ (red)} \times 100 \qquad (S6)$$

where the colors refer to those used in Figure S3.11.

• In our case this analysis leads to 34.7% light absorption by valerophenone 0.1 M corrected for a 1.5 mm optical path and integrated between 300 and 420 nm, for a standard UVA lamp (model LZC-355-022).

Note that these calculations are only needed to convert absorbed photons (I_a) to incident photons (I_0), otherwise, the simple calculations of Figure 3.4 and equation 5 would suffice.

If you are using a different geometry the same calculations will apply, but you have to establish the correct optical path in your system. The value of 0.15 cm that we used here only applies if you use the same geometry and Teflon tubing. Using lamps from a different supplier will not affect the calculations, but the correct lamp spectrum needs to be obtained.

3.4 Accompaniment to Chapter

The design and study of this flow photochemistry setup have significantly advanced our research capabilities, providing us with a robust platform to enhance and fine-tune synthetic chemistry processes. The innovative arrangement of light sources and reactor setup not only increased the efficiency of photochemical reactions but also allowed for greater control over reaction conditions. This breakthrough has made the way for more precise and scalable chemical synthesis.

In the next chapter, Chapter 4, we will detail how this setup has been applied to the production of sustainable silver nanoparticles. We will explore the specific modifications and optimizations made to the reactor design to facilitate this process. Additionally, this system helped us to collaborate with industry partners to further refine and apply the photochemistry process to the synthesis of vitamin D_2. This partnership aims to leverage our combined expertise to enhance the yield and purity of vitamin D_2 isomers' production, demonstrating the practical and commercial applications of our advanced photochemical setup.

3.5 References

(1) Scaiano, J. C. (Tito). *Photochemistry Essentials*; ACS In Focus; American Chemical Society, 2022. https://doi.org/10.1021/acsinfocus.7e5031.

(2) Rabani, J.; Mamane, H.; Pousty, D.; Bolton, J. R. Practical Chemical Actinometry—A Review. *Photochem. Photobiol.* **2021**, *97* (5), 873–902. https://doi.org/10.1111/php.13429.

(3) Wagner, P. J.; Kelso, P. A.; Kemppainen, A. E.; McGrath, J. M.; Schott, H. N.; Zepp, R. G. Type II Photoprocesses of Phenyl Ketones. Glimpse at the Behavior of 1,4 Biradicals. *J. Am. Chem. Soc.* **1972**, *94* (21), 7506–7512. https://doi.org/10.1021/ja00776a037.

(4) Pitre, S. P.; McTiernan, C. D.; Vine, W.; DiPucchio, R.; Grenier, M.; Scaiano, J. C. Visible-Light Actinometry and Intermittent Illumination as Convenient Tools to Study Ru(Bpy)3Cl2 Mediated Photoredox Transformations. *Sci. Rep.* **2015**, *5* (1), 16397. https://doi.org/10.1038/srep16397.

(5) Hatchard, C. G.; Parker, C. A.; Bowen, E. J. A New Sensitive Chemical Actinometer - II. Potassium Ferrioxalate as a Standard Chemical Actinometer. *Proc. R. Soc. Lond. Ser. Math. Phys. Sci.* **1956**, *235* (1203), 518–536. https://doi.org/10.1098/rspa.1956.0102.

(6) Wagner, P. J. Type II Photoelimination and Photocyclization of Ketones. **1971**.

(7) Wagner, P. J.; Kochevar, I. E.; Kemppainen, A. E. Type II Photoprocesses of Phenyl Ketones. Procedures for Determining Meaningful Quantum Yields and Triplet Lifetimes. **1971**.

(8) Small, R. D.; Scaiano, J. C. Interaction of Oxygen with Transient Biradicals Photogenerated from γ-Methyl Valerophenone. *Chem. Phys. Lett.* **1977**, *48* (2), 354–357. https://doi.org/10.1016/0009-2614(77)80331-X.

(9) Small, R. D.; Scaiano, J. C. Differentiation of Excited-State and Biradical Processes. Photochemistry of Phenyl Alkyl Ketones in the Presence of Oxygen. **1978**.

(10) Roibu, A.; Fransen, S.; Leblebici, M. E.; Meir, G.; Van Gerven, T.; Kuhn, S. An Accessible Visible-Light Actinometer for the Determination of Photon Flux and Optical Pathlength in Flow Photo Microreactors. *Sci. Rep.* **2018**, *8* (1), 5421. https://doi.org/10.1038/s41598-018-23735-2.

(11) Vandekerckhove, B.; Piens, N.; Metten, B.; Stevens, C. V.; Heugebaert, T. S. A. Practical Ferrioxalate Actinometry for the Determination of Photon Fluxes in Production-Oriented Photoflow Reactors. *Org. Process Res. Dev.* **2022**, *26* (8), 2392–2402. https://doi.org/10.1021/acs.oprd.2c00079.

(12) Achi, N. E.; Bakkour, Y.; Chausset-Boissarie, L.; Penhoat, M.; Rolando, C. Rapid and Facile Chemical Actinometric Protocol for Photo-Microfluidic Systems Using Azobenzene and NMR Spectroscopy. *RSC Adv.* **2017**, *7* (47), 29815–29820. https://doi.org/10.1039/C7RA01237C.

(13) Aillet, T.; Loubiere, K.; Dechy-Cabaret, O.; Prat, L. Accurate Measurement of the Photon Flux Received Inside Two Continuous Flow Microphotoreactors by Actinometry. *Int. J. Chem. React. Eng.* **2014**, *12* (1), 257–269. https://doi.org/10.1515/ijcre-2013-0121.

(14) Rehm, T. H. Flow Photochemistry as a Tool in Organic Synthesis. *Chem. – Eur. J.* **2020**, *26* (71), 16952–16974. https://doi.org/10.1002/chem.202000381.

(15) Cambié, D.; Bottecchia, C.; Straathof, N. J. W.; Hessel, V.; Noël, T. Applications of Continuous-Flow Photochemistry in Organic Synthesis, Material Science, and Water Treatment. *Chem. Rev.* **2016**, *116* (17), 10276–10341. https://doi.org/10.1021/acs.chemrev.5b00707.

(16) Wagner, P. J.; Kelso, P. A.; Zepp, R. G. Type II Photoprocesses of Phenyl Ketones. Evidence for a Biradical Intermediate. *J. Am. Chem. Soc.* **1972**, *94* (21), 7480–7488. https://doi.org/10.1021/ja00776a033.

(17) Turro, N. *Modern Molecular Photochemistry*; 1991.

(18) Braslavsky, S. E. Glossary of Terms Used in Photochemistry. *Pure Appl. Chem.* **2007**, *79* (3), 293–465. https://doi.org/10.1351/pac200779030293.

(19) Wriedt, B.; Ziegenbalg, D. Common Pitfalls in Chemical Actinometry. *J. Flow Chem.* **2020**, *10* (1), 295–306. https://doi.org/10.1007/s41981-019-00072-7.

(20) Gessner, F.; Scaiano, J. C. Importance of Entropy Terms in Triplet Energy Transfer Equilibria. *J. Am. Chem. Soc.* **1985**, *107* (24), 7206–7207. https://doi.org/10.1021/ja00310a091.

(21) Shrestha, N. K.; Yagi, E. J.; Takatori, Y.; Kawai, A.; Kajii, Y.; Shibuya, K.; Obi, K. Photochemical *α*-Cleavage Reaction of Benzoin and Its Derivatives. *J. Photochem. Photobiol. Chem.* **1998**, *116* (3), 179–185. https://doi.org/10.1016/S1010-6030(98)00308-6.

(22) Lewis, F. D.; Lauterbach, R. T.; Heine, H. G.; Hartmann, W.; Rudolph, H. Photochemical .Alpha. Cleavage of Benzoin Derivatives. Polar Transition States for Free-Radical Formation. *J. Am. Chem. Soc.* **1975**, *97* (6), 1519–1525. https://doi.org/10.1021/ja00839a041.

(23) Scaiano, J. C.; Billone, P.; Gonzalez, C. M.; Marett, L.; Marin, M. L.; McGilvray, K. L.; Yuan, N. Photochemical Routes to Silver and Gold Nanoparticles. *Pure Appl. Chem.* **2009**, *81* (4), 635–647. https://doi.org/10.1351/PAC-CON-08-09-11.

(24) McGilvray, K. L.; Decan, M. R.; Wang, D.; Scaiano, J. C. Facile Photochemical Synthesis of Unprotected Aqueous Gold Nanoparticles. *J. Am. Chem. Soc.* **2006**, *128* (50), 15980–15981. https://doi.org/10.1021/ja066522h.

(25) Jockusch, S.; Landis, M. S.; Freiermuth, B.; Turro, N. J. Photochemistry and Photophysics of α-Hydroxy Ketones. *Macromolecules* **2001**, *34* (6), 1619–1626. https://doi.org/10.1021/ma001836p.

Chapter 4. Facile Scale-Up of the Flow Synthesis of Silver Nanostructures Based on Norrish Type I Photoinitiators

4.1 Preamble to Chapter

The previous chapter (chapter 3) introduced a straightforward actinometer design for flow photoreactions, based on a Norrish Type II reaction. This actinometer allows for accurate measurement of photon flux in flow reactors, offering a reliable and easy-to-use method for monitoring and optimizing photochemical processes. The study demonstrated the utility of this setup in various photoreactions, highlighting its importance for researchers working with flow photochemistry.

This chapter explores the synthesis and optimization of silver nanoparticles (AgNPs) in flow conditions. The previously described system, with its ability to accurately measure photon flux in flow reactors, proved instrumental in the development of our photochemical processes.

Silver nanoparticles (AgNPs) are crucial in various fields due to their unique properties. They exhibit strong antimicrobial activity, making them valuable in medical applications such as coatings for medical devices and antibacterial agents. Their high surface area-to-volume ratio enhances their reactivity, which is beneficial in catalysis and environmental applications like water purification. Additionally, AgNPs have unique optical properties, enabling their use in biosensing and imaging. Their synthesis is important for advancing technologies in healthcare, environmental protection, and nanotechnology-based devices.

In this project, we used two approaches: my colleague Connor conducted batch experiments, and I did flow experiments with our supervisor's guidance. Batch experiments helped us fine-tune the reaction conditions in a controlled setting, while flow experiments allowed us to test the process in a way that could be scaled up for industrial use.

By combining what we learned from our actinometer studies with a detailed investigation of silver nanoparticle (AgNP) synthesis, we aimed to create a reliable and scalable method for producing AgNPs. This chapter explains our experimental design, methods, and results, showing how fundamental photochemistry and applied nanotechnology worked together in our research.

4.2 Post-print version of the manuscript

First published in Molecules. 2023;28(11):4445.

This chapter has been adapted from Molecules journal with permission as the author of this article.

4.2.1 Abstract

Silver nanoparticles have become one of the most commercially and industrially relevant nanomaterials of the 21st century, owing to their potent antibacterial properties, as well as their useful catalytic and optical properties. Although many methods have been explored to produce AgNPs, we favour the photochemical approach using photoinitiators to produce AgNPs, owing to the high degree of control over reaction conditions, and the generation of so-called AgNP 'seeds' that can be used as is, or as precursors for other silver nanostructures. In this work, we explore the scale-up of AgNP synthesis using flow chemistry and assess the usefulness of a range of industrial Norrish Type 1 photoinitiators in terms of flow compatibility and reaction time, as well as the resulting plasmonic absorption and morphologies. We establish that while all the photoinitiators used were able to generate AgNPs in a mixed aqueous/alcohol system, photoinitiators that generate ketyl radicals showed the greatest promise in terms of reaction times, while also showing greater flow compatibility compared to photoinitiators that generate α-aminoalkyl and $\boldsymbol{\alpha}$-hydroxybenzyl radicals. These findings help to establish a guideline for adapting photochemical AgNP syntheses to flow systems, helping to improve the scalability of the method in one of the largest industries in nanomaterial chemistry.

4.2.2 Introduction

Numerous free radical photoinitiators have been designed based on the Norrish Type I reaction involving C-C α-cleavage of carbonyl compounds.[1–4] In selected cases, one of the radicals generated is a strong electron donor; such systems are of great interest for the production of metal nanoparticles as they produce reducing agents with excellent spatial and temporal control.[1,5–7] Further, an additional benefit is kinetic control, as the light source irradiance can be readily adjusted by either controlling the power supplied (dimming) or simply changing the source-sample distance.

Many metal ions are excellent quenchers of excited states and frequently this quenching can limit the efficiency of photoinitiators. For these initiators to be effective, the Norrish Type I cleavage must be extremely fast and since most cleavages occur from the triplet state, this requires very short-lived triplet states.[5] A molecule that we have long recognized as a good nanoparticle precursor is Irgacure-2959 (I-2959), which has been widely employed in our group. I-2959 has a triplet lifetime of ~8 ns[3] and cleaves with a quantum yield of one in acetonitrile[8], Scheme 4.1.

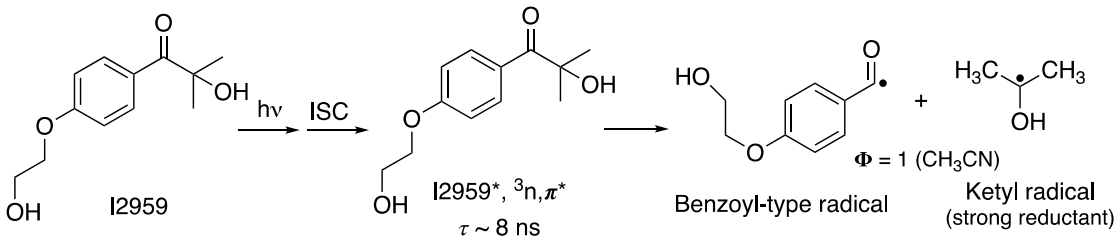

Scheme 4.1. Mechanism for the decomposition of Irgacure 2959 (I-2959) showing the formation of the strongly reducing ketyl radical. Under typical reaction conditions the benzoyl radical yields the corresponding carboxylic acid that can behave as a mild nanoparticle stabilizer.

Early work on the use of carbonyl compounds to generate metal nanoparticles frequently required very long exposure times[9], probably the result of the use of molecules with long-lived triplets that were readily quenched by the metal ions, typically Ag(I) or Au (III). Further, the need to generate strongly reducing radicals was not always recognized.

Among reducing radicals, ketyl and ***α***-aminoalkyl radicals are convenient sources, both operating by proton-coupled electron transfer reactions (PCET) and with commercial precursors readily available.[1] Scheme 4.2 illustrates the mechanism for silver; although, the same applies (with adjusted stoichiometry) for other ions, such as Au (III). Once the silver atoms have been produced, their next step is to form Ag_2, eventually leading to nanoparticle formation.[10]

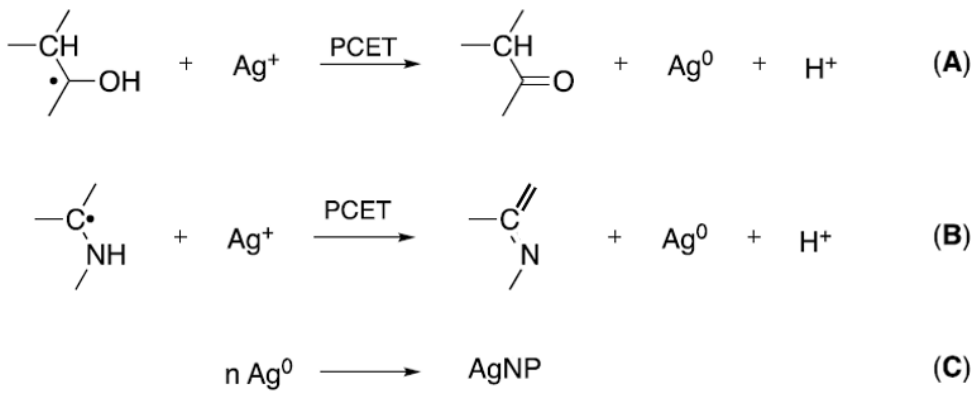

Scheme 4.2. Electron transfer from ketyl and α-aminoalkyl radicals to reduce Ag(I) to Ag(0), reactions A and B, respectively, which eventually generates silver nanoparticles (AgNP), reaction C.

In this contribution, we examine several readily available radical photoinitiators frequently used in polymerization applications; although, our applications concentrate on the synthesis of nanostructures, illustrated here with silver seeds, small nanoparticles that we require for the production of other nanostructures with biological applications. We know that the morphology and size dispersity of nanostructures can depend on the precursor, including distinct byproducts, as well as on other additives, such as citrate that are of particular interest for our applications.

While nanoparticle synthesis is usually performed in batch reactions, in the last decade, there has been an interest in converting many reactions to flow systems, where scale-up is frequently easier and safety risks, if applicable, can be reduced.[11,12] In our laboratory, we have recently developed a flow actinometer that allows the quantification of the key reagent in photochemical reactions: light.[8] As we determined experimental irradiances in the UVA and UVB regions, we realized that our experimental geometry was exceptionally efficient in delivering photons to a flow reactor consisting of a narrow Teflon tube. In fact, in our preliminary work, we studied how short the residence time (<60 s) of the sample could be, and we discovered that our pumps were not fast enough to establish a threshold for quantitative Ag+ to Ag0 conversion. The answer to this issue is presented in the sections that follow. Scheme 4.3 shows the structures we tested.

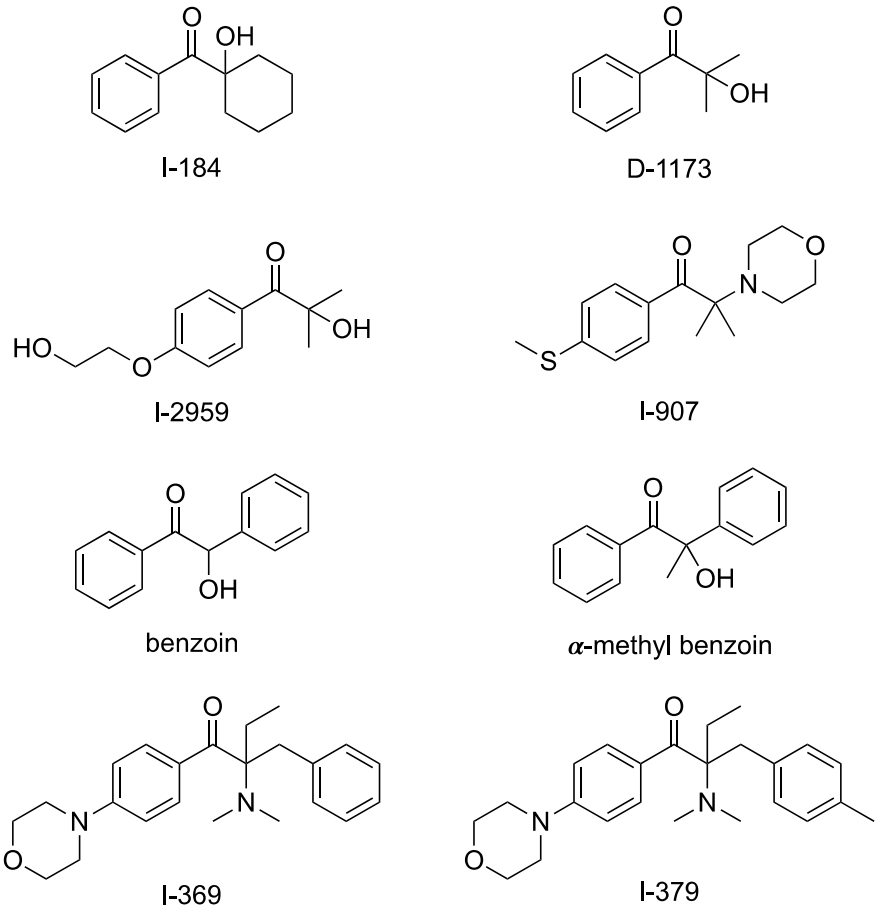

Scheme 4.3. Structure of the molecules studies as precursors for AgNP. The letter 'I' is used as an abbreviation for Irgacure, and 'D' is used as an abbreviation for Darocur.

4.2.3 Results and discussion

This section is divided according to the methodologies used to synthesize nanoparticles and their characterization. The objective of this contribution is to establish a fast and reliable method to produce silver nanoparticles in a continuous flow. These small particles are sometimes described as 'seeds' and can be used to generate complex silver structures.[13]

4.2.3.1 Spectroscopy of initiators and lamps used

Our studies were performed with several photoinitiators that generate strongly reducing free radicals of the ketyl or α-aminoalkyl type with the structures shown in Scheme 4.3. They usually have strong absorptions in the UVA or UVB region and their spectra are shown in Figure

4.1A. The spectra for the UVA and UVB lamps used (mostly the latter) are shown in Figure 4.1B. The same wavelength scale is used for both to facilitate vertical comparisons.

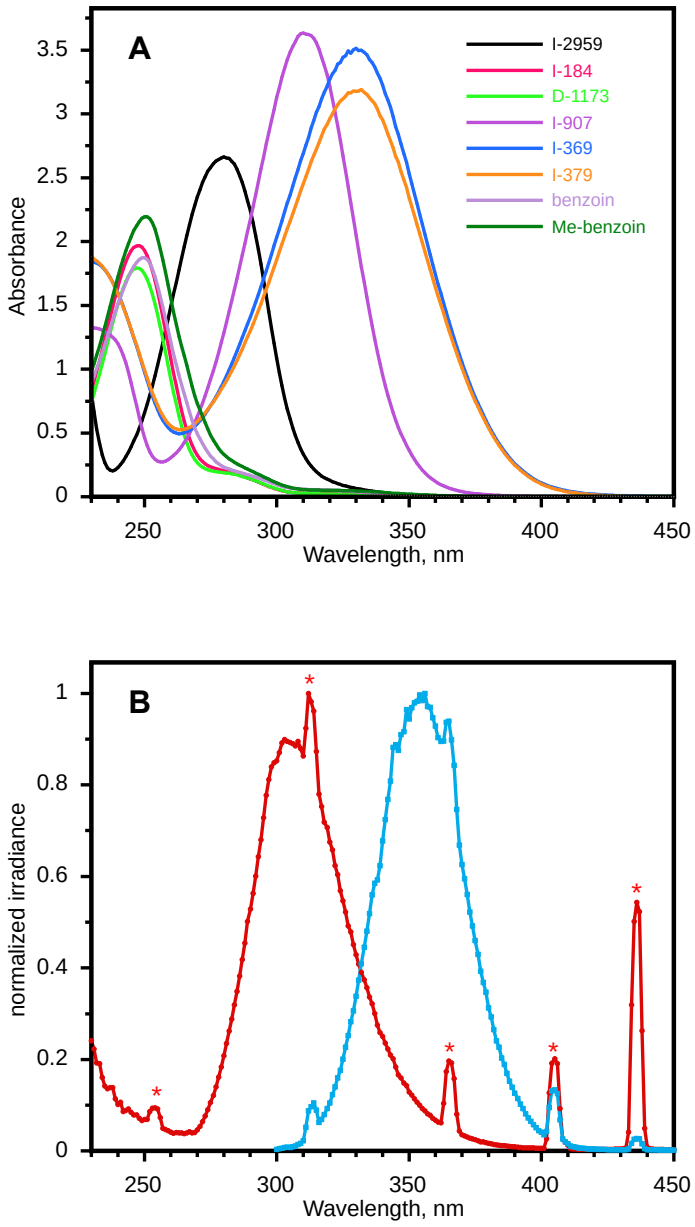

Figure 4.1. (A) Spectra of the initiators used at 0.2 mM in 1:1 aqueous methanol. All spectra in panel A were recorded using a Cary 7000 spectrometer that can handle high absorbances, as the Cary 60 instrument used elsewhere in this paper showed saturation at A > 2.7 in a 1 cm cuvette. The actual optical path under flow conditions is 0.15 cm and there is no saturation under these conditions. (B) Normalized spectra for the UVA (blue) and UVB (red) lamps utilized in this work. The sharp lines are leftovers (marked with '*') from typical mercury emission lines at 254, 313, 365, 405, and 436 nm.

4.2.3.2 Batch Experiments and Controls

A number of preliminary batch experiments were performed in order to find out the preferred conditions for the flow work on which this contribution centers. In spite of the low concentrations required (frequently sub-millimolar) some of the initiators showed limited aqueous solubility, the exception being I-2959, where its glycol-like moiety facilitates solubility while also causing a red shift in the absorbance. Three co-solvents were tested: acetonitrile, ethanol, and methanol. The results with acetonitrile were disappointing as it seemed to slow down or inhibit nanoparticle formation, even at amounts as low as 10%, while the alcohols performed well. In the end, we settled on 50:50 methanol/H_2O (v/v) as the preferred solvent (but not the only one) as it seemed compatible with all the initiators, with $AgNO_3$ and with citrate used as a particle stabilizer. An example of solvent studies is presented in Figure 4.2 for I-2959 irradiated with UVB light for 15 min under an argon atmosphere; here, the Ag plasmon band seems best for 25% methanol; however, 50% still shows a well-resolved band and is a better choice when taking solubilities into consideration. Furthermore, when >50% MeOH was used, the absorption of the AgNP suspensions began to drop considerably. For this reason, the reaction condition chosen for flow reactions going forward was 1:1 MeOH: H_2O.

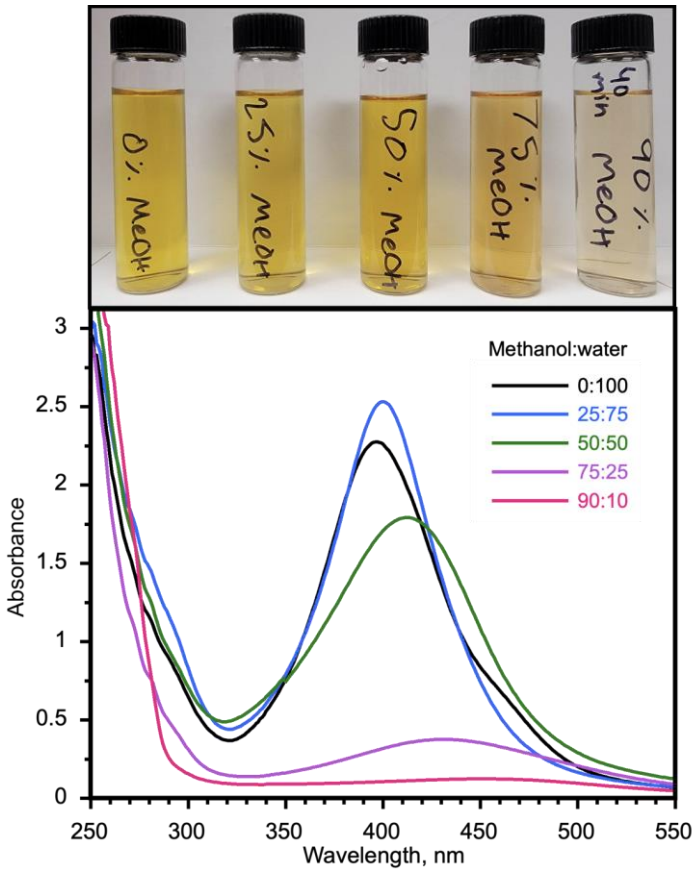

Figure 4.2. AgNPs are synthesized in solutions containing different fractions of CH_3OH ranging from 0% to 90%. Each reaction initially contains 1 mM citrate, 0.2 mM $AgNO_3$, and 0.2 mM of I-2959. All samples were irradiated for 15 min in a photoreactor with 6 UVB lamps, except for the 90% CH_3OH sample, which required 40 min to yield any noticeable colour.

A very interesting observation from the batch experiments is that the initiator to Ag^+ stoichiometric ratio required is less than one. If in Scheme 4.1 one assumes that only the ketyl radical leads to Ag^+ reduction, then the minimum stoichiometric requirement would be 1.0. This is illustrated in Figure 4.3, where, for example, an 82% yield is obtained with 0.1 mM I-2959 and 0.2 mM Ag^+, when the maximum anticipated yield would be 50% if only the ketyl radical is reactive. Clearly, the other materials in the reaction, citrate or methanol, may contribute to the reduction process. Citrate is known to be a modest reducing agent towards silver[14] and an established one in the case of gold.[15] In the case of methanol, the $\dot{C}H_2OH$ radical is a good reducing agent, but its formation would require H-abstraction by the benzoyl radical of Scheme

4.1, a process that is expected to be slow, given the C-H bond dissociation energy of methanol,[16] yet some contribution may be expected given that methanol is 12.4 M in the system.

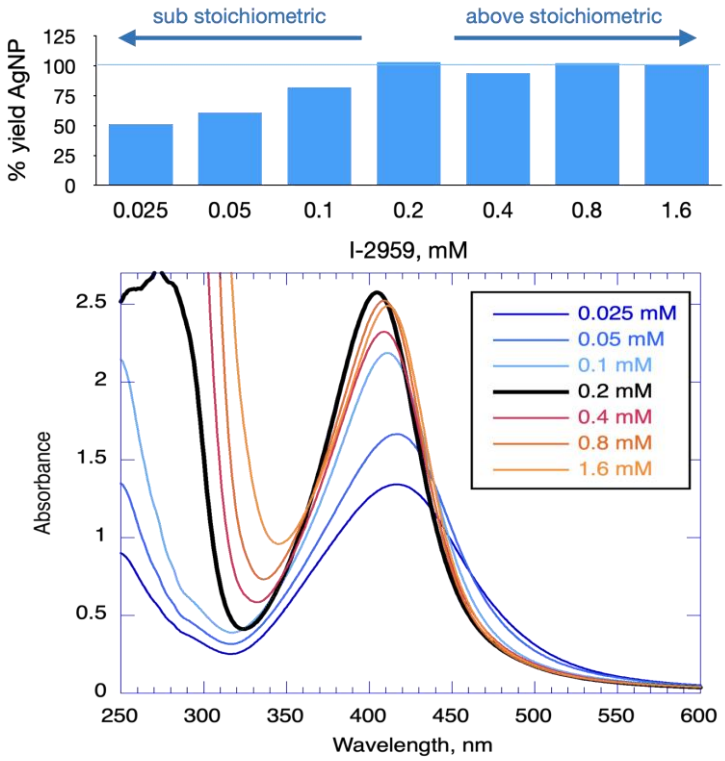

Figure 4.3. Effects of varying photoinitiator concentration in batch reaction. Top: Relative max absorption yield for AgNP suspensions in comparison to the stoichiometric ratio of I-2959 to $AgNO_3$ for solutions with I-2959 concentrations ranging from 0.025 to 1.6 mM. Each reaction uses 0.2 mM of $AgNO_3$, 1 mM of citrate, and 1:1 CH_3OH: H_2O. Solutions were irradiated for 15 min in a photoreactor with six 8W UVB bulbs. Bottom: Corresponding UV–Vis absorption spectra of AgNP plasmon bands with varying concentrations of I-2959. The black heavier line corresponds to the stoichiometric concentration of I-2959. Note that the 0.1 mM initiator (light blue) generates 82% of the signal obtained with the stoichiometric concentration.

Among the initiators in Figure 4.1, I-369 and I-379 are interesting because of their excellent absorbance match with the emission of the UVA lamp, something that may be advantageous in the presence of organic molecules (e.g., produced in catalytic processes) that are more likely to photodegrade with UVB than with UVA. However, this initiator presents consistency problems mentioned in the Supplementary Materials and addressed also in the flow experiments section.

Based on the results of bench experiments, it was decided to proceed using 0.2 mM of initiator, 0.2 mM of $AgNO_3$, and 1 mM of trisodium citrate dissolved in 1:1 MeOH: H_2O in order to best dissolve all of the initiators, while still producing AgNPs with strong, consistent plasmon bands.

Table 4.1. Summary of flow photochemistry results of silver nanoparticle production with different initiators, using 0.2 mM of $AgNO_3$, 0.2 mM of initiator, and 1 mM of citrate in a deaerated solvent with UVB lamp (see Scheme 4.3).

Initiator	Solvent	λ_{max} FWHM (nm)	Residence Time (min)	Notes
I-184	H_2O	400 50	0.8	Clean no deposits in the flow tube
	1:1 CH_3OH: H_2O	420 100	4	
D-1173	H_2O	400 60	0.8	Clean no deposits in the flow tube
	1:1 CH_3OH: H_2O	415 95	0.8	
I-2959	H_2O	400 50	0.7	Clean no deposits in the flow tube
	1:1 CH_3OH: H_2O	415 80	0.8	
I-907	1:9 CH_3OH: H_2O	445 160	4	Heavy black deposits in the flow tube
	1:1 CH_3OH: H_2O	445 150	8	
Benzoin	H_2O	400 85	30	Very weak signals
	1:1 CH_3OH: H_2O	410 80	0.8	Yellow deposits in the flow tube
α-MeBenzoin	H_2O	400 70	0.8	Yellow deposits in the flow tube
	1:1 CH_3OH: H_2O	405 80	0.8	Faint yellow deposits in the flow tube
I-369 [a]	1:1 CH_3OH: H_2O	410 90	4	Heavy black deposits in the flow tube
I-379	1:1 CH_3OH: H_2O	410 90	6	Heavy black deposits in the flow tube
	2:3 CH_3OH: H_2O	410 80	10	

[a] I-369 results are the same for UVA and UVB light (Figure S14).

Several other experiments were performed in batch and are described in the Supplementary Materials. In general, they show that the first three entries in Table 4.1 yield AgNP in a clean fast process with plasmon bands consistent with predominantly spherical particles, something confirmed in the TEM images (Figures S4.6–S4.13). Our best and most consistent results were obtained with initiators that yield ketyl radicals. The next section illustrates the excellent performance of ketyl radical generators under flow conditions.

4.2.3.3 Nanoparticle Synthesis Using Flow Strategies

The synthesis of AgNPs in flow was performed using the same experimental strategy as in a recent paper where we developed an actinometer for flow photoreactions.[8] Briefly, we utilize as light source 8 W fluorescent tubes from Luzchem, which are 30 cm long and with a diameter of 16 mm. The lamp is tightly wrapped with Teflon tubing with an outside diameter of 1.80 mm and an inside diameter of 1.50 mm corresponding to a wall thickness of 0.15 mm. The flow cavity in the tube is about 6.3 m long with a liquid capacity of 10 mL. The experimentally determined optical path is 0.15 cm.[8] The sample is supplied by a peristaltic pump with adjustable flow rate feeding from a container where the sample can be deaerated, normally with argon. At the exit, samples can be collected in vials or cuvettes or be directly fed to a flow cell in a Cary-60 absorbance spectrometer. Particles undergo ripening over the next few hours in a process that can also depend on the presence or not of oxygen; however, the spectra shown below correspond to nascent particles under argon and the time lapse between the flow system and the spectrometer is usually less than one minute. We note at the onset that the most reliable initiators were those yielding ketyl radicals. This is illustrated in Figure 4.4, for a very short residence time, where all three initiators yield approximately the same plasmon band with comparable absorbance.

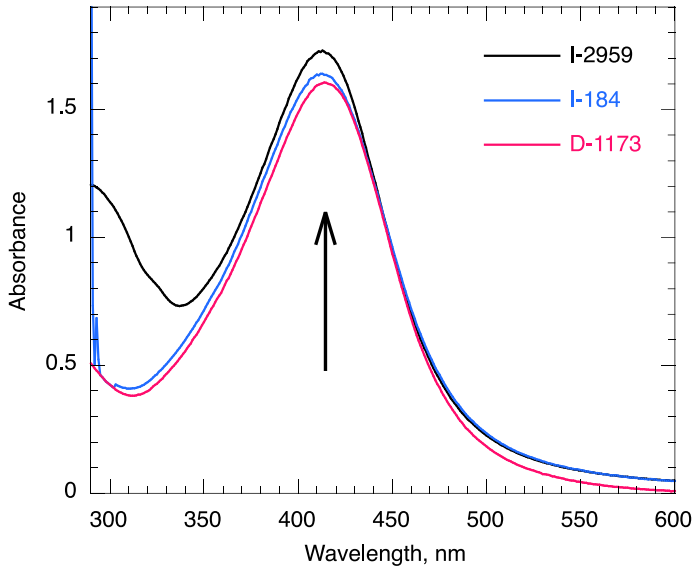

Figure 4.4. Comparison of initiators yielding ketyl radicals with high efficiency, produced under flow conditions with 0.2 mM of each photoinitiator, 0.2 mM of $AgNO_3$, 1 mM of citrate, and 1:1 CH_3OH: H_2O and a residence time of 0.8 min. The arrow indicates growth during irradiation. The spike at 290 nm in the I-184 graph is due to bubbles in the flow.

Figure 4.5 shows the spectra recorded for AgNP with different residence times; the remarkable observation is that a residence time of 40 s is enough to achieve the 100% conversion of a 0.2 mM Ag^+ solution, this short residence time corresponds to the maximum flow speed for our pump and is equivalent to nearly one liter per hour. The reality is that we do not know how fast we could go and still have 100% conversion; however, it is interesting to note that the residence time of 0.8 min is much shorter than the required irradiation time of 15 min seen in the batch reaction, which yields only 6 mL of product.

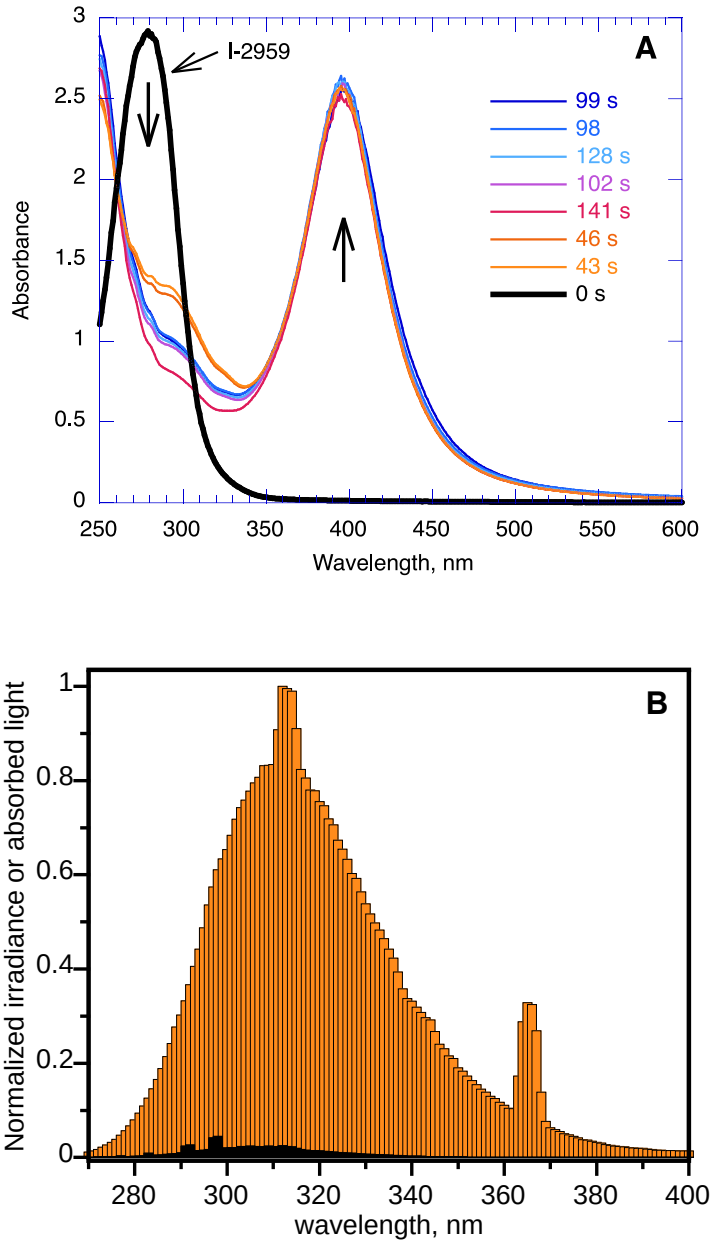

Figure 4.5. (A) Different residence times irradiated with UVB light and using I-2959 as initiator. Note that the residence times are not in increasing order, but rather are randomized; this is done to make sure any effects observed are not the result of a systematic change in the conditions. Silver nitrate (0.2 mM), sodium citrate (1 mM), I-2959 (0.2 mM) in H_2O, purged with Argon and irradiated with a UVB lamp with different residence times (seconds) in 6.3 m Teflon tubing with a total irradiated volume of 10 mL. The arrow indicates growth during irradiation; (B) spectral distribution of the UVB lamp (normalized, orange) and the fraction of light absorbed by the I-2959 solution (black), the spectrum corrected for 0.15 cm optical path.

The high yield contrasts with the fact that only 2.17% is being absorbed by I-2959 at a 0.2 mM concentration for the 1.5 mm optical path of the Teflon tubing. Intrigued by this result we used the actinometric determination method that we developed,[8] to compare the chemical conversion of 0.2 mM with the light absorbed by the initiator (see our recent contribution on actinometry for detailed calculations[8]). In the shortest (40 s) residence time, the dose absorbed was 0.00012 Einstein L^{-1}. This leads to a quantum yield for the $Ag^{+} \rightarrow Ag^{0}$ conversion of 1.67 ± 0.17. Clearly more than one Ag^{+} conversion per photon, but probably not high enough to suspect a chain reaction. We suspect that this is an autocatalytic process, just as it is in silver photography, where silver clusters lead to the reduction of neighbouring Ag^{+} or salts in the presence of a reducing agent.[17] Possibly the UVB illumination contributes to this growth. The reducing agent can be methanol or citrate, more likely the latter. This is consistent with the results of batch experiments and illustrated in Figure 4.3. In general, I-2959, I-184, and D-1173 showed very similar behavior, and the results obtained, along with those for other initiators are summarized in Table 4.1, with further details available in the supplementary materials. The photochemistry of some of these initiators has been examined in a classic publication from Turro's group.[3]

Another example with more complex photochemistry is shown in Figure 4.6 for I-379, where the initiator (λ_{max}~325 nm) has a good overlap with the UVB lamp (see Figure 4.1) and is rapidly consumed, with essentially none left after 3.1 min. However, the AgNP plasmon band continues to grow and peaks at ~29 min. Once again, this suggests that the growth of the plasmon band reflects an autocatalytic process similar to that in silver photography[17], but stimulated by light. Notice also that the Teflon tubing (see top inset) develops black deposits after the flow tube has been used for 3 h. These deposits are believed to be silver or Ag_2O formed during prolonged exposure. We note that no deposits were observed when I-2959, I-184, or D-1173 were used as initiators. The deposits can be readily removed by flowing nitric acid and the Teflon tube can be reused.

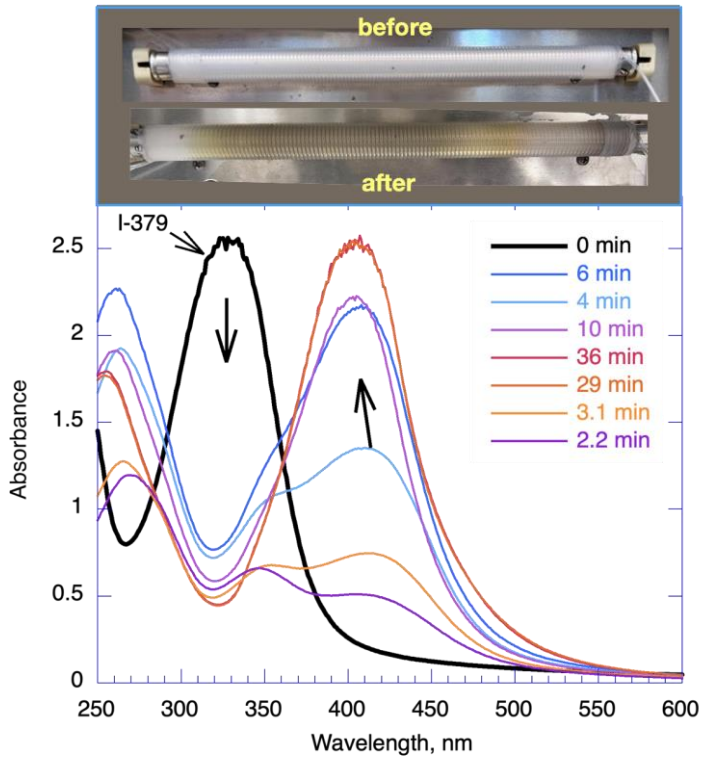

Figure 4.6. Different residence times irradiated with UVB light and using I-379 as initiator. Silver nitrate (0.2 mM), sodium citrate (1 mM), I-379 (0.2 mM) in 2:3 CH_3OH: H_2O purged Argon and irradiated with a UVB lamp with different residence times. Notice that the initiator (black with λ_{max}~323 nm is consumed in the first 2 min and has a slight blue shift at long irradiation times. The inset at the top shows the Teflon-wrapped lamp before and after the experiment by using I-379 as an initiator. Notice the black deposits on the latter.

Initiator I-369 showed behaviour very similar to I-379, as expected, given the similarity of the two structures (see Table 4.1).

Initiator I-907 shows the best overlap with the UVB lamp (see Figure 4.1), producing strongly reducing $\boldsymbol{\alpha}$-aminoalkyl radicals, and the sulphur center should help stabilize nanoparticles. Its performance is good, but it produces nanostructures with a shifted plasmon band (~440 nm compared with the typical 395 nm), and the band is quite broad, Figure 4.7. The plasmon band stops growing after 8–10 min.

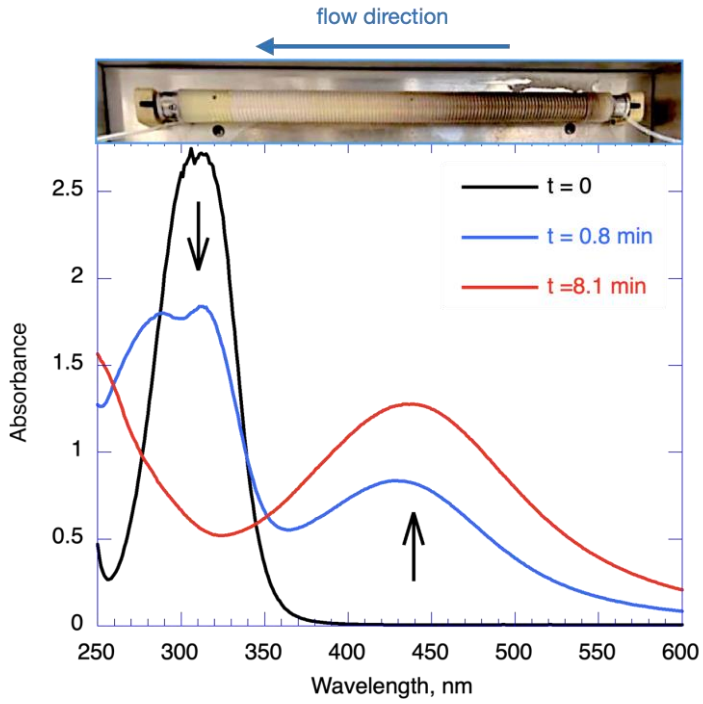

Figure 4.7. Different residence times irradiated with UVB light and using I-907 as initiator. Silver nitrate (0.2 mM), I-907 (0.2 mM), trisodium citrate (1 mM), and 1:1 CH_3OH: H_2O purged with argon. The inset at the top shows the Teflon-wrapped lamp after using I-907 as an initiator. Notice the black deposits, and in particular the dark areas are predominantly on the right side from which the reagents are fed to the system.

The photochemistry of I-907 generates reducing α-aminoalkyl radicals (Scheme 4.4). The benzoyl radical is expected to form the corresponding aldehyde or carboxylic acid, and both can stabilize AgNP, given the presence of a thioether.

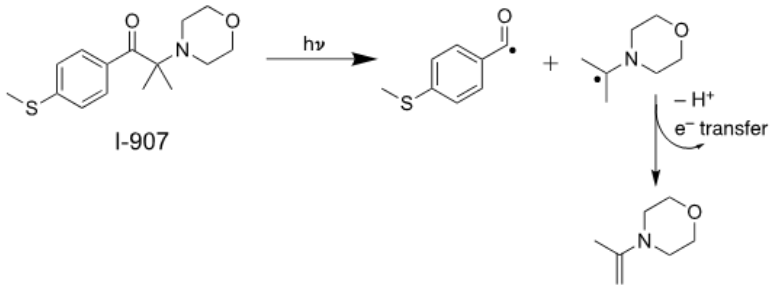

Scheme 4.4. Anticipated Norrish Type I reaction of I-907 and chemistry of the α-aminoalkyl radical.

Overall, I-907 is a reasonable initiator but produces particles with a red-shifted plasmon band and requires periodic nitric acid treatment of the Teflon tubing to clean up the silver deposits. This process is simple and fast, and the published Supplementary Materials includes a video S1 illustrating the cleaning process showing that the silver removal occurs as soon as the nitric acid front moves along the tube.[18]

Finally, we come to the examples of benzoin and α-methylbenzoin. Benzoin is known to have a very short triplet state with a lifetime of around 1 ns.[2,19] Reports normally use non-aqueous solvents; although, measurements in methanol have been reported.[2] Benzoin has a rather low extinction coefficient, which becomes a disadvantage, for example, in polymer chemistry applications.[4] Frequently, the absorbance is enhanced by the addition of thioether substitution,[3,4] something that is also evident when comparing the spectra of benzoin and I-907 in Figure 4.1. To the best of our knowledge, benzoin has not been studied in water.

Unfortunately, benzoin proved to be a very inefficient initiator in water, but it was reasonably efficient in 50% aqueous methanol, see Figure 4.8. In contrast, α-methyl benzoin was very efficient, even in water (Figure 4.8A), while the absorption spectra of the two ketones are very similar, with λmax~250 nm.

In 50% aqueous methanol, the performance is good. Notice that after 1.3 min, the main effect of irradiation is a red shift of the plasmon band and a gradual decrease in absorbance at the maximum. Overall, while benzoin seems a challenging initiator, α-methylbenzoin seems straightforward and quite efficient, even in water (Figure 4.8A). We speculated that benzoin in water may undergo some enolization, but the very limited aqueous solubility led to the failure of the NMR work aimed at detecting any enol formation. In the context of this work, which is aimed at practical recommendations for initiators for nanoparticle fabrication, benzoin is not recommended, while α-methylbenzoin is.

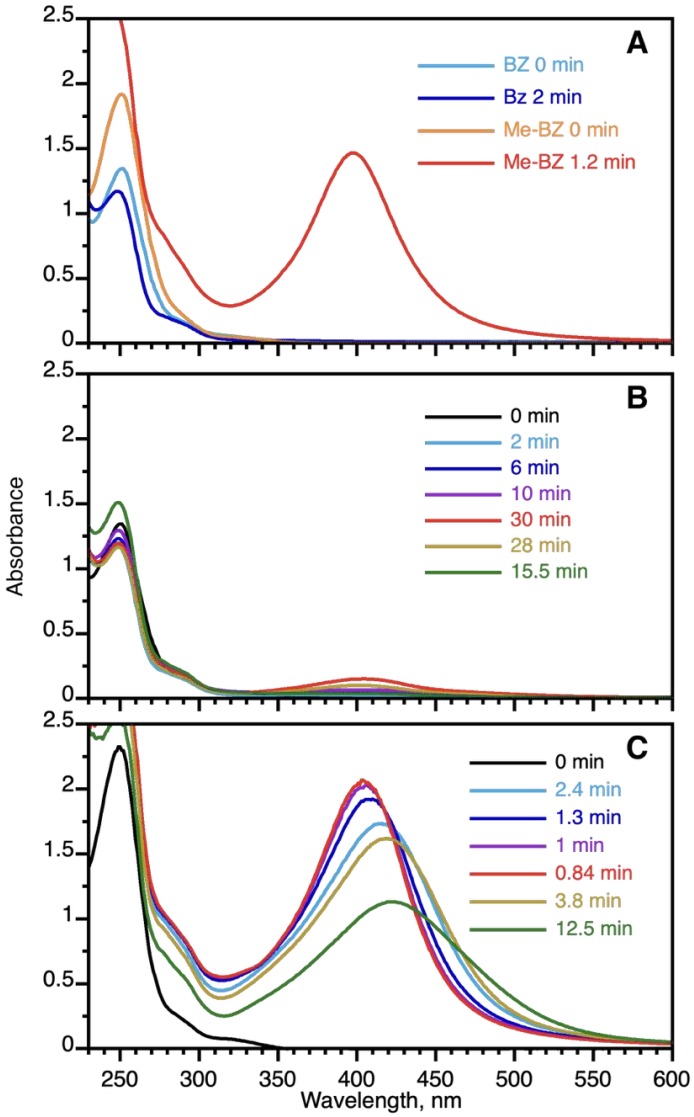

Figure 4.8. Benzoin as an initiator for spectra corresponding to different residence times in minutes. Silver nitrate (0.2 mM), benzoin (0.2 mM), and trisodium citrate (1 mM) were deaerated with argon and irradiated with a UVB lamp in a flow system with 6.3 m Teflon tubing. The order shown in each panel for residence times corresponds to the sequence of acquisition, ensuring that no systematic order is used (A) in water comparing benzoin (totally inefficient) with α-methylbenzoin, the latter showing intermediate efficiency; (B) benzoin in water showing that at long residence times, there is a slow growth of the plasmon band; (C) spectra in 1:1 CH_3OH: H_2O. Notice that the top absorbance is nearly 30 times larger in panel (C), and further, the highest absorbance is achieved in ~1 min.

4.2.3.4 Concentration tolerance and stability during long fabrication times

We were also interested in establishing to what extent the continuous generation of particles in the flow system would offer consistent results. We were also interested in establishing if AgNP could be produced at higher concentrations, and then diluted just before use. For this work, we chose I-184, one of the highly reliable initiators. The results in Figure 4.9A confirm that a higher concentration of reagents can be readily utilized and dilution to the spectrometer absorbance range shows an excellent well-resolved plasmon band. In the context of continuous production of nanoparticle solutions Figure 4.9B, the 400 nm absorbance shows variations of ±2% over a 6 h period, illustrating the high reliability of the method.

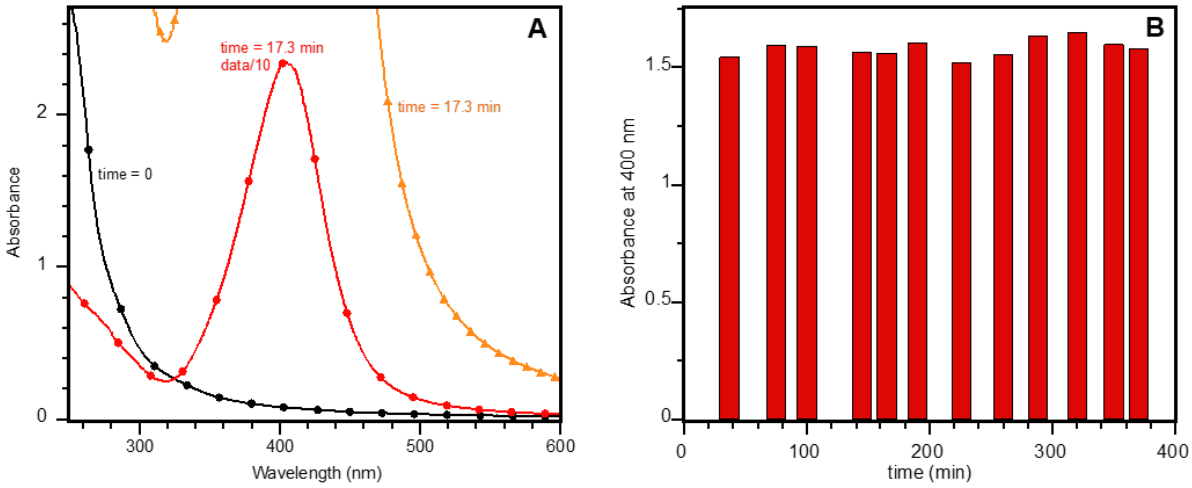

Figure 4.9. Higher concentration and stability during long fabrication times. (A) For our concentration study, we used silver nitrate (2 mM), I-184 (2 mM), and trisodium citrate (10 mM), in MeOH 10% in H_2O deaerated with argon, under UVB irradiation with a residence time of 17.3 min. The absorbance axis has been limited to the 2.7 specification for the Cary 60 spectrometer and the graph includes a sample diluted 10 times. (B) Monitored at 400 nm for over 6 h, with silver nitrate (0.2 mM) and all other parameters identical to panel (A).

4.2.3.5 Characterization of the Nanostructures Prepared

AgNP morphologies for all the initiators were approximately spherical, with D-1173, I-2959, and I-907 producing seeds with the smallest size and narrowest size distributions (Table 4.2). Conversely, I-379 and I-369 yielded the largest seeds with broader size distributions. TEM images (Figure 4.10) and histograms for NPs made with each initiator are available in the Supplementary Materials, see Figures S4.6–S4.13, with corresponding UV–Vis spectra for each sample used for the TEM imaging shown in Figure S4.15.

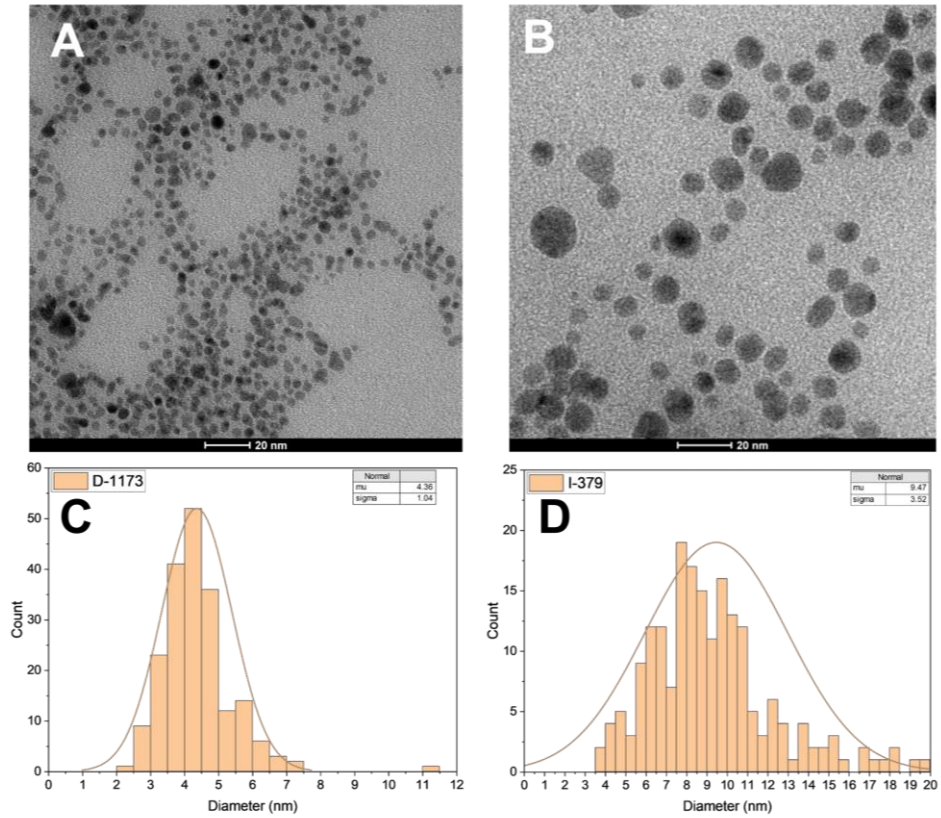

Figure 4.10. TEM image of AgNPs generated with D-1173 (A) and I-379 (B) synthesized in flow using 50% MeOH and their corresponding particle size histograms (C) and (D), respectively. Histograms were made from the counting of 200 particles. XRD for similarly stabilized particles is available in the literature.[20]

Table 4.2. Average diameters and standard deviation of AgNPs synthesized using each photoinitiator with optimized flow conditions. All values are based on the counting of 200 nanoparticles.

Initiator Used	Average Diameter (nm)	Standard Deviation (nm)
I-2959	4.6	1.8
D-1173	4.4	1.0
I-184	7.6	2.6
I-907	5.3	1.5
I-369	8.6	4.2
I-379	9.5	3.5
benzoin	6.1	2.2
α-methylbenzoin	8.3	2.7

4.2.4 Materials and methods

4.2.4.1 Materials and instruments

Chemicals and materials were sourced from multiple suppliers for the experimental work. Ciba Specialty Chemicals supplied the initiators I-184, I-907, I-369, I-379, and D-1173, while Sigma Aldrich provided the benzoin. BASF supplied I-2959, and Alfa Aesar provided alpha-hydroxy-alpha-methylbenzyl phenyl ketone. Solvents were purchased from Fisher chemical.

The UVB lamp (8W) and Expo panel (EXPO-01) were obtained from Luzchem Research, Inc., Ottawa, Canada and Teflon tubing (STT-15) was procured from Component Supply Company, Sparta, TN, USA. The pump (minipuls 3) was purchased from Gilson.

UV–Vis spectroscopy was performed using a Cary 7000 UV–Vis spectrometer for bench reactions and for flow when needed; this instrument can measure high absorbances reliably. A Cary 60 UV–Vis spectrometer was normally used for flow reactions. Transmission electron microscopy (TEM) was performed using an FEI Tecnai G2 spirit Twin TEM microscope.

4.2.4.2 Batch reactions

Batch reactions (without flow) were performed in 20 mL glass vials containing in a typical reaction 0.2 mM $AgNO_3$, 0.2 mM photoinitiator, and 1 mM trisodium citrate dissolved in a 1:1 mixture of MeOH and H_2O. Samples were deoxygenated under gentle argon bubbling for 20 min before being placed in a photoreactor containing 6 UVB lamps for 15 min. Samples were analyzed with UV–Vis spectroscopy and TEM as prepared without any purification.

Similar preparations were also prepared using acetonitrile and ethanol as co-solvents. Notably, without the addition of co-solvent, most photoinitiators were not easily dissolved.

4.2.4.3 Flow reactions

The light sources were 8 W fluorescent lamps from Luzchem installed on an EXPO panel from the same supplier. The Teflon tubing has an outside diameter of 1.80 mm and an inside diameter of 1.50 mm corresponding to a wall thickness of 0.15 mm. We have shown before that this setup leads to an experimental optical path of 0.15 cm.[8]

4.2.5 Conclusions

The photochemical synthesis of silver nanoparticles under flow conditions has proven extremely efficient and reproducible, yielding suitable AgNP seeds under UVB irradiation with exposure times of less than one minute for the best initiators. The recommended initiators are those yielding ketyl radicals efficiently following Norrish Type I cleavage. Among the eight structures shown in Scheme 4.3, four of them are highly recommended, I-184, D-1173, $\boldsymbol{\alpha}$-methylbenzoin, and I-2959. The last of which shows the best absorption properties, adequate aqueous solubility, and is readily available. We anticipate that the seeds produced here will enable the synthesis of other morphologies with interesting biological applications.[13,21]

4.3 Post-print version of supplementary information

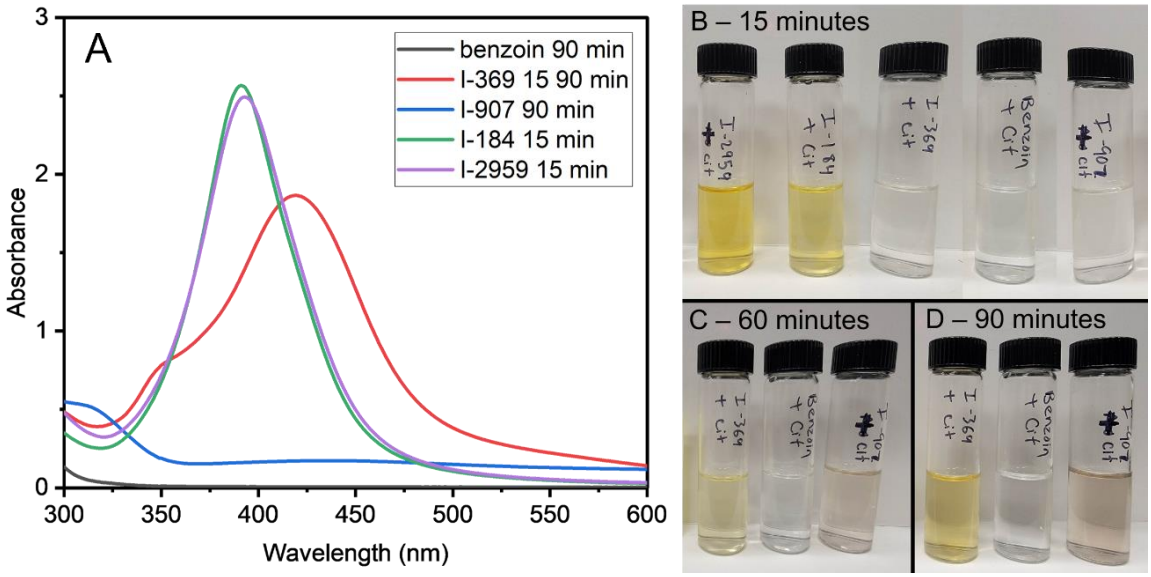

Figure S 4.1. A) UV-Vis spectra of AgNP solutions produced using 0.2 mM I-2959, I-184, I-369, benzoin, or I-907 as photoinitiators in H_2O. I-2959 and I-184 completed the reaction in 15 minutes, while I-369 required 90 minutes to generate similar levels of AgNP absorbance. Benzoin and I-907 did not yield any notable plasmonic absorbance peaks within 90 minutes of the reaction. The corresponding appearance of the nanoparticle suspensions at 15 minutes (B), 60 minutes (C), and 90 minutes (D) are shown in the right panel. It should be noted that I-2959 dissolved easily.

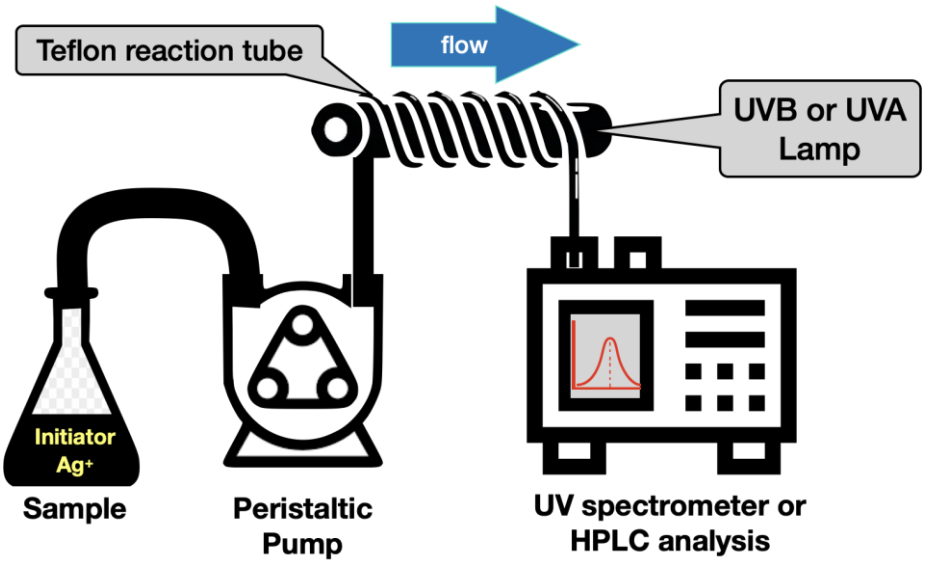

Figure S 4.2. Schematic representation of the experimental flow system.

Figure S 4.3. The appearance of solutions containing 0.2 mM $AgNO_3$, 1 mM citrate, and 0.2 mM of either I-2959 (“A”) and I-184 (“E”) as initiators, in mixtures of MeCN and H_2O (0%, 25%, 50%, 75% and 100% MeCN) following 15 minutes of irradiation with in a photoreactor with 6, 8W UVA lamps (for the 0% MeCN samples). The samples containing MeCN showed no change after 15 minutes. The MeCN containing samples were subsequently irradiated for a total of 90 min but still did not yield any AgNPs.

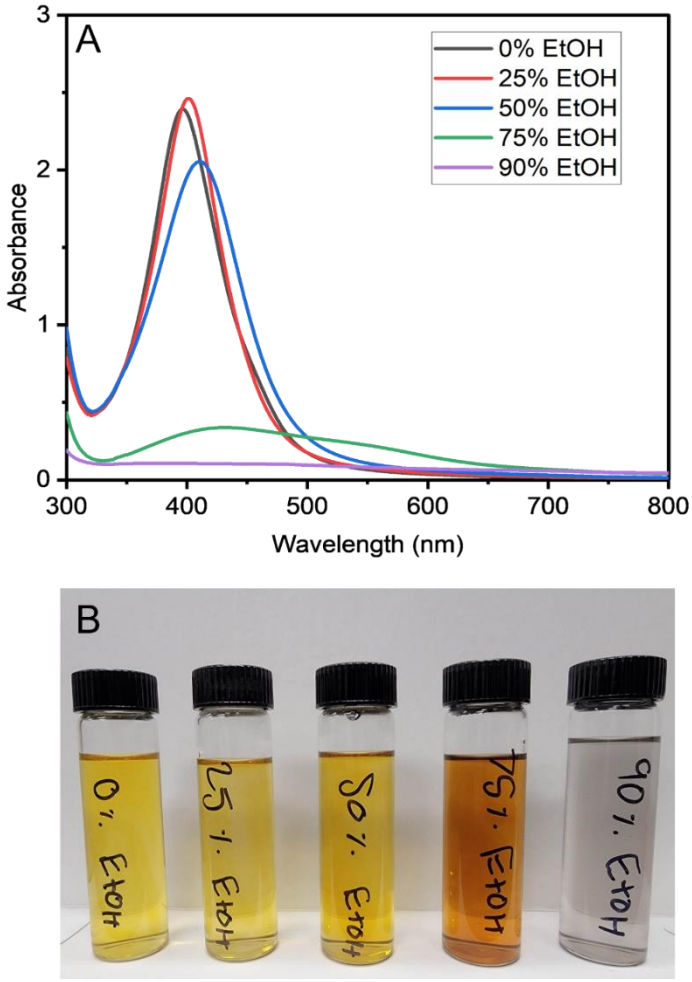

Figure S 4.4. A) UV-Vis spectra of AgNPs synthesized in batch scale, using 0.2 mM I-2959 as an initiator. Solutions were prepared in mixtures of EtOH: H_2O in ratios ranging from 0 to 90% EtOH and irradiated for 15 minutes in a photoreactor with 6, 8W UVB lamps. The 90% EtOH sample was irradiated for an additional 25 mins, as little color could be seen after 15 minutes of irradiation. B) Corresponding appearance of AgNPs produced in solutions containing different fractions of EtOH following reacting under UVB.

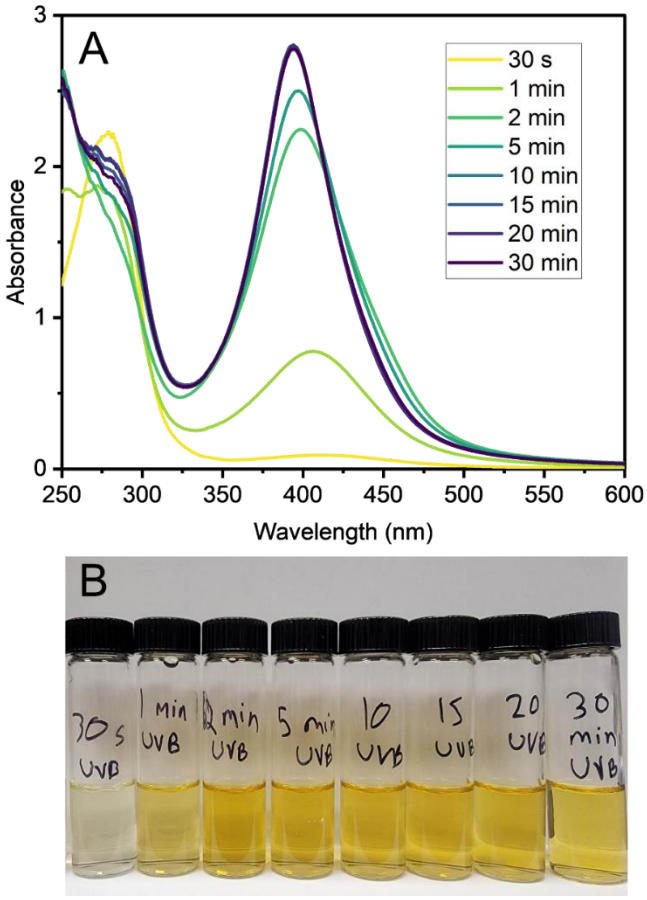

Figure S 4.5. A) UV-Vis spectra of AgNPs synthesized in single batches, using 0.2 mM I-2959 in H_2O. Samples were irradiated in a photoreactor with 6 UVB lamps for 30 sec to 30 min to determine the endpoint of the reaction. B) The appearance of the corresponding nanoparticle suspensions.

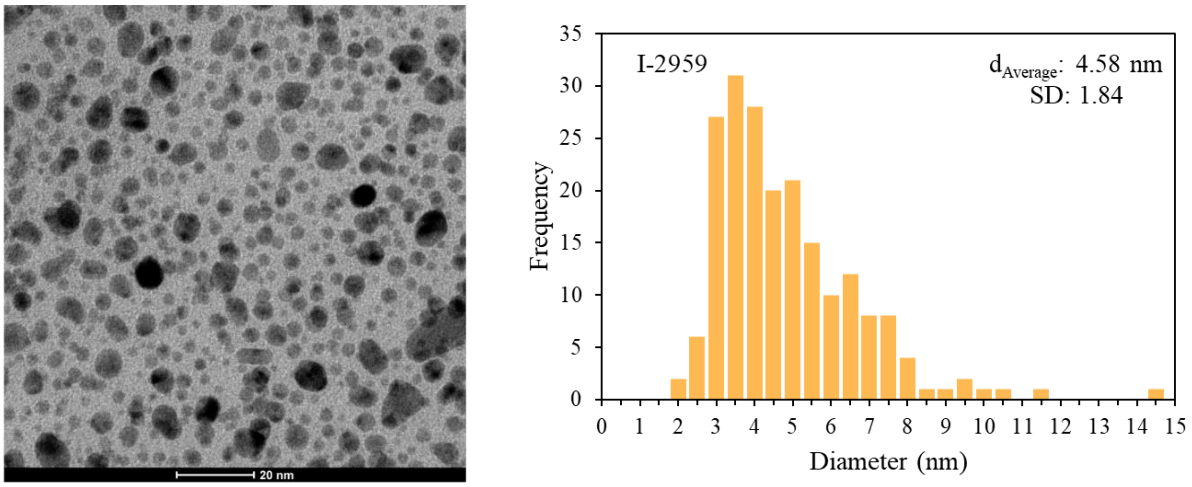

Figure S 4.6. Left: Representative TEM image of AgNPs generated using the optimized flow reaction conditions using I-2959 as a photoinitiator. Right: Corresponding histogram for I-2959 generated AgNPs, n = 200 particles. Inset lists average size, nm, and standard deviation, sigma, in nm.

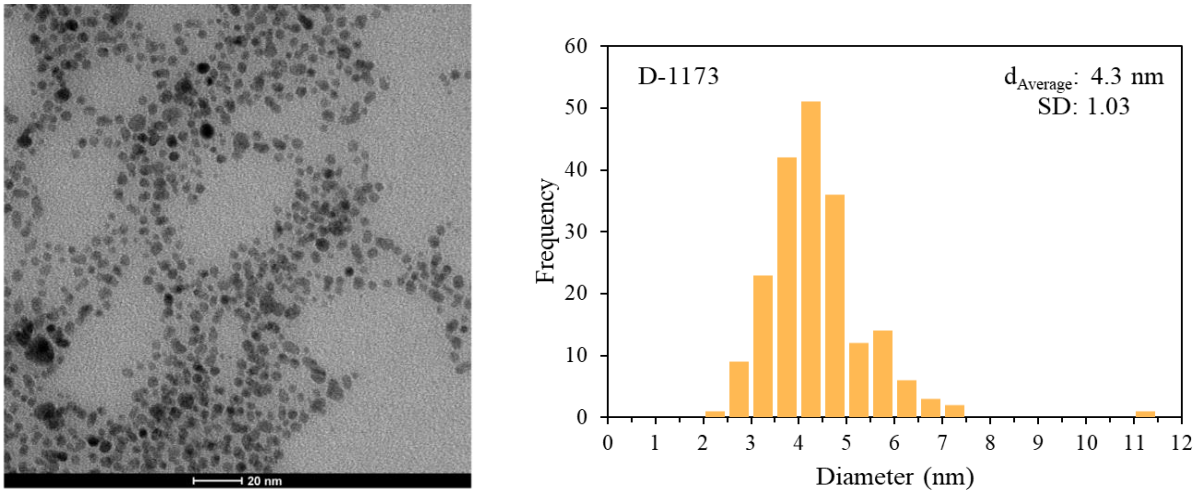

Figure S 4.7. Left: Representative TEM image of AgNPs generated using the optimized flow reaction conditions using D-1173 as a photoinitiator. Right: Corresponding histogram for D-1173 generated AgNPs, n = 200 particles. Inset lists average size, nm, and standard deviation, sigma, in nm.

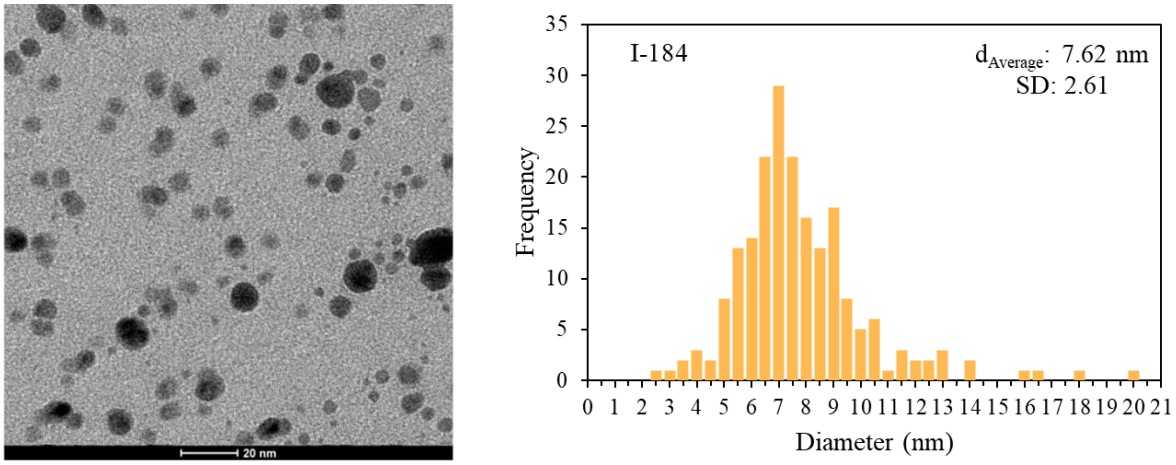

Figure S 4.8. Left: Representative TEM image of AgNPs generated using the optimized flow reaction conditions using I-184 as a photoinitiator. Right: Corresponding histogram for I-184 generated AgNPs, n = 200 particles. Inset lists average size, nm, and standard deviation, sigma, in nm.

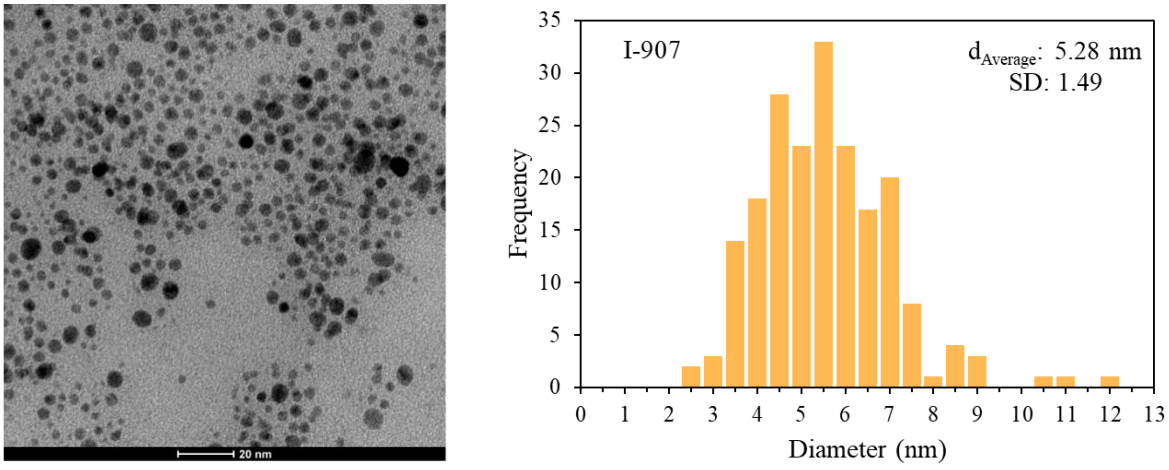

Figure S 4.9. Left: Representative TEM image of AgNPs generated using the optimized flow reaction conditions using I-907 as a photoinitiator. Right: Corresponding histogram for I-907 generated AgNPs, n = 200 particles. Inset lists average size, nm, and standard deviation, sigma, in nm.

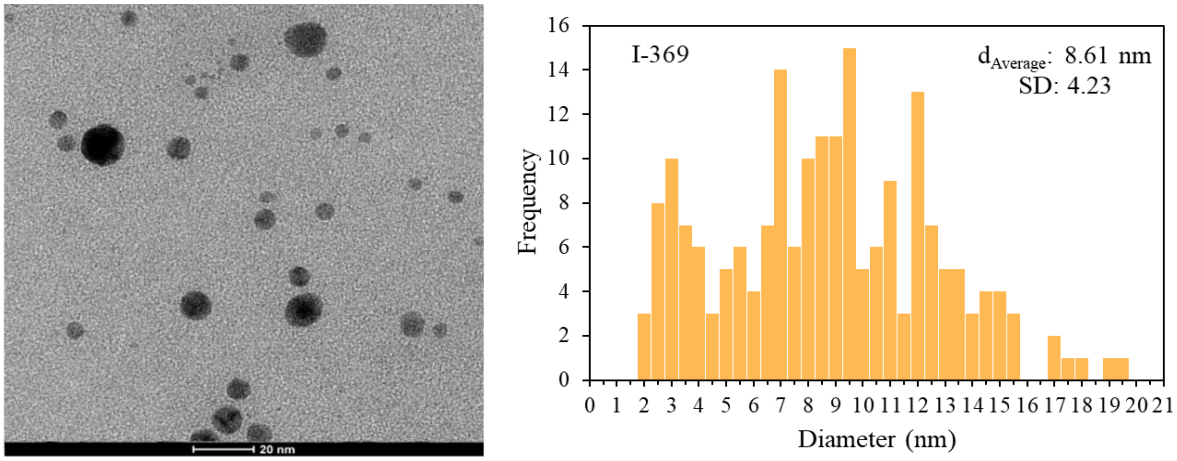

Figure S 4.10. Left: Representative TEM image of AgNPs generated using the optimized flow reaction conditions using I-369 as a photoinitiator. Right: Corresponding histogram for I-369 generated AgNPs, n = 200 particles. Inset lists average size, nm, and standard deviation, sigma, in nm.

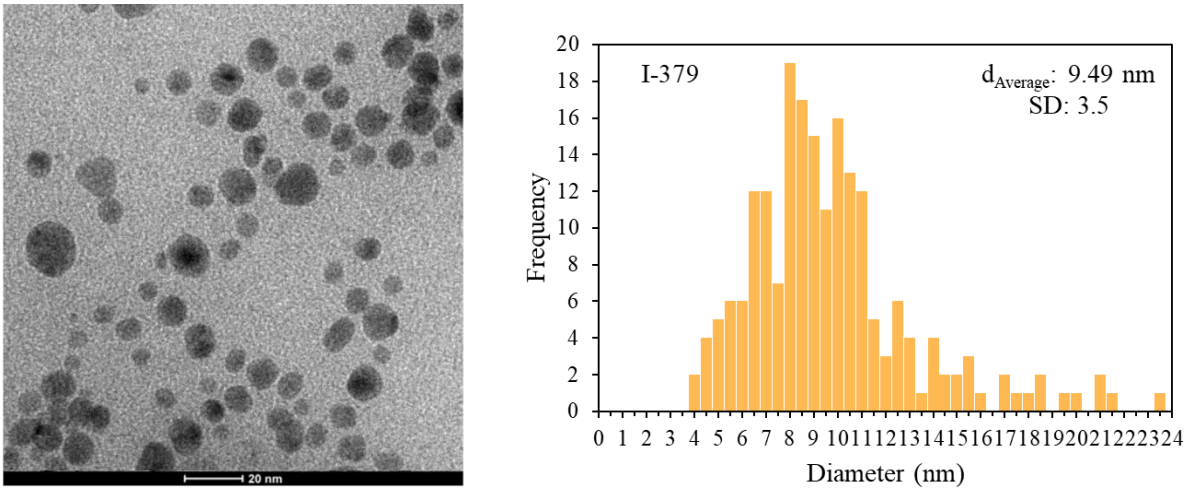

Figure S 4.11. Left: Representative TEM image of AgNPs generated using the optimized flow reaction conditions using I-379 as a photoinitiator. Right: Corresponding histogram for I-379 generated AgNPs, n = 200 particles. Inset lists average size, nm, and standard deviation, sigma, in nm.

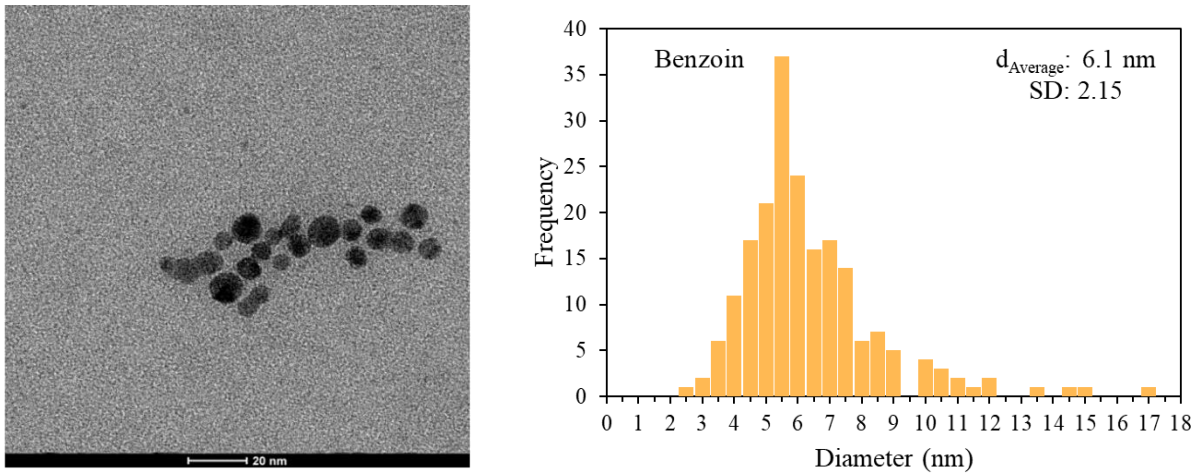

Figure S 4.12. Left: Representative TEM image of AgNPs generated using the optimized flow reaction conditions using benzoin as a photoinitiator. Right: Corresponding histogram for benzoin generated AgNPs, n = 200 particles. Inset lists average size, nm, and standard deviation, sigma, in nm.

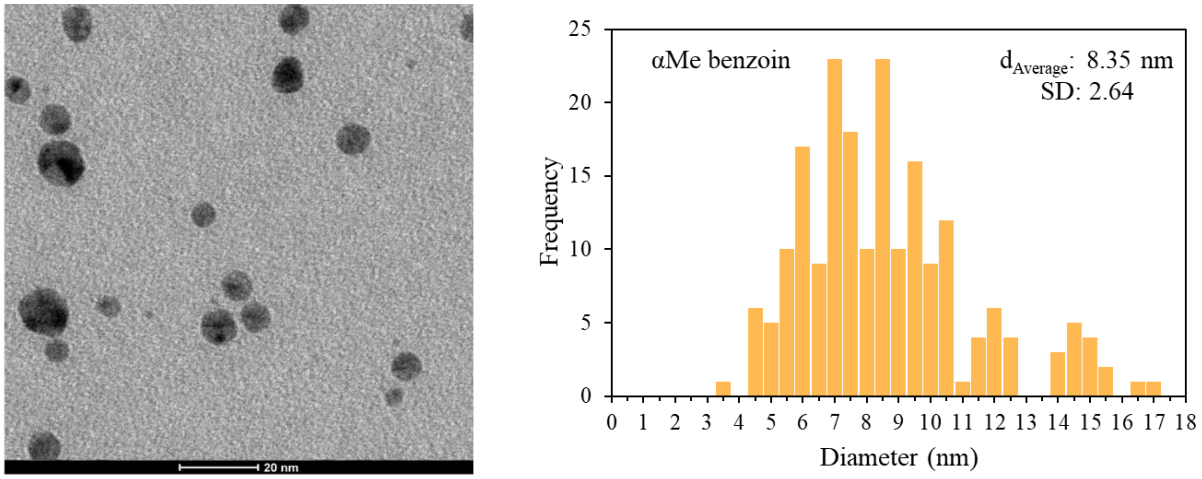

Figure S 4.13. Left: Representative TEM image of AgNPs generated using the optimized flow reaction conditions using α-methylbenzoin as a photoinitiator. Right: Corresponding histogram for α-methylbenzoin generated AgNPs, n = 200 particles. Inset lists average size, nm, and standard deviation, sigma, in nm.

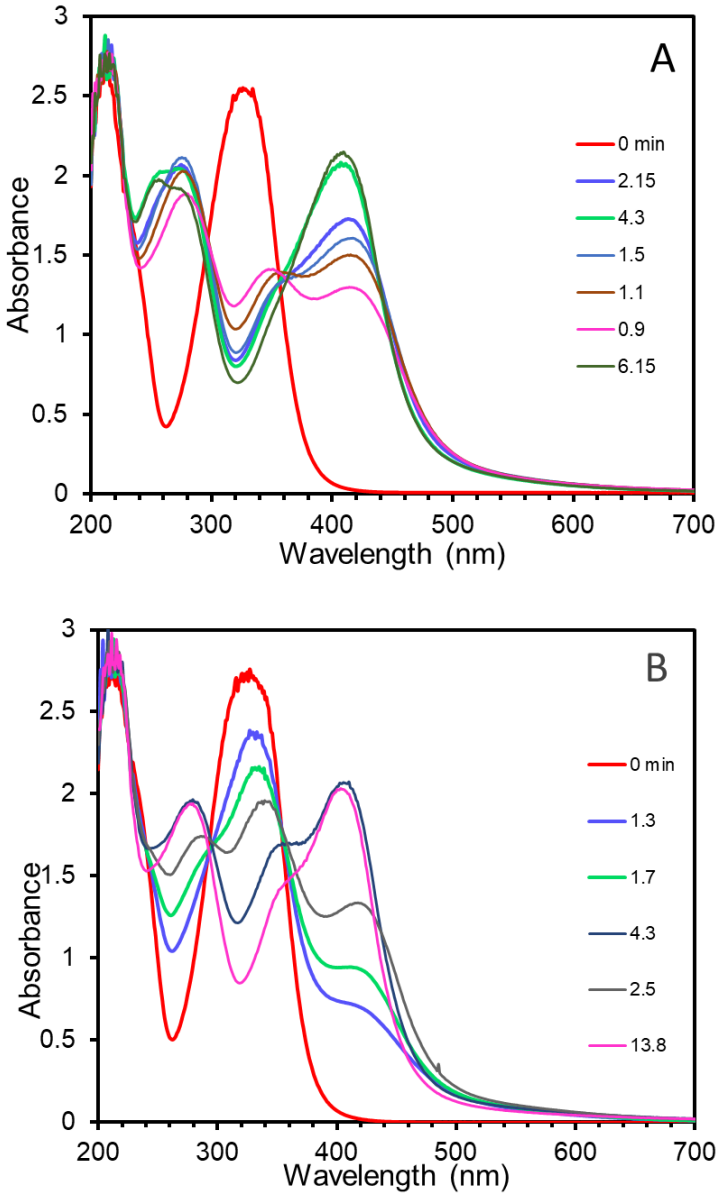

Figure S 4.14. I-369 as an initiator for spectra corresponding to different residence times in minutes. Silver nitrate (0.2 mM), benzoin (0.2 mM), and trisodium citrate (1 mM) in 1:1 CH_3OH: H_2O deaerated with argon and irradiated in a flow system with 6.3 m Teflon tubing with (A) UV-B lamp and (B) UV-A lamp.

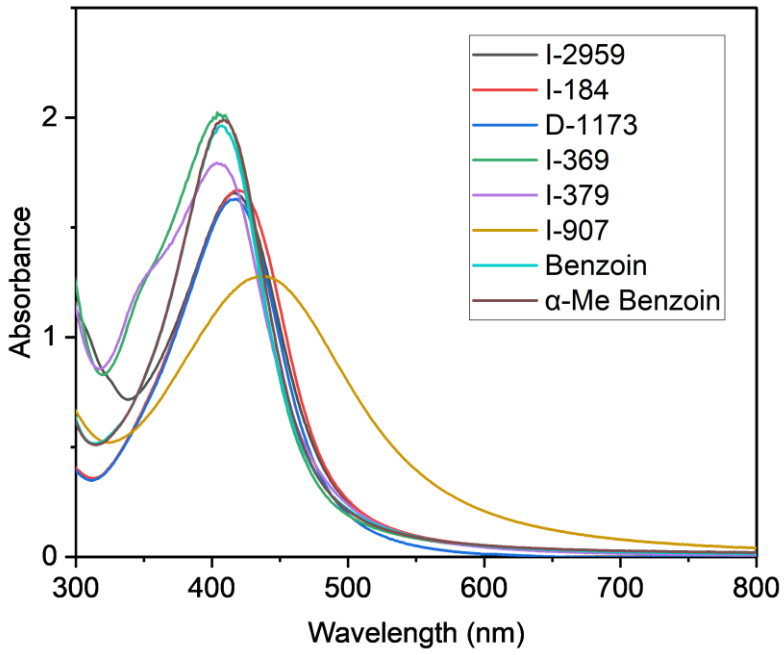

Figure S 4.15. UV-Vis spectra of AgNPs made in-flow using 50% MeOH, 1 mM citrate, 0.2 mM $AgNO_3$, and 0.2 mM of photoinitiator under UVB irradiation. Flow rates for each are shown in Table 4.1. Corresponding TEM and histograms are shown in Figure S4.6-S4.13.

4.4 Accompaniment to Chapter

The photochemical synthesis of silver nanoparticles (AgNPs) under flow conditions has proven highly efficient and reproducible. Using UVB irradiation and photoinitiators that yield ketyl radicals through Norrish Type I cleavage, we achieved AgNP seed formation in less than one minute. The most effective initiator demonstrated optimal absorption properties, good aqueous solubility, and ready availability.

These AgNP seeds serve as versatile precursors for nanoparticles with diverse morphologies, opening possibilities for tailored biological applications. Building on this success, our research group is now exploring how altering the light source within the same system can produce AgNPs of different shapes and sizes, such as triangular and decahedral structures.

This morphological control is crucial as it directly influences the optical and biological properties of the nanoparticles. The flow-based photochemical approach offers advantages over

traditional batch methods, including improved parameter control, enhanced reproducibility, and potential for continuous production.

The next phase of this research, led by our colleague Carly Frank, investigates how different light source characteristics influence the morphology of shape-controlled silver nanoparticles (AgNPs). This work not only refines the method for synthesizing AgNP seeds but also establishes a foundation for precise control over nanoparticle shapes. These advancements have significant potential for applications in nanomedicine and environmental remediation. The result of this study is submitted to the Nanoscale Advances journal.

4.5 References

(1) Scaiano, J. C.; Stamplecoskie, K. G.; Hallett-Tapley, G. L. Photochemical Norrish Type I Reaction as a Tool for Metal Nanoparticle Synthesis: Importance of Proton Coupled Electron Transfer. *Chem. Commun.* **2012**, *48* (40), 4798–4808. https://doi.org/10.1039/C2CC30615H.

(2) Lipson, M.; Turro, N. J. Picosecond Investigation of the Effect of Solvent on the Photochemistry of Benzoin. *J. Photochem. Photobiol. Chem.* **1996**, *99* (2), 93–96. https://doi.org/10.1016/S1010-6030(96)04399-7.

(3) Jockusch, S.; Landis, M. S.; Freiermuth, B.; Turro, N. J. Photochemistry and Photophysics of α-Hydroxy Ketones. *Macromolecules* **2001**, *34* (6), 1619–1626. https://doi.org/10.1021/ma001836p.

(4) Esen, D. S.; Arsu, N.; Da Silva, J. P.; Jockusch, S.; Turro, N. J. Benzoin Type Photoinitiator for Free Radical Polymerization. *J. Polym. Sci. Part Polym. Chem.* **2013**, *51* (8), 1865–1871. https://doi.org/10.1002/pola.26569.

(5) McGilvray, K. L.; Decan, M. R.; Wang, D.; Scaiano, J. C. Facile Photochemical Synthesis of Unprotected Aqueous Gold Nanoparticles. *J. Am. Chem. Soc.* **2006**, *128* (50), 15980–15981. https://doi.org/10.1021/ja066522h.

(6) Marin, M. L.; McGilvray, K. L.; Scaiano, J. C. Photochemical Strategies for the Synthesis of Gold Nanoparticles from Au(III) and Au(I) Using Photoinduced Free Radical Generation. *J. Am. Chem. Soc.* **2008**, *130* (49), 16572–16584. https://doi.org/10.1021/ja803490n.

(7) Scaiano, J. C.; Billone, P.; Gonzalez, C. M.; Marett, L.; Marin, M. L.; McGilvray, K. L.; Yuan, N. Photochemical Routes to Silver and Gold Nanoparticles. *Pure Appl. Chem.* **2009**, *81* (4), 635–647. https://doi.org/10.1351/PAC-CON-08-09-11.

(8) Yaghmaei, M.; Scaiano, J. C. A Simple Norrish Type II Actinometer for Flow Photoreactions. *Photochem. Photobiol. Sci.* **2023**, *22* (8), 1865–1874. https://doi.org/10.1007/s43630-023-00417-1.

(9) Miranda, O. R.; Ahmadi, T. S. Effects of Intensity and Energy of CW UV Light on the Growth of Gold Nanorods. *J. Phys. Chem. B* **2005**, *109* (33), 15724–15734. https://doi.org/10.1021/jp0514832.

(10) Stamplecoskie, K. G.; Scaiano, J. C. Kinetics of the Formation of Silver Dimers: Early Stages in the Formation of Silver Nanoparticles. *J. Am. Chem. Soc.* **2011**, *133* (11), 3913–3920. https://doi.org/10.1021/ja108451v.

(11) Cambié, D.; Bottecchia, C.; Straathof, N. J. W.; Hessel, V.; Noël, T. Applications of Continuous-Flow Photochemistry in Organic Synthesis, Material Science, and H2O Treatment. *Chem. Rev.* **2016**, *116* (17), 10276–10341. https://doi.org/10.1021/acs.chemrev.5b00707.

(12) Rehm, T. H. Flow Photochemistry as a Tool in Organic Synthesis. *Chem. – Eur. J.* **2020**, *26* (71), 16952–16974. https://doi.org/10.1002/chem.202000381.

(13) Stamplecoskie, K. G.; Scaiano, J. C. Light Emitting Diode Irradiation Can Control the Morphology and Optical Properties of Silver Nanoparticles. *J. Am. Chem. Soc.* **2010**, *132* (6), 1825–1827. https://doi.org/10.1021/ja910010b.

(14) Jiang, X. C.; Chen, C. Y.; Chen, W. M.; Yu, A. B. Role of Citric Acid in the Formation of Silver Nanoplates through a Synergistic Reduction Approach. *Langmuir* **2010**, *26* (6), 4400–4408. https://doi.org/10.1021/la903470f.

(15) Turkevich, J.; Stevenson, P. C.; Hillier, J. A Study of the Nucleation and Growth Processes in the Synthesis of Colloidal Gold. *Discuss. Faraday Soc.* **1951**, *11* (0), 55–75. https://doi.org/10.1039/DF9511100055.

(16) Cruickshank, F. R.; Benson, S. W. Carbon-Hydrogen Bond Dissociation Energy in Methanol. *J. Phys. Chem.* **1969**, *73* (3), 733–737. https://doi.org/10.1021/j100723a041.

(17) Belloni, J. The role of silver clusters in photography. *Comptes Rendus Phys.* **2002**, *3* (3), 381–390. https://doi.org/10.1016/S1631-0705(02)01321-X.

(18) Yaghmaei, M.; Bourgonje, C. R.; Scaiano, J. C. Facile Scale-Up of the Flow Synthesis of Silver Nanostructures Based on Norrish Type I Photoinitiators. *Molecules* **2023**, *28* (11), 4445. https://doi.org/10.3390/molecules28114445.

(19) Lewis, F. D.; Lauterbach, R. T.; Heine, H. G.; Hartmann, W.; Rudolph, H. Photochemical .Alpha. Cleavage of Benzoin Derivatives. Polar Transition States for Free-Radical Formation. *J. Am. Chem. Soc.* **1975**, *97* (6), 1519–1525. https://doi.org/10.1021/ja00839a041.

(20) Mahy, J. G.; Kiendrebeogo, M.; Farcy, A.; Drogui, P. Enhanced Decomposition of H2O2 Using Metallic Silver Nanoparticles under UV/Visible Light for the Removal of p-Nitrophenol from H2O. *Catalysts* **2023**, *13* (5), 842. https://doi.org/10.3390/catal13050842.

(21) Bourgonje, C. R.; Silva, D. R. C. da; McIlroy, E.; Calvert, N. D.; Shuhendler, A. J.; Scaiano, J. C. Silver Nanoparticles with Exceptional Near-Infrared Absorbance for Photoenhanced Antimicrobial Applications. *J. Mater. Chem. B* **2023**, *11* (26), 6114–6122. https://doi.org/10.1039/D3TB00199G.

Chapter 5. Photosensitised selective semi-oxidation of tetrahydroisoquinoline: A singlet oxygen path

5.1 Preamble to Chapter

The conception of this research originated during Iris Martin's visit to the Scaiano group in 2018. The initial objective of the project was to elucidate the oxidation mechanism of tetrahydroisoquinoline (THIQ) using heterogeneous catalysts under visible light. Over time, several students contributed to the foundational experiments at various stages. Following the successful completion of my initial project on the reduction of nitro compounds to amines using Pd@GW (palladium on glass wool), Prof. Scaiano assigned me to further investigate this study, specifically focusing on detecting traces of hydrogen peroxide as evidence to support the proposed reaction mechanism.

As I embarked on this project, I began by replicating the catalyst (MoCo@GW - molybdenum complex on glass wool) using the same methods as in previous studies. My initial goal was to repeat the experiments under identical conditions, employing strip detectors to identify hydrogen peroxide. Despite numerous attempts, I couldn't definitively detect hydrogen peroxide. However, this led me to closely monitor the reaction kinetics. After running several experiments, I obtained three significant results:

The reagent conversion exhibited an inflection point, which was our first intriguing finding. We began to think about potential factors that could accelerate the reaction after a specific retention time.

The second noteworthy result emerged when I experimented without a catalyst. By patiently tracking the reaction kinetics, I discovered that the reaction could proceed catalyst-free, albeit with a longer reaction time but showed the same inflection point.

This observation led us to explore the possibility of an autocatalytic mechanism. After months of trial and error, I decided to change the solvent to improve oxygen solubility. This third discovery provided a critical clue: the lifetime of singlet oxygen plays a crucial role in the

reaction. This realization shifted the focus of our study entirely, leading to extensive work with Laser Flash Photolysis (LFP) and a deeper investigation into quenching plots.

The disclosure that singlet oxygen reactivity drives selectivity dramatically shifted our research trajectory. This unexpected shift led to some earlier experiments remaining unpublished, though they were no less valuable to our understanding.

Acknowledgments are extended to all contributors involved in the initial stages of this research project. Their efforts laid the groundwork for subsequent investigations. It should be noted, however, that the experimental results presented in this chapter were exclusively conducted by me under the direct supervision of Prof. Tito Scaiano and with the guidance of Dr. Anabel Lanterna. Their combined mentorship and expertise were instrumental in shaping the methodological approach and interpreting the resultant data.

5.2 Post-print version of the manuscript

First published in Photochemical & Photobiological Sciences. 2022;21(8):1473-9

This chapter has been adapted from Photochemical & Photobiological Sciences journal with permission as the author of this article.

5.2.1 Abstract

Selective semi-oxidation of tetrahydroisoquinoline (THIQ) leads to a valuable dihydroisoquinoline (DHIQ) derivative via the singlet oxygen photooxidation process. In contrast to DHIQ, THIQ acts as an efficient singlet oxygen quencher driving reaction selectivity. Typical photosensitisers (i.e., Ru complexes) can activate the reaction even under heterogeneous conditions that facilitate catalyst separation and reusability. The reaction can also be facilitated by semiconductor catalysts such as MoCo@GW, a glass wool-based catalyst that is easy to separate and reuse and compatible with flow photochemistry. Its role is to mediate the formation of isoquinoline (IQ) and thus an in situ-generated singlet oxygen catalyst. Laser flash photolysis with NIR detection provides proof of the singlet oxygen mechanism proposed and rate constants for the key steps that mediate oxidation.

5.2.2 Introduction

Reactions that involve partial hydrogenation or de-hydrogenation present selectivity challenges due to catalytic processes that tend to proceed to completion; for example, we recently reported on the reduction of alkynes, where it is easy to proceed completely to the alkane, but difficult to stop "halfway" at the alkene.[1,2] In the case of oxidations, a similar characteristic is common, for example, the overoxidation of 1,2,3,4-tetrahydroisoquinoline (THIQ) to yield isoquinoline (IQ) is common, while stopping at the semi-oxidation product – dihydroquinoline (DHIQ) is challenging and requires highly selective catalysts. This is reflected in commercial pricing, where DHIQ is 150 times more expensive than THIQ and 250 times more expensive than IQ on the scale of 100 g.[3] The possibility of carrying out these selective transformations with reusable catalysts and utilizing molecular oxygen constitutes a preferred sustainable pathway. Badu-Tawiah et al. have recently reported on the photocatalytic aerobic dehydrogenation of tetrahydroquinolines (THQ) and THIQ derivatives.[4] While they recognize THIQ oxidation is frequently incomplete, they attribute this unusual reactivity to the hyperconjugation of the molecule and use N-substituted derivatives to achieve full oxidation. Contrasting reports suggest the formation of singlet oxygen under photocatalytic conditions can be either detrimental[5] or essential[6] when considering aerobic oxidation of N-substituted THIQ to their corresponding isoquinoline derivatives. In this work, we show singlet oxygen is essential for the dehydrogenation of THIQ, and the oxidation process is stalled until minimal concentrations of IQ are generated in situ during the reaction, driving selectivity toward the semi-oxidation product DHIQ.

Oxidation of THIQ with visible light showed an induction delay before the reaction started. Using different solvents with different oxygen solubility affected the reaction delay time, and experiments with deuterated methanols with various singlet oxygen lifetimes suggested the involvement of singlet oxygen in this reaction. Further experiments with laser flash photolysis were a confirmation on the main role of singlet oxygen in THIQ oxidation.

The mechanistic studies shown here test a recently introduced photocatalyst based on glass wool as an inexpensive, widely available catalyst support that with adequate surface modification can provide physical or chemical affinity towards numerous catalytic materials.[7,8] In this research heterogeneous and homogeneous catalysts were used. For heterogeneous a newly

designed molybdenum disulfide-cobalt semi-conductor catalyst (MoCo@GW) and a modified $Ru(bpy)_3Cl_2$ (RuB@GW), both supported on glass wool, were selected and as a homogeneous catalyst commercial $Ru(bpy)_3Cl_2$ were added to the reaction mixture. Remarkably, these catalysts allow for selective photooxidation to dihydroisoquinoline (DHIQ), avoiding common overoxidation to isoquinoline (IQ), under oxygen atmosphere, room temperature, and visible light irradiation.

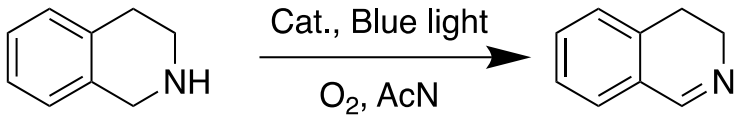

Scheme 5.1. Selective oxidation of THIQ to DHIQ catalysed by supported MoCo@GW, RuB@GWor soluble $Ru(bpy)_3Cl_2$. When no catalyst is added the reaction shows a prolonged induction period until the catalyst is generated in situ.

The reaction was performed under blue light excitation (wavelength centred at ~450 nm) and an oxygen atmosphere. For catalytic experiments, 50 mg of the heterogeneous catalyst was used. Kinetic studies show a long induction period for the reaction to start; for example, under an irradiance of ≤ 6 Wcm^{-2}, it takes as long as 90 minutes to achieve the first 10% conversion, followed by a dramatic acceleration of the partial oxidation to DHIQ. Given the high value-added of DHIQ, we decided to undertake a mechanistic study of this semi-oxidation step and the parameters that control the rate, initial delay, and selectivity of the process. Our studies show that MoCo@GW can perform single electron transfer (SET) reactions (even if inefficiently) that can get the oxidation started and eventually produce enough IQ that can accelerate the reaction through efficient singlet oxygen mechanisms. While alternative direct photosensitization to generate singlet oxygen (e.g., with soluble $Ru(bpy)_3Cl_2$) allows a delay-free oxidation process, the use of MoCo@GW has the advantage of being readily removable from the reaction media and is also potentially compatible with flow photocatalysis.

We combine catalyst characterization and bench studies with laser flash photolysis under various conditions, including near-infrared detection. This approach provides valuable kinetic information, revealing the role of singlet oxygen in the later stages of the reaction and offering insights that help reduce or eliminate the initial reaction delay.

5.2.3 Experimental

Please see the Supporting Information part for additional information on experimental conditions, sources of materials and spectroscopic and analytical conditions.

5.2.3.1 Conditions of irradiation

The standard conditions for the reaction involved 67 mg of THIQ (0.125 M) in 4 mL of acetonitrile, irradiated with ≤ 6 Wcm^{-2} of LED light centered at ~450 nm (LEDi, Luzchem LED Illuminator with FWHM 23 nm) under O_2 atmosphere with air cooled samples maintained at ~23 °C. A detailed spectroscopic analysis of this light source reveals that it contains 0.02% of light below 400 nm.

5.2.3.2 Laser flash photolysis and NIR detection

The laser flash photolysis experiments were performed using a Surelite Nd-YAG laser 355 nm (~10-20 mJ/pulse) in a customized LFP-111 laser-flash photolysis (LFP) system (Luzchem Inc., Ottawa, Canada) and 1×1 cm^2 or 0.7 x 0.7 cm^2 LFP cuvettes from Luzchem. Samples had an absorbance of ~0.3 at the laser wavelength.

Time-resolved singlet oxygen luminescence measurements were conducted using the same laser system as above and were detected at right angles using a Hamamatsu photomultiplier tube sensitive in the near IR. The signal was captured and digitized using a Tektronix 2440 transient digitizer part of the customized Luzchem laser flash photolysis system. Singlet oxygen measurements were made at 1270 nm, where singlet oxygen has an emission spectrum peak, with samples having absorbances at 355 nm in the range of 0.1 - 0.4.

5.2.3.3 Synthesis and characterization of MoCo@GW catalyst

Initial requirements for the active species attachment have implied the activation of the non-silanized glass wool with a source of amino-groups given by (3-aminopropyl)-triethoxysilane (APTES) treatment. The catalyst was then synthesized by treating glass wool with 3.5 %wt of Mo and a 5.4 %wt Co load. Metallic species were grafted (chemisorption) to the APTES@GW fibers using a photochemical method. Briefly, proper amounts of Mo and Co precursors were mixed with the photoinitiator Irgacure 907 (I-907) in a flask using acetonitrile as

a reaction solvent. This initiator can undergo Norrish type I cleavage upon UVA excitation generating radical species that can reduce the metal cations, also improving the attachment of cobalt oxide (CoOx) nanoparticles to the Mo layered matrix. Mo and Co proportions were determined by ICP-OES analysis (Table S5.1). Additionally, through comparisons with only Mo (Mo@GW) and only Co (Co@GW), control catalysts, we found that a mix of both Mo and Co (MoCo@GW) is more efficient than their single metal catalysts. This is the synergistic effect of Co and Mo, as has also been reported by others.[9] Scanning electron microscopy (SEM) allowed us to observe the particles and a similar distribution of Mo and Co determined by EDS analyses on fibers; images of the complete fibers show that cobalt centers are located in the same area as the molybdenum structures (Figure S5.1). The oxidation states of Mo 3d and Co 2p were determined by X-ray photoelectron spectroscopy (XPS), with a mixture of Mo^{4+}, Mo^{6+} and Co^{2+} being observed (Figure S5.2).

5.2.4 Results and Discussion

5.2.4.1 Experiments without catalyst

The selective oxidation of THIQ was studied under different conditions. In the absence of any catalyst, the THIQ solution in acetonitrile is stable under dark conditions. The system also shows minimal changes for at least two hours under visible light (λ= 450 nm) irradiation. Prolonged irradiation leads to small conversions to DHIQ (10 % after 370 min), after which the reaction accelerates and reaches a conversion rate of 0.51% per minute near the inflection point, see Figure 5.1. The reaction reaches 90% selectivity towards DHIQ [i.e.,100 x DHIQ/(DHIQ + IQ)] at 50% conversion and remains at 82% selectivity at 98.5% conversion. The drastic acceleration of the reaction shown in Figure 5.1 suggests a slow in situ formation of efficient catalytic species within the reaction, which were further analyzed by LFP. Notably, the reaction performs poorly in air and does not proceed under an inert atmosphere (Figure S5.3).

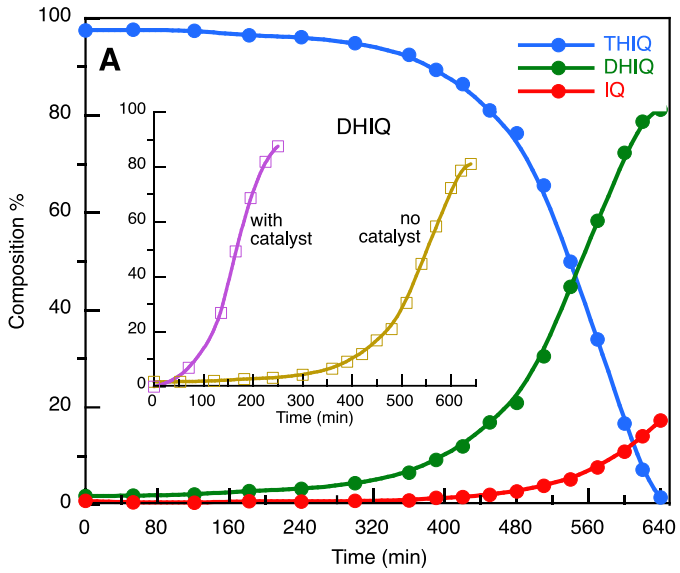

Figure 5.1. Evolution of the semi-oxidation of THIQ (0.125 M) in acetonitrile under blue LEDi (~450 nm) irradiation and O_2 atmosphere in the absence of the catalyst. Inset, a comparison of DHIQ formation when the catalyst is MoCo@GW.

Close analysis of the reaction evolution experiments indicates that the maximum conversion rate, as measured at the inflection point in the THIQ curve, coincided with the presence of a small (≤2%) formation of IQ. To better understand the role of IQ in the selective oxidation of THIQ, we performed a series of experiments introducing small quantities of IQ at different reaction times (Figure S5.4). The addition of 4 %mol equivalents of IQ at the start of the reaction reduced the initial delay (to 10% conversion) from 370 to 210 minutes. The effect of the addition of 4 %mol DIQ was less than the IQ addition. Further, adding 0.5 mL of a completed reaction to a 4 mL fresh THIQ sample reduced the delay to 35 minutes, doubling the conversion rate (figure S5.4).

Another way to test the effect of pre-irradiation is to add THIQ when the reaction is almost completed as illustrated in Figure 5.2, where THIQ was added after 600 minutes. Notice that no delay is detectable after the addition of THIQ, suggesting that the solution was “ready” to proceed with the photocatalytic process.

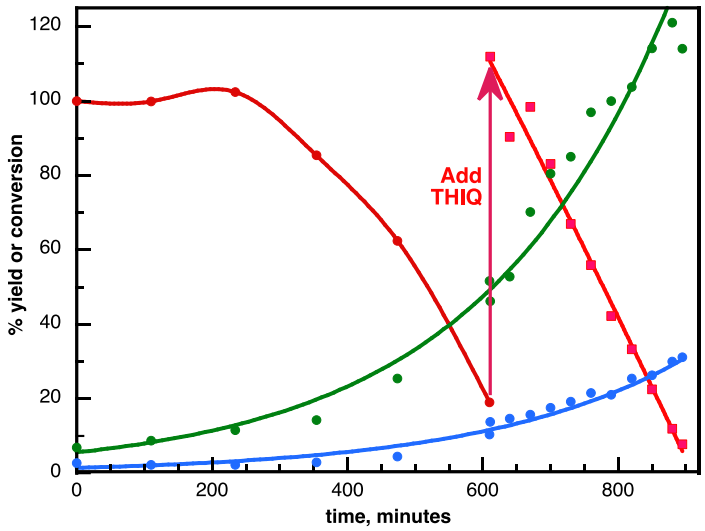

Figure 5.2. THIQ oxidation reaction evolution over time under conditions described in Figure 1, followed by the addition of THIQ (to reach 0.125 M) at 611 minutes. Notice that after the addition of THIQ = red, DHIQ = green and IQ = blue follow a smooth growth curve, while consumption of THIQ occurs without delay. Selectivity was 79% after 900 minutes.

5.2.4.2 Solvent effects

The reaction conditions shown in Figure 5.1 were used to test different solvents, namely acetonitrile (AcN), hexane (Hx), and methanol (MeOH). The solvents were selected based on their different oxygen solubility (Hx > AcN > MeOH) and polarity (Hx < AcN < MeOH).[10] Figure 5.3 shows that methanol is the least efficient solvent because of the long initial delay and the low rate of THIQ consumption, effectively almost 5 times slower than in acetonitrile. This led us to suspect that singlet oxygen could be mediating the late stages (post-initial delay) of the oxidation of THIQ. To test this possibility, we substituted methanol for CD_3OD, as deuteration is known to enhance dramatically the lifetime of singlet oxygen.[11] As illustrated in Figure 5.3, CD_3OD causes a significant acceleration of the overall process, as expected for singlet oxygen reactions, reflecting that THIQ reactions will be favoured if the lifetime of singlet oxygen is enhanced.[11] The effect for CH_3OD (not shown) is minor, reflecting a minor $^1O_2$ lifetime enhancement.

As a further test of the singlet oxygen hypothesis, we added NaN_3 to the system, as N_3^- is a well-known singlet oxygen scavenger.[12] This led to a small slow-down of the reaction (Figure

S5.7). The usual extensive effect of azide is probably attenuated by the fact that THIQ is itself an excellent singlet oxygen scavenger. On the other hand, adding $Ru(bpy)_3Cl_2$ as a singlet oxygen sensitizer to the THIQ showed a reaction without any delay Figure S5.5.

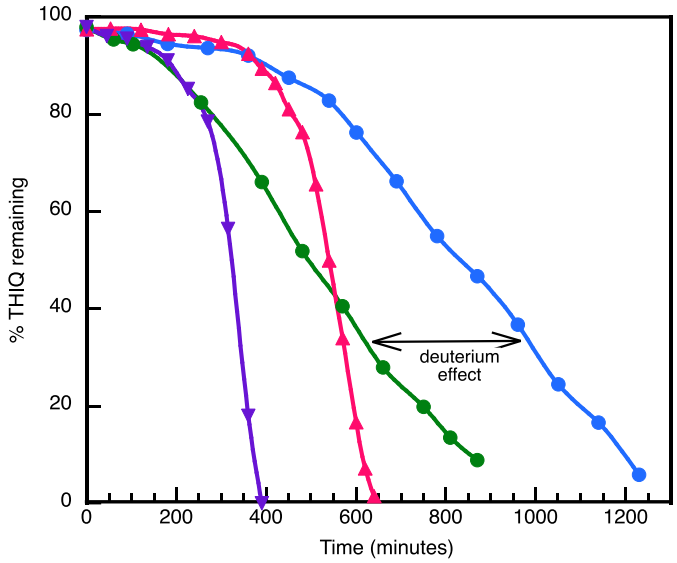

Figure 5.3. Consumption of THIQ as a function of time in various solvents: purple triangles = hexane, pink triangles = acetonitrile, blue circles = methanol and green circles = methanol-d_4. Note that methanol-d_4 accelerates the reaction by ~ 360 minutes.

5.2.4.3 Mechanistic studies

As the next step, we decided to examine the possible role of singlet oxygen making its generation independent of the THIQ system. For this purpose, we used $Ru(bpy)_3Cl_2$ as a commercially available sensitizer, using 355 nm laser pulses for excitation and monitoring the emission from singlet oxygen in acetonitrile at 1270 nm. The lifetime in the absence of quencher was ~80 μs (τ_0), which is consistent with literature reports for singlet oxygen in acetonitrile.[13,14] The lifetimes were reduced in the presence of THIQ, as illustrated in the inset in Figure 5.4. A plot of the rate constant for decay (k_d) as a function of the THIQ concentration (equation 1) leads to a quenching rate constant of 2.63 x 10^7 $M^{-1}s^{-1}$.

$$k_d = \tau^{-1} = \tau_0^{-1} + k_q [THIQ] \qquad (1)$$

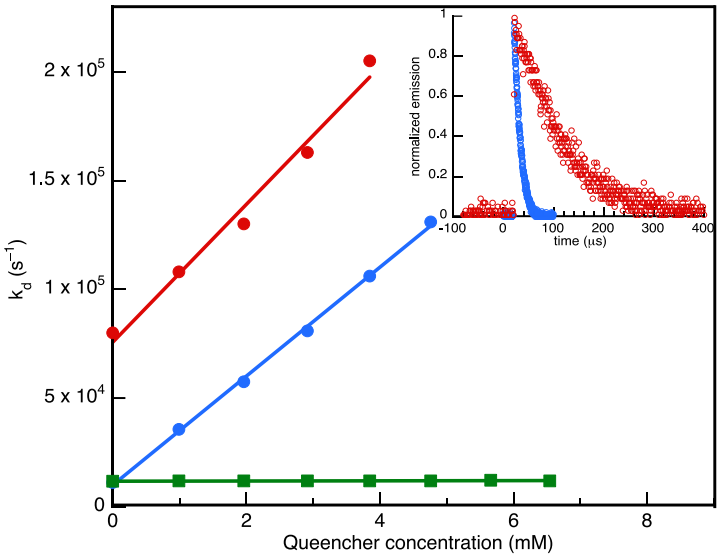

Figure 5.4. Quenching plots for singlet oxygen in acetonitrile. Blue and red points for THIQ as a quencher with $Ru(bpy)_3Cl_2$ and IQ as sensitizers, respectively. Green points are for DHIQ as a quencher, with $Ru(bpy)_3Cl_2$ as a sensitizer. No significant quenching is observed for DHIQ. Inset: decay traces for singlet oxygen emission (monitored at 1270 nm) in the absence (red) and presence of 2.9 mM THIQ (blue). For long lifetimes (red data) it is necessary to attenuate the signal to obtain more reliable lifetimes.

As discussed before, the presence of IQ can accelerate the oxidation of THIQ (Figure 5.2). To understand this apparent in situ catalytic effect, we explored the potential formation of singlet oxygen using IQ as a sensitiser. The experiment needed to be performed at a rather high IQ concentration that led to a reduction of singlet oxygen lifetimes; however, the identification of the emitter was unequivocal and the rate constant for THIQ quenching was the same as in $Ru(bpy)_3Cl_2$ experiments. What is more, similar $Ru(bpy)_3Cl_2$ experiments with DHIQ as a quencher revealed that singlet oxygen quenching by DHIQ is at least 1000 times slower than by THIQ (Figure 5.4), an observation that is key to the high discrimination towards selective oxidation observed in our work.

5.2.4.4 Heterogeneous Catalysts

We tried several catalysts to test the oxidation dynamics without affecting the selectivity. While the experiments above show that singlet oxygen generators can greatly enhance the kinetics of THIQ to DHIQ conversion with minimal loss of selectivity, it would be desirable to

avoid soluble catalysts that add steps to the post-reaction separation and purification processes. For this purpose, we tested if the ruthenium catalysis could be performed by a heterogeneous catalyst also capable of generation of singlet oxygen but being amenable for easy removal after use. We have previously developed glass-grafted ruthenium catalysts, among them the $[Ru(bpy)_2dppa](PF_6)_2$ loaded onto glass wool (RuB@GW).[8] As shown in Figure 5.5A, irradiation of RuB@GW confirmed the conversion of THIQ to DHIQ without an extended initial delay, in a reasonable time (that could be adjusted with light intensity) and with excellent selectivity.

The same reaction conditions were assayed in the presence of 50 mg of MoCo@GW and the initial delay was shortened to ~80 min for 10% conversion and the rate at the inflection point increased to 0.82% per minute. At 90% conversion (225 min) the selectivity was still 90%, Figure 5.5B. As a control experiment for using a bimetallic catalyst, we prepared Mo@GW, Co@GW, and APTES@GW and ran the experiment with the same conditions (Figure S5.6). The results confirmed the synergistic effect between Mo and Co in improving the catalytic role in oxidation reactions.[15,16]

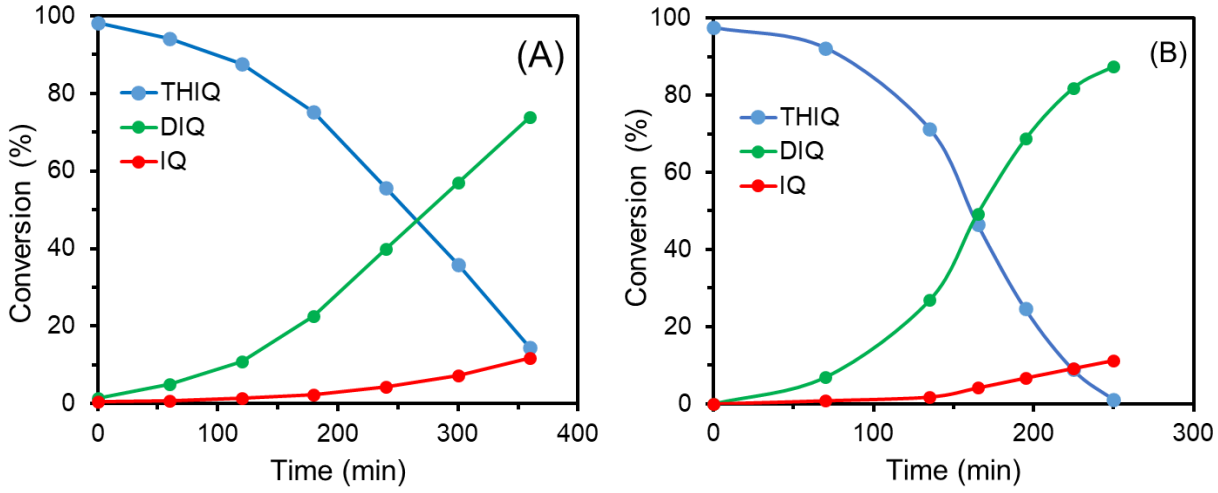

Figure 5.5. THIQ oxidation reaction evolution over time under visible light irradiation in the presence of (A) RuB@GW and (B) MoCo@GW. Conditions: THIQ (0.125 M) in acetonitrile, O_2 atmosphere, light $\lambda = 450$ nm (≤ 6 W cm^{-2}). THIQ in blue, DHIQ in green and IQ in red.

5.2.4.5 Mechanistic analysis

There are two aspects to the oxidative generation of DHIQ from THIQ. One is straightforward and is the singlet oxygen-mediated oxidation. With a quenching rate constant of 2.6×10^7 $M^{-1}s^{-1}$, THIQ is a favoured target for singlet oxygen reaction. Further, the fact that DHIQ is a poor singlet oxygen target, with its reaction at least 1000 times slower than for THIQ is the cause of the high selectivity that helps the oxidation to stop "halfway" rather than proceed to IQ.

The second aspect is the initiation of the process in the absence of added singlet oxygen sensitizers. Since in all cases, singlet oxygen is the dominant reaction mechanism, the cases with no sensitiser added, or with MoCo@GW as a pre-catalyst require a route for the in-situ generation of a singlet oxygen sensitizer, with the simplest explanation (and confirmed by chromatographic analysis) is the formation of IQ. For the non-catalyst system, nearly 6-hour delay under strong irradiation is required to form a minimum amount of IQ. It is hard to identify a source, although it is hardly surprising that some oxidation takes place, noting also that once some IQ is generated it can support further oxidation. In addition, as much as 0.7% IQ may be present in the initial reaction mix.

The presence of MoCo@GW greatly reduces the delay. We propose that the formation of IQ in this case is also mediated by DHIQ which is an excellent target for hydroperoxyl radical HOO• (given the presence of benzylic hydrogens),[17] with DHIQ formed by the mechanisms of Scheme 5.2.

The complexity of Scheme 5.2 is entirely related to the need to add or generate in situ a good singlet oxygen sensitizer; once this has been achieved the singlet oxygen oxidation takes over and ensures excellent selectivity towards DHIQ. In fact, the mechanism of Scheme 5.2, which enables the initial formation of IQ, would not be anticipated to provide the selectivity towards DHIQ that is at the centre of this report.

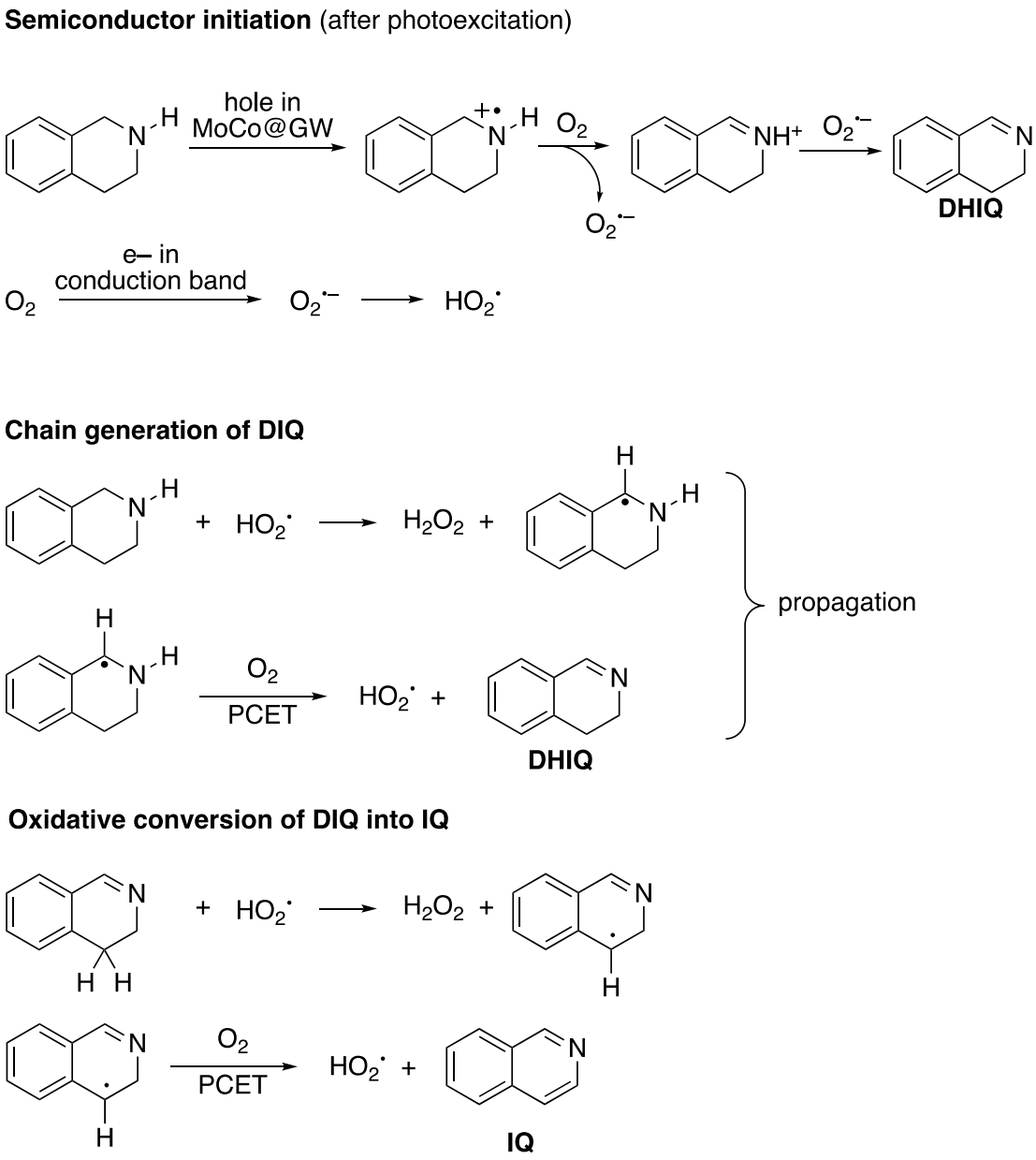

Scheme 5.2. Semiconductor-based mechanisms for the formation of DHIQ, a precursor for IQ under semiconductor-mediated oxidation.

5.2.5 Conclusions

For the series THIQ. DHIQ and IQ, the most valuable one is DHIQ, largely reflecting that both for catalytic oxidations and reductions, stopping “halfway” is difficult. Catalysts that utilize molecular oxygen are highly desirable as they enable sustainable pathways, more so if they are heterogeneous catalysts, easy to recover and suitable or adaptable flow chemistry.

In the case of THIQ the dramatic difference in reactivity towards singlet oxygen between THIQ and DHIQ (≤1000) enables exceptional selectivity and the ability to stop "halfway" in the oxidative process.

5.3 Post-print version of supplementary information

5.3.1 Materials and instruments

Most of the compounds for doing experiments such as 1,2,3,4-tetrahydroisoquinoline, 3,4-dihydroisoquinoline, isoquinoline, (3-aminopropyl)triethoxysilane, methanol-d_4, and cobalt (II) chloride hexahydrate were purchased from Sigma Aldrich. Ammonium tetrathiomolybdate, 99.95% from Alfa Aesar and solvents were from Fisher chemical. UVA lamp 8W (LZC-UVA), blue LEDi 450 nm (LEDi-HBL) and Expo panel (EXPO-01) were from Luzchem Research, Inc.

The oxidation states of metals on glass wool were characterized by X-ray Photoelectron spectroscopy. XPS was performed on a Kratos analytical model Axis Ultra DLD, using monochromatic aluminum Ka X-rays at 140 W. XPS data were analyzed using CasaXPS software, Version 2.1.01. ICP experiments were performed using an Agilent Vista Pro ICP Emission Spectrometer and Scanning electron microscopy (SEM) and Energy dispersive X-ray spectroscopy (EDX) were performed in the JEOL JSM-1600 SE microscope. All results were analysed by GC-MS analyses from Agilent 6890-N Gas Chromatograph with an Agilent 5973 mass selective detector.

5.3.2 Catalyst preparation

5.3.2.1 Glass wool pre-treatment

A mass of 1 g of non-treated glass wool was placed in a round bottom flask and immersed in a 250 mL solution of 1% concentration of APTES in toluene. The mixture was refluxed overnight at 110°C to allow monolayer coverage. After that, a cooling down to room temperature the mixture was allowed under constant stirring for 6 additional hours. The filtering process was done by washing the mixture with toluene (3x100 mL) and acetone (3x100 mL) then dried in the oven at 100°C overnight before metal decoration.[7]

5.3.2.2 Synthesis of MoCo@GW

Molybdenum and Cobalt supported on GW were prepared by photo deposition of $CoCl_2$ and $(NH_4)_4MoS_4$ onto the APTES-treated GW. In brief, 9.6 mg of $(NH_4)_4MoS_4$ (3.5 wt% Mo), 21.8 mg of $CoCl_2.6H_2O$ (5.4 wt% Co), and 18.4 mg of I-907 (photo-initiator) were suspended in 10 mL of acetonitrile (AcN). The mixture was sonicated for 10 minutes, then added to 100 mg APTES@GW in a glass vial then purged with Argon for 10 minutes. The sealed glass vial was irradiated with a Luzchem Expo panel fitted with 5 UVA bulbs (8W each) for 5 h and rotated on a hot-dog cooker for homogeneous mixing. The dark grey fibers obtained were filtered and washed with AcN to remove non-bonded species and left to dry in the oven overnight. The resulting grey fibers were characterized by SEM, EDS, ICP, and XPS.

Similar procedures were followed for the synthesis of Mo@GW and Co@GW, using the corresponding metal precursor.

5.3.2.3 Synthesis of Mn@GW

MnO_2 supported on GW was prepared by reducing the reaction of permanganate. 10 mg of $KMnO_4$ were dissolved in 10 mL of milli-Q water. 300 mg of APTES@GW were soaked in 10 mL of ethanol in a Pyrex petri dish and the $KMnO_4$ solution was added. The mixture was kept in the dark and at room temperature for 3 h, then washed with ethanol and water to remove the non-bonded residual of MnO_2.

5.3.2.4 Synthesis of RuB@GW

The synthesis of this material has been described in the literature.[8]

5.3.3 Catalyst characterization

The catalysts were characterized by Inductively Coupled Plasma Optical Emission Spectroscopy (ICP-OES), Scanning Electron Microscopy (SEM), and X-ray Photoelectron spectroscopy (XPS).

5.3.3.1 ICP-OES analysis

Metal loading on freshly prepared MoCo@GW, Mo@GW, Co@GW, Mn@GW, and RuB@GW catalysts was determined by ICP-OES. Sample replicates of 20 mg of catalysts were accurately weighed, digested with aqua regia, and then diluted. The samples were measured and

quantified by using the emission line of the corresponding elements (284.824 nm (Mo), 238.892 nm (Co), 267.876 nm (Ru), and 257.610 nm (Mn)). Table S5.1 shows the average results of ICP-OES for these samples.

Table S 5.1. Metal loading was determined by ICP-OES analysis.

Catalyst	**Mass (metal/ GW+ metal) ×100 (wt%)**
MoCo@GW	0.146 (Mo)
	0.260 (Co)
Mo@GW	0.120
Co@GW	0.486
RuB@GW	0.002
Mn@GW	0.300

5.3.3.2 SEM analysis

Scanning electron microscopy analysis of the fresh and used MoCo@GW and Mn@GW were performed. SEM imaging and EDX analyses (Figure S5.1) show that the surface of the glass fiber is covered with metal particles (or clusters). After using MoCo@GW as a catalyst the amount of Mo and Co decreased significantly but when MnO2 was added as a co-catalyst to the solution, some particles of Co stayed on the glass wool.

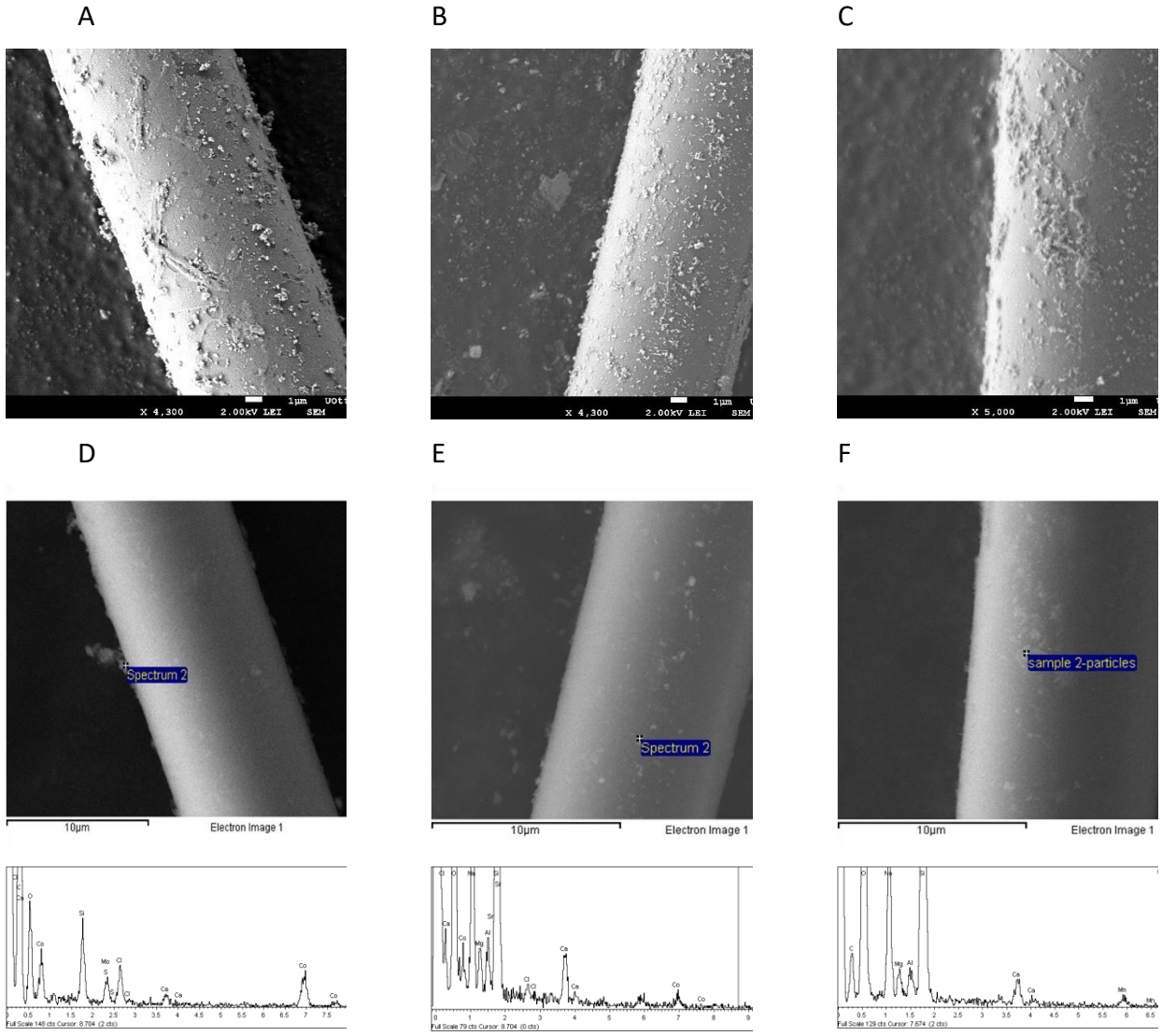

Figure S 5.1. SEM images of catalysts
(A) fresh MoCo@GW, (B) used MoCo@GW in the presence of MnO_2, and (C) fresh Mn@GW. EDX spectra for the corresponding region shown of (D) fresh MoCo@GW, (E) used MoCo@GW in the presence of MnO_2, and (F) fresh Mn@GW. Scale bar = 1 μm. Fibers are about 10 μm in diameter.

5.3.3.3 XPS analysis

XPS deconvolution analyses were performed for MoCo@GW to determine the oxidation state of Mo and Co. Characteristic peaks for Mo 3d were proved MoS_2 and MoS_3 in our catalyst. These peaks were fitted using the spin-orbit split constituted by Mo^{4+} 3d5/2 (229.1 eV), Mo^{4+} 3d3/2 (232.1 eV), Mo^{6+} 3d5/2 (231.8 eV), and Mo^{6+} 3d3/2 (235 eV) separated by 3.2 eV. Peaks of $Mo^{\delta+}$ 3d5/2 (227.7 eV) and $Mo^{\delta+}$ 3d3/2 (230.7 eV) ($0 < \delta < 4$). A single peak at 226.6 eV was attributed to S^{2-} 2s which is an overlapping part of Mo 3d peaks. S is from Mo precursor $(NH_4)_4MoS_4$ in MoCo@GW.[18,19]

The XPS fitting for the Co 2p in MoCo@GW reveals the presence of two oxidation states. Co^{3+} 2p3/2 (779 eV) and Co^{3+} 2p1/2 (794 eV) are separated by 14.99 eV and Co^{2+} 2p3/2 (781.2 eV) and Co^{2+} 2p1/2 (796.5 eV) followed by Co^{2+} 2p satellite peaks at (786 eV and 802.6 eV) is confirmation in presence of Co oxides.[20]

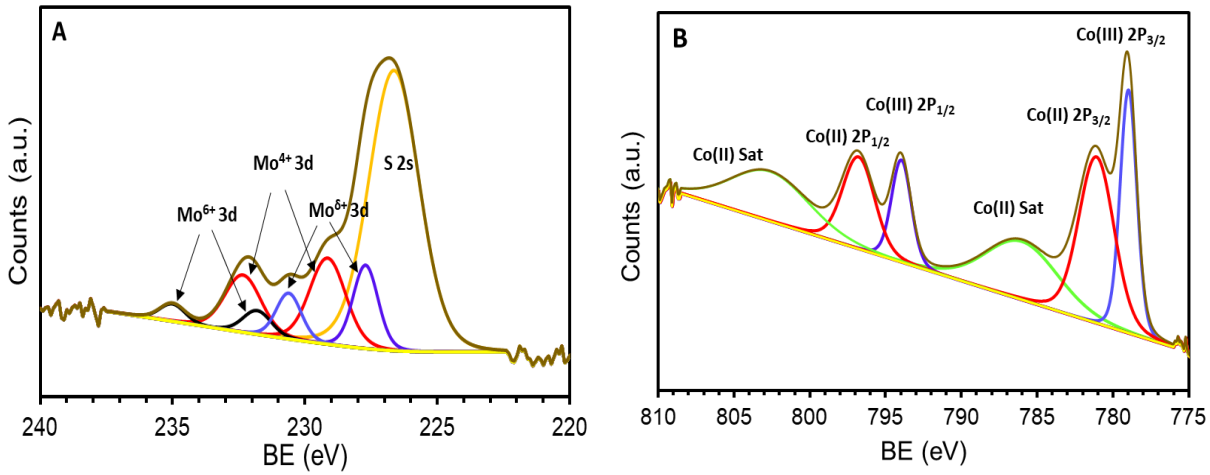

Figure S 5.2. Deconvoluted HR-XPS spectrum of MoCo@GW (A) Mo 3d, (B) Co 2P

5.3.4 Photosensitized semi-oxidation of THIQ

This section provides conversion selectivity graphs for a variety of experimental conditions beyond those illustrated in graphs in the main text. These conditions supplement and provide additional support for the examples in the main text.

5.3.4.1 Reaction conditions

Typical experiments involve 67 mg of THIQ (0.125 M) in 4 mL of acetonitrile and visible light irradiation (LED: λmax = 450 nm, FWHM = 23 nm, irradiance ≤ 6 Wcm^{-2}) under an O_2 atmosphere. An air cooling system was used to maintain the reaction temperature at about ~23 °C. A detailed spectroscopic analysis of this light source reveals a 0.02% content of light below 400 nm.

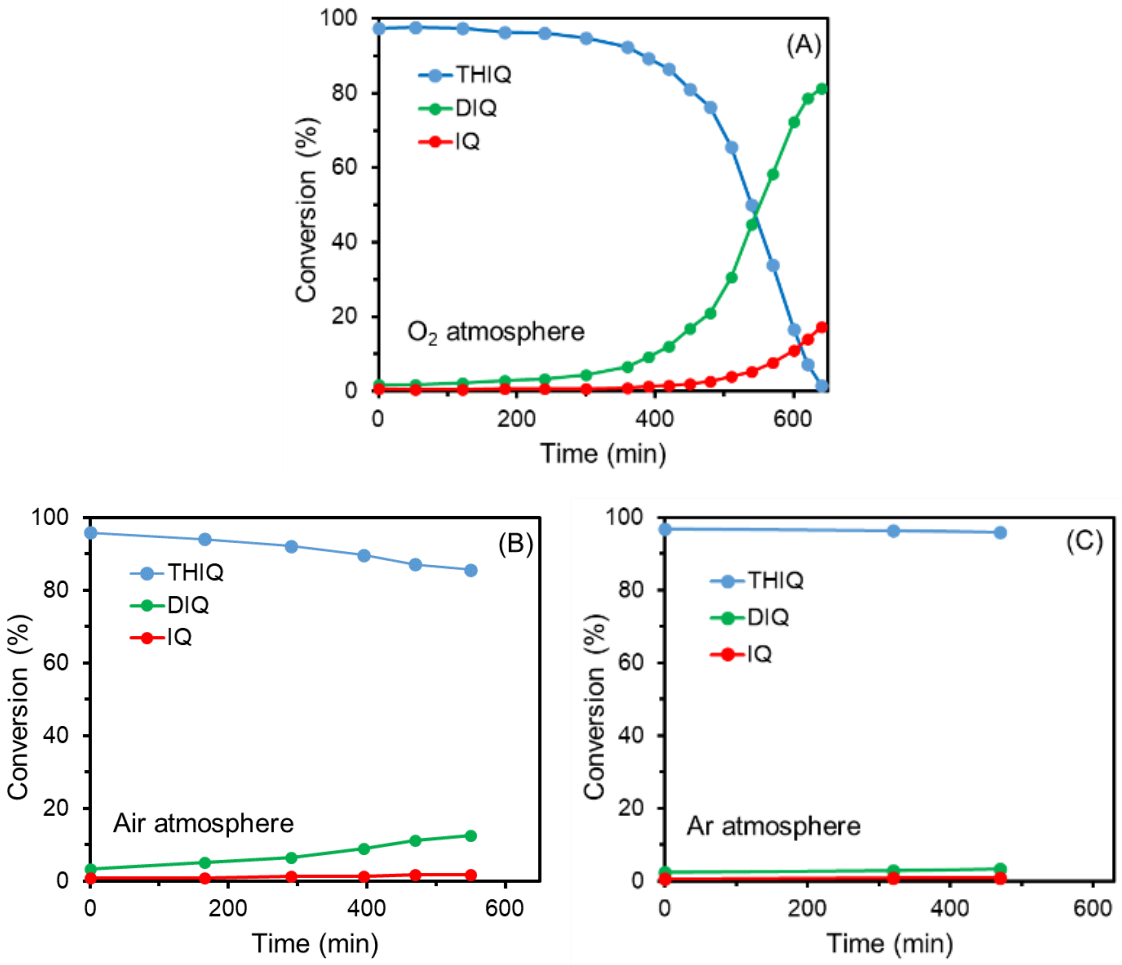

Figure S 5.3. Effect of oxygen concentration
Semi-oxidation of THIQ (0.125 M) in AcN (in the absence of photosensitisers) irradiated with blue LEDi under different atmospheres: (A) oxygen, (B) air, and (C) argon. Samples were analysed by GC-MS using tert-Butylbenzene as an external standard.

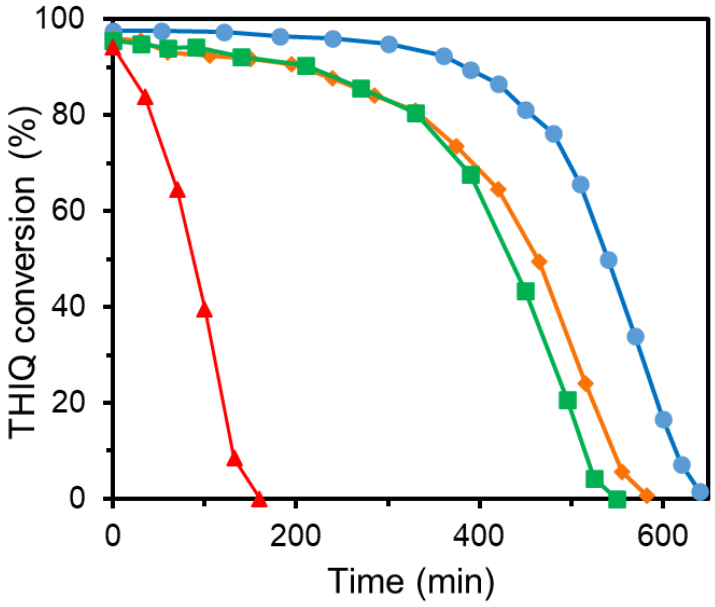

Figure S 5.4. Effect of adding IQ and DHIQ in the oxidation of THIQ
THIQ (0.125 M) in 4 ml AcN, O_2 atmosphere, irradiated with blue LEDi. Samples were analysed by GC-MS using tert-butylbenzene as an external standard. GC-MS results of experiments with different additives. In parenthesis, composition at time = 0.
(Blue circle) without added IQ. (THIQ 97.51%, DHIQ 1.82%, IQ 0.77%)
(Green square) with 4 %mol of commercial IQ (THIQ 95.45%, DHIQ 1.12%, IQ 3.43%)
(Orange diamond) with 4 %mol of commercial DHIQ (THIQ 95.94%, DHIQ 3.90%, IQ 0.16%)
(Red triangle) with 0.5ml of completed reaction IQ and DHIQ (THIQ 94.11%, DHIQ 4.18%, IQ 1.7%)

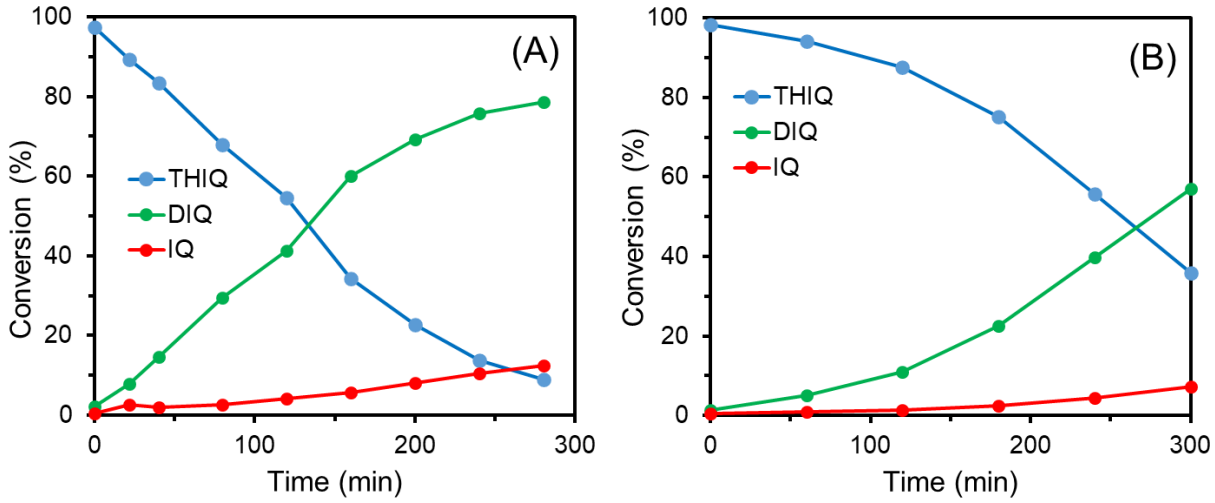

Figure S 5.5. Effect of ruthenium-based sensitizers on the reaction progress
Semi-oxidation of THIQ (0.125 M) in AcN in the presence of photosensitisers and irradiated with blue LEDi under O_2 atmosphere: (A) $Ru(bpy)_3Cl_2$ (0.01mM) and (B) RuB@GW (50 mg). Samples were analysed by GC-MS using tert-Butylbenzene as an external standard. Note that (A) is a homogeneous system, while (B) is heterogeneous.

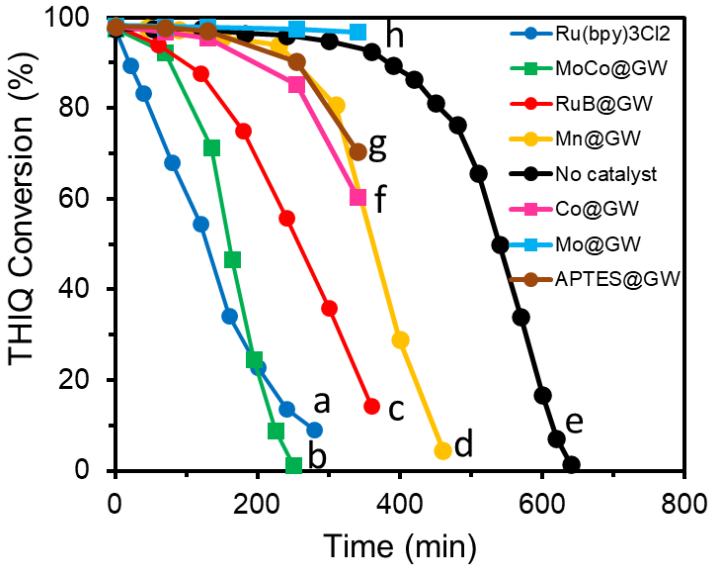

Figure S 5.6. Comparison of different photosensitizers reported in this contribution with a few others that were tested in preliminary experiments.
Semi-oxidation of THIQ (0.125M) in AcN using different photosensitisers. All samples were irradiated with blue LEDi under an O_2 atmosphere and analysed by GC-MS using tert-Butylbenzene as an external standard. (a) $Ru(bpy)_2Cl_3$, (b)MoCo@GW, (c)RuB@GW, (d)Mn@GW, (e) no catalyst, (f) Co@GW, (g)APTES@GW, (h) Mo@GW.

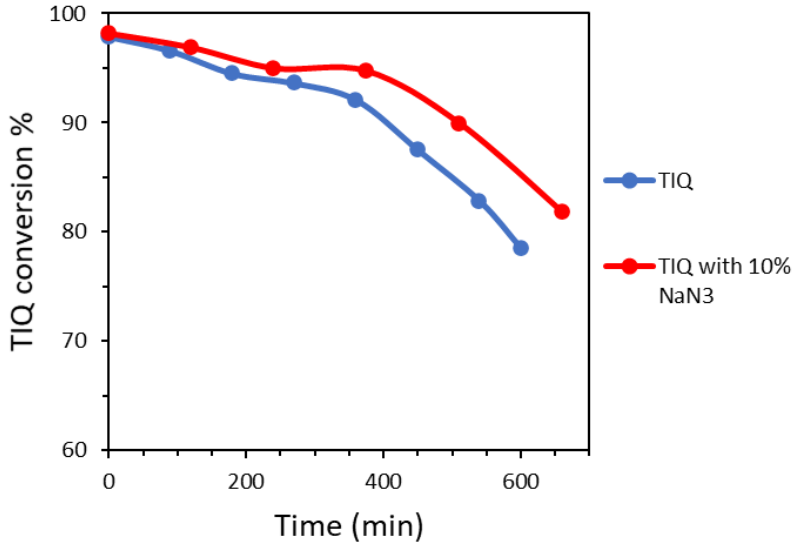

Figure S 5.7. Effect of NaN_3 (a singlet oxygen scavenger) on catalyst performance THIQ (0.125M) in methanol irradiated with blue LEDi (450 nm), samples were analysed with GC-MS. (blue) THIQ, (red) THIQ with 10 mol% NaN_3

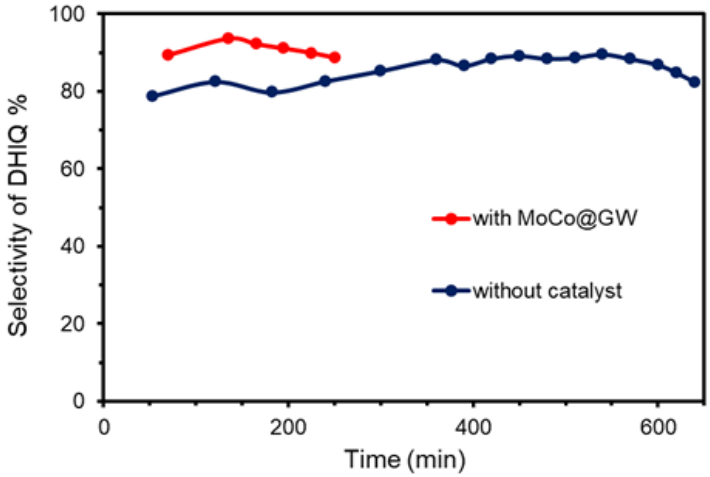

Figure S 5.8. Selectivity of DHIQ as a product of THIQ oxidation reaction by the time.

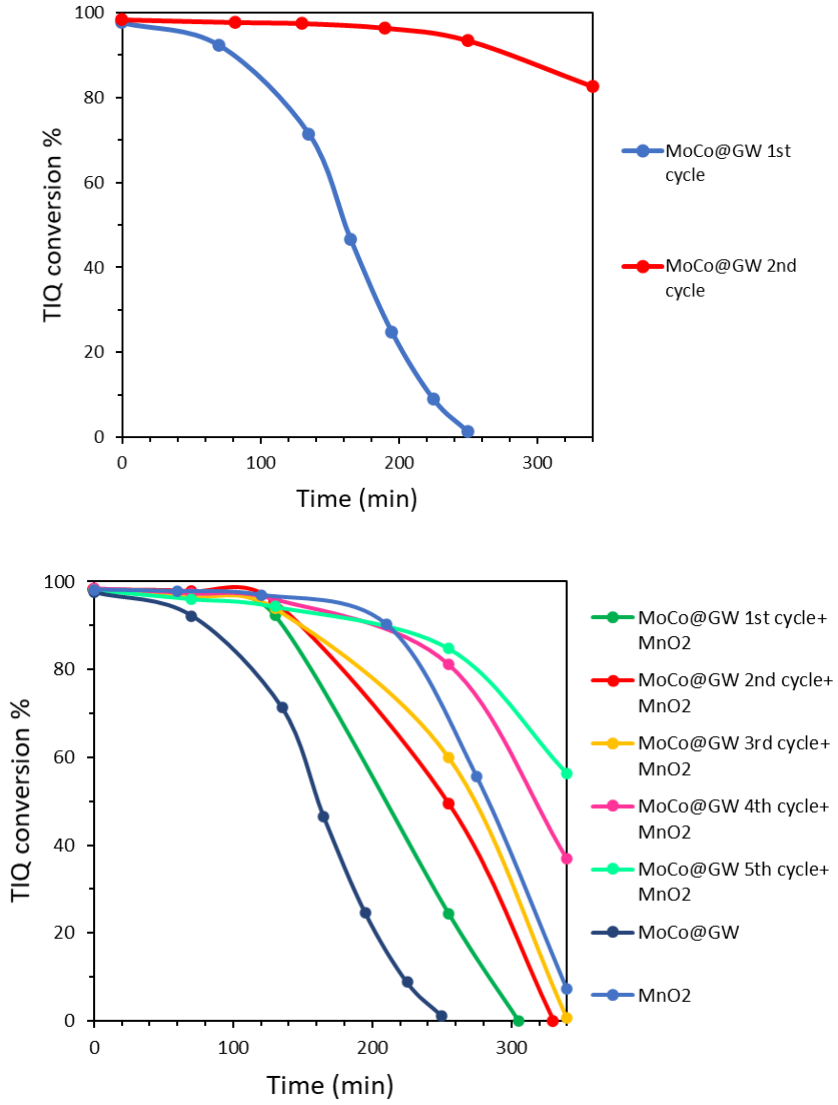

Figure S 5.9. Effect of added MnO2 on MoCo@GW performance and reusability.
All experiments were done with THIQ (0.125M) in AcN, oxygen atmosphere, irradiated with LEDi 450nm and samples analysed with GC-MS. (A) 2 cycles of MoCo@GW, (B) effect of adding MnO2 as a co-catalyst to preserve MoCo@GW for next cycles.

5.4 Accompaniment to Chapter

This study explores the selective semi-oxidation of tetrahydroisoquinoline (THIQ) to dihydroisoquinoline (DHIQ) through a singlet oxygen-mediated mechanism. The research combines bench-scale experiments with advanced spectroscopic techniques to elucidate the reaction pathway.

Key findings include the critical role of singlet oxygen in achieving high selectivity, due to the vast difference in reactivity between THIQ and DHIQ. The study demonstrates the effectiveness of both homogeneous and heterogeneous photocatalysts in generating singlet oxygen, with in-situ formation of isoquinoline (IQ) acting as an additional sensitizer.

Instrumentally, the research displays the combination of laser flash photolysis, near-infrared detection, chromatography, and materials characterization techniques can provide a comprehensive understanding of complex photochemical processes.

This work not only advances our understanding of selective oxidation processes but also highlights the potential of heterogeneous photocatalysts in sustainable organic synthesis. It provides valuable insights into combining photochemical principles with advanced analytical techniques to develop efficient and environmentally friendly synthetic processes.

5.5 References

(1) Wang, B.; Duke, K.; Scaiano, J. C.; Lanterna, A. E. Cobalt-Molybdenum Co-Catalyst for Heterogeneous Photocatalytic H-Mediated Transformations. *J. Catal.* **2019**, *379*, 33–38. https://doi.org/10.1016/j.jcat.2019.09.015.

(2) Alonso, F.; Osante, I.; Yus, M. Highly Stereoselective Semihydrogenation of Alkynes Promoted by Nickel (0) Nanoparticles. *Adv. Synth. Catal.* **2006**, *348* (3), 305–308. https://doi.org/10.1002/adsc.200505327.

(3) *Product Compare*. https://www.sigmaaldrich.com/CA/en/product/compare?term=isoquinoline&focus=products&page=1&perpage=30&sort=relevance&type=product&products=T13005%3AALDRICH%3Asial%2C779385%3AALDRICH%3Asial%2CI28208%3AALDRICH%3Asial (accessed 2024-08-30).

(4) Jayaraj, S.; Badu-Tawiah, A. K. N-Substituted Auxiliaries for Aerobic Dehydrogenation of Tetrahydro-Isoquinoline: A Theory-Guided Photo-Catalytic Design. *Sci. Rep.* **2019**, *9* (1), 11280. https://doi.org/10.1038/s41598-019-47735-y.

(5) Aganda, K. C. C.; Hong, B.; Lee, A. Aerobic α-Oxidation of N-Substituted Tetrahydroisoquinolines to Dihydroisoquinolones via Organo-Photocatalysis. *Adv. Synth. Catal.* **2019**, *361* (5), 1124–1129. https://doi.org/10.1002/adsc.201801301.

(6) Clark, J. L.; Hill, J. E.; Rettig, I. D.; Beres, J. J.; Ziniuk, R.; Ohulchanskyy, T. Y.; McCormick, T. M.; Detty, M. R. Importance of Singlet Oxygen in Photocatalytic Reactions of 2-Aryl-1,2,3,4-Tetrahydroisoquinolines Using Chalcogenorosamine Photocatalysts. *Organometallics* **2019**, *38* (12), 2431–2442. https://doi.org/10.1021/acs.organomet.9b00126.

(7) Elhage, A.; Wang, B.; Marina, N.; Luisa Marin, M.; Cruz, M.; E. Lanterna, A.; C. Scaiano, J. Glass Wool: A Novel Support for Heterogeneous Catalysis. *Chem. Sci.* **2018**, *9* (33), 6844–6852. https://doi.org/10.1039/C8SC02115E.

(8) Teixeira, R. I.; Lucas, N. C. de; Garden, S. J.; Lanterna, A. E.; Scaiano, J. C. Glass Wool Supported Ruthenium Complexes: Versatile, Recyclable Heterogeneous Photoredox Catalysts. *Catal. Sci. Technol.* **2020**, *10* (5), 1273–1280. https://doi.org/10.1039/C9CY02479D.

(9) Zhong, W.; Liu, M.; Dai, J.; Yang, J.; Mao, L.; Yin, D. Synergistic Hollow CoMo Oxide Dual Catalysis for Tandem Oxygen Transfer: Preferred Aerobic Epoxidation of Cyclohexene to 1,2-Epoxycyclohexane. *Appl. Catal. B Environ.* **2018**, *225*, 180–196. https://doi.org/10.1016/j.apcatb.2017.11.074.

(10) Quaranta, M.; Murkovic, M.; Klimant, I. A New Method to Measure Oxygen Solubility in Organic Solvents through Optical Oxygen Sensing. *Analyst* **2013**, *138* (21), 6243–6245. https://doi.org/10.1039/C3AN36782G.

(11) Turro, N. J.; Vaidhyanathan Ramamurthy; Juan C Scaiano. *Modern Molecular Photochemistry of Organic Molecules*; University Science Books, 2010; Vol. 188.

(12) Harbour, J. R.; Issler, S. L. Involvement of the Azide Radical in the Quenching of Singlet Oxygen by Azide Anion in Water. *J. Am. Chem. Soc.* **1982**, *104* (3), 903–905. https://doi.org/10.1021/ja00367a066.

(13) Wilkinson, F.; Brummer, J. G. Rate Constants for the Decay and Reactions of the Lowest Electronically Excited Singlet State of Molecular Oxygen in Solution. *J. Phys. Chem. Ref. Data* **1981**, *10* (4), 809–999. https://doi.org/10.1063/1.555655.

(14) Wilkinson, F.; Helman, W. P.; Ross, A. B. Rate Constants for the Decay and Reactions of the Lowest Electronically Excited Singlet State of Molecular Oxygen in Solution. An Expanded and Revised Compilation. *J. Phys. Chem. Ref. Data* **1995**, *24* (2), 663–677. https://doi.org/10.1063/1.555965.

(15) Kaluža, L.; Gulková, D.; Vít, Z.; Zdražil, M. Effect of Support Type on the Magnitude of Synergism and Promotion in CoMo Sulphide Hydrodesulphurisation Catalyst. *Appl. Catal. Gen.* **2007**, *324*, 30–35. https://doi.org/10.1016/j.apcata.2007.02.050.

(16) Ji, J.; Duan, X.; Qian, G.; Zhou, X.; Tong, G.; Yuan, W. Towards an Efficient CoMo/γ-Al2O3 Catalyst Using Metal Amine Metallate as an Active Phase Precursor: Enhanced Hydrogen Production by Ammonia Decomposition. *Int. J. Hydrog. Energy* **2014**, *39* (24), 12490–12498. https://doi.org/10.1016/j.ijhydene.2014.06.081.

(17) Small Jr., R. D.; Scaiano, J. C.; Patterson, L. K. Radical Process in Lipids. A Laser Photolysis Study of t-Butoxy Radical Reactivity toward Fatty Acids. *Photochem. Photobiol.* **1979**, *29* (1), 49–51. https://doi.org/10.1111/j.1751-1097.1979.tb09258.x.

(18) Wu, H.; Lian, K. The Development of Pseudocapacitive Molybdenum Oxynitride Electrodes for Supercapacitors. *ECS Trans.* **2014**, *58* (25), 67. https://doi.org/10.1149/05825.0067ecst.

(19) Zhang, L.; Wu, L.; Li, J.; Lei, J. Electrodeposition of Amorphous Molybdenum Sulfide Thin Film for Electrochemical Hydrogen Evolution Reaction. *BMC Chem.* **2019**, *13* (1), 88. https://doi.org/10.1186/s13065-019-0600-0.

(20) Biesinger, M. C.; Payne, B. P.; Grosvenor, A. P.; Lau, L. W. M.; Gerson, A. R.; Smart, R. St. C. Resolving Surface Chemical States in XPS Analysis of First Row Transition Metals, Oxides and Hydroxides: Cr, Mn, Fe, Co and Ni. *Appl. Surf. Sci.* **2011**, *257* (7), 2717–2730. https://doi.org/10.1016/j.apsusc.2010.10.051.

Chapter 6. Conclusion and future work

6.1 Summary and Future Directions

6.1.1 Nitro to amine reduction by using a heterogeneous catalyst in flow systems

Chapter two presents a novel, environmentally friendly method for reducing nitro compounds to amino using a heterogeneous catalyst, palladium on glass wool (Pd@GW). The process operates under remarkably mild conditions, room temperature, atmospheric pressure and using water as the main solvent in a flow system. This approach stands in stark contrast to current industrial methods that often require high temperatures and pressures.

We developed a photochemical method to synthesize the Pd@GW catalyst with a minimum amount of Pd, which can be prepared in situ within the flow reactor. This catalyst demonstrated excellent stability and reusability, maintaining its activity even after 8 months of storage and showing the ability to be regenerated through treatment with sodium borohydride.

A key achievement of this study was the successful scale-up of the process. Starting from batch reactions with a space-time yield of 0.08 $gL^{-1}h^{-1}$, then we scaled up to a flow system achieving yields up to 28 $gL^{-1}h^{-1}$. This scalability, combined with the use of either sodium borohydride or hydrogen gas as reducing agents, showcases the potential industrial applicability of the method.

The process is not limited to nitrobenzene; it proved effective for various other nitro compounds as well. Notably, the method uses a much lower catalyst loading (0.32 wt% Pd) compared to some current processes (up to 7 wt%), further enhancing its efficiency and potential cost-effectiveness.

Future work can be done by focusing on the next steps of amine products. In situ product utilization has emerged as a powerful strategy in flow chemistry, particularly for the synthesis and immediate use of reactive intermediates such as amines produced from nitro reductions. This approach offers several significant advantages over traditional batch processes, enhancing both the efficiency and safety of chemical synthesis.[1] One of the primary benefits of in situ utilization is the improved handling of sensitive intermediates. Many amines, especially primary aromatic

amines, are susceptible to air oxidation or prone to side reactions when isolated.[2] By using these amines immediately after formation, chemists can minimize degradation and unwanted reactions. For instance, notoriously unstable compounds like o-aminophenol or p-phenylenediamines can be swiftly converted to more stable derivatives, preserving their reactivity for desired transformations.[3]

Another impactful next step in this research could be extending the focus to the reduction of NO_x compounds, which are significant air pollutants contributing to smog formation, acid rain, and various health issues. Developing efficient NO_x reduction methods would have substantial environmental benefits.[4] NOx reduction plays a critical role in automotive catalytic converters, emissions control in power plants, and various industrial processes. Enhancing these technologies could yield wide-reaching implications.[5]

The catalytic systems and flow setups developed in this study for nitro reductions could potentially be adapted for NO_x reduction, offering novel and more efficient approaches. Key challenges will involve adapting flow reactors capable of handling gas-phase reactions or gas-liquid interactions required for NO_x reduction, investigating the use of flow catalysis to improve selective catalytic processes, utilizing ammonia or hydrocarbons as reducing agents, and developing precise analytical methods, such as thermal conductivity detectors (TCD), for product analysis.[6]

The direct utilization of amines in flow systems also leads to improved yields and product purity. By eliminating isolation and purification steps, the losses typically associated with these processes are significantly reduced. This streamlined approach often results in higher overall yields and purer final products, as the opportunities for side reactions or decomposition are minimized.[7]

Process intensification is another key advantage of in situ product utilization. By combining multiple synthetic steps into a single, continuous process, the overall efficiency of the synthesis is markedly improved. This integration leads to reduced reaction times, smaller reactor volumes, and potentially lower energy consumption, aligning well with the principles of green chemistry.[8]

Safety considerations also favour the in-situ approach, particularly when dealing with toxic or strong-smelling amines. By utilizing these compounds immediately after their formation, exposure risks for operators are minimized, and environmental concerns associated with the handling and storage of hazardous intermediates are significantly reduced.[9]

The implementation of in situ product utilization in flow chemistry represents a significant advance in synthetic methodology, offering a more efficient, safer, and potentially more environmentally friendly approach to complex chemical synthesis, particularly in the realm of amine chemistry.

6.1.2 Actinometry in a flow system

Chapter 3 introduces an advancement in flow photochemistry by developing a simple yet effective Norrish Type II actinometer based on valerophenone photochemistry. The research addresses a critical gap in current practice, where quantitative measurements of light absorption have been largely absent, leading to difficulties in determining quantum yields and comparing results across different laboratories.

The actinometer can be readily implemented in organic chemistry laboratories, requiring only standard equipment and materials. This accessibility should encourage the wider adoption of quantitative techniques in flow photochemistry. The system is adaptable to various UV-Vis light sources and flow reactor geometries, making it applicable to a broad range of experimental setups.

A key strength of this actinometer is its ability to measure both incident (I_0) and absorbed (I_a) light intensities, providing a complete picture of the photochemical process. By utilizing normalized lamp emission spectra and absorption spectra of samples and actinometer solutions, the method eliminates the need for specialized spectroradiometric equipment.

The effectiveness of the actinometer has been demonstrated through several case studies, including quenched valerophenone photolysis, benzoin photochemistry, and studies of the photoinitiator Irgacure-2959. These validations showcase the versatility and reliability of the method across different photochemical systems.

By providing a standardized method for measuring light absorption, this actinometer facilitates more meaningful comparisons of results between different research groups. The ability to accurately measure light absorption enables the calculation of quantum yields, a critical parameter in understanding and optimizing photochemical reactions.

Future work could focus on extending this approach to other spectral regions, developing actinometers for visible and near-infrared light, and integrating this quantitative approach into automated flow chemistry platforms. As the field of flow photochemistry continues to evolve, tools like this actinometer will be crucial in ensuring that it develops on a solid quantitative foundation.

6.1.3 Scalable synthesis of silver nanoparticles

The photochemical synthesis of silver nanoparticles (AgNPs) under flow conditions has demonstrated remarkable efficiency and reproducibility. This innovative approach yields high-quality AgNP seeds under UVB irradiation with remarkably short exposure times, less than one minute for the most effective photoinitiators. Our research has identified that the most suitable initiators are those that efficiently produce ketyl radicals through Norrish Type I cleavage.

Among the photoinitiators tested, I-2959, I-184, and D-1173 emerged as the standout performers. These compounds exhibit optimal absorption properties, and adequate aqueous solubility, and are readily available, making them an ideal choice for scaled-up production. These characteristics not only enhance the efficiency of the synthesis process but also contribute to its potential for industrial application.

The AgNP seeds produced through this method serve as versatile precursors, potentially enabling the synthesis of nanoparticles with diverse morphologies. This versatility opens up exciting possibilities for tailoring nanoparticles to specific biological applications, where shape and size play crucial roles in determining functionality.

Expanding the flow synthesis method to other noble metals and bimetallic nanoparticles presents an exciting frontier for future research. This approach could be adapted to produce gold, platinum, and palladium nanoparticles, each with unique properties and applications.

Gold nanoparticles (AuNPs), known for their distinctive optical properties, are widely used in biomedical applications, catalysis, and sensing. Adapting the flow synthesis method to reduce Au (III) salts like $HAuCl_4$ to Au (0) could offer new avenues for AuNP production. However, this may require adjusting the reaction conditions to account for gold's different reduction potential compared to silver. The resulting AuNPs could then be compared to those produced by traditional methods.[10]

This method could be extended to produce bimetallic nanoparticles. Combining two metals in a single nanoparticle can lead to synergistic properties not found in monometallic nanoparticles. Examples could include Ag-Au, Pt-Pd, or Au-Pd nanoparticles. The flow synthesis method could be adapted to introduce two metal precursors simultaneously or sequentially, allowing for precise control over the composition and structure of the bimetallic nanoparticles. Each metal will likely require optimization of reaction conditions, including choice of photoinitiator, solvent system, and irradiation parameters. The different reduction potentials of various metals may necessitate the exploration of new photoinitiators.

6.1.4 Photosensitized selective semi-oxidation

Chapter 5 presents a significant advancement in the selective semi-oxidation of tetrahydroisoquinoline (THIQ) to dihydroisoquinoline (DHIQ), a valuable intermediate in organic synthesis. The research illuminates a highly efficient and selective process mediated by singlet oxygen, offering a sustainable pathway to produce DHIQ.

The key to exceptional selectivity lies in the dramatic difference in reactivity towards singlet oxygen between THIQ and DHIQ. THIQ quenches singlet oxygen at a rate of 2.63×10^7 $M^{-1}s^{-1}$, while DHIQ reacts at least 1000 times slower. This substantial difference allows the reaction to effectively "stop halfway," avoiding over-oxidation to isoquinoline (IQ) even at high conversion rates.

The study explores both homogeneous and heterogeneous catalysts, with the latter showing particular promise for practical applications. Heterogeneous catalysts such as RuB@GW and MoCo@GW, supported on glass wool, demonstrate excellent performance in reducing the reaction's induction period and maintaining high selectivity. These catalysts offer the additional

advantages of easy separation, reusability, and compatibility with flow photochemistry systems, paving the way for potential scale-up and continuous production processes.

Mechanistic investigations, including laser flash photolysis with NIR detection, solvent studies, and deuterium effect experiments, provide compelling evidence for the singlet oxygen mechanism. The research also reveals an interesting autocatalytic aspect, where small amounts of IQ formed during the reaction act as in-situ singlet oxygen sensitizers, accelerating the process.

The use of molecular oxygen as the oxidant, coupled with visible light irradiation and recyclable heterogeneous catalysts, aligns this process with principles of green chemistry and sustainable synthesis. The ability to selectively produce DHIQ, which is significantly more valuable than both its precursor (THIQ) and its over-oxidation product (IQ), underscores the economic potential of this methodology.

Future work could focus on further optimizing the heterogeneous catalysts, exploring the potential of flow chemistry for continuous production, and extending this approach to other substrates where selective partial oxidation is desirable.

Investigating the scalability of the selective oxidation process of THIQ to DHIQ for potential industrial applications is a crucial next step in developing this research. This scale-up study would involve several interconnected aspects to bridge the gap between laboratory success and industrial implementation. The first challenge would be reactor design. Developing larger-scale photoreactors that can handle increased volumes while maintaining efficient light distribution is essential. Creating a flow reactor with internal illumination to optimize light penetration, steady mixing, more control on temperature, and continuous oxygen delivery could offer advantages in terms of scalability and process control.

6.1.5 Flow set-up

The flow setup employed in these studies (Chapters 3 and 4) demonstrates a versatile and efficient system for photochemical reactions. At its core, the setup consists of a Luzchem’s Expo panel with 8W fluorescent, or LED lamps (30 cm long, 16 mm diameter) tightly wrapped with thin wall Teflon tubing (1.80 mm outer diameter, 1.50 mm inner diameter). This configuration,

utilizing about 6.3 m of Teflon tubing, creates a total irradiated volume of approximately 10 mL per lamp with an experimentally determined optical path of 0.15 cm.

This system's efficiency in delivering photons to the reaction mixture is evident from the rapid conversion rates observed in both studies. Its versatility is demonstrated by its compatibility with different light sources (UV-Vis) and various solvents, enabling a wide range of photochemical reactions at lower temperatures. The setup's scalability is a notable advantage, allowing for continuous production with the potential for scaling up by employing multiple lamps or longer tubing, double-wrapped. Additionally, the flow system provides consistent results over extended periods, as shown in the nanoparticle synthesis study, highlighting its reproducibility. The precise actinometry capabilities further enhance its utility by enabling quantitative analysis of light absorption and reaction efficiency.

The reliability and versatility of this setup for multi-step reactions have been further validated through a successful collaboration with a chemical company to prepare vitamin D analogs. This project demonstrated significant improvements over traditional methods that had been in use for two decades. The flow system enabled the production of the purest isomers, which was not achievable with the previous lab procedure. It also provided enhanced control over product selectivity, improved energy efficiency, and significantly increased safety. This last point is particularly noteworthy, as the previous method, using a high-pressure lamp had resulted in a laboratory fire some years ago. The flow system's design inherently mitigates such risks. While the specifics of this industry collaboration remain confidential due to its nature, the success of the project underscores the potential of this setup for industrial applications and process improvements.

While this thesis is used primarily for single-step photochemical reactions, this setup shows promising potential for adaptation into multi-step flow systems. By connecting multiple lamp-wrapped tubing sections in series, each with different reagent inputs, it could be possible to perform sequential photochemical reactions. The system could also be expanded to include non-photochemical reaction steps between photochemical stages, such as mixing chambers or heating/cooling sections. The current incorporation of in-line UV-Vis spectroscopy could be extended to include other analytical techniques for real-time monitoring of multi-step processes.

The simplicity of the setup lends itself to an adjustable design, where different reaction stages can be easily added or removed.

However, adapting this system for multi-step processes would require addressing several challenges. More sophisticated pumping systems might be needed to precisely control residence times in different reaction stages. Ensuring compatibility of reagents and products across multiple steps could be challenging and may require careful optimization. Multiple photochemical steps might necessitate additional cooling mechanisms. We successfully overcame these challenges in our industrial collaboration project.

In conclusion, the current setup efficiency, versatility, and simplicity make it a promising platform for developing more complex, multi-step flow systems. With appropriate modifications and careful design, it could be adapted to perform a wide range of sequential photochemical and non-photochemical reactions, opening new possibilities in flow chemistry and continuous manufacturing processes. The successful application in the vitamin D analog project further demonstrates its potential for industrial-scale use and process improvement. This potential for expansion and adaptation, coupled with its proven industrial applicability, positions the system as a valuable tool for advancing research and applications in photochemistry and flow reaction technology.

6.2 Conclusion

These four studies collectively demonstrate the power and versatility of photochemistry, particularly when combined with flow systems, in advancing various areas of chemical synthesis and analysis. From the reduction of nitro compounds to amines using Pd@GW, to the development of a flow actinometer, the scalable synthesis of silver nanoparticles (AgNPs), and the selective semi-oxidation of tetrahydroisoquinoline (THIQ) to dihydroisoquinoline (DHIQ), these works display how photochemical approaches can address diverse challenges in organic synthesis, and nanomaterial production.

A common thread throughout these studies is the use of heterogeneous catalysts supported on glass wool, such as Pd@GW, and MoCo@GW. These catalysts offer significant advantages in terms of ease of separation, reusability, and compatibility with flow systems. The glass wool

support proves to be a versatile platform for various catalytic materials, enabling efficient photocatalytic processes across different types of reactions.

The development of the flow actinometer addresses a critical need in quantitative flow photochemistry, providing a tool for accurately measuring light absorption, a key parameter often overlooked in photochemical reactions. This advancement enables more precise control and understanding of photochemical processes in flow systems.

The scale-up of AgNP synthesis in flow conditions demonstrates the potential for continuous production of nanomaterials, highlighting the scalability of photochemical processes when adapted to flow systems. This approach offers improved control over particle size and morphology, crucial factors in nanomaterial applications.

In all cases, the use of flow systems enhances reaction efficiency, improves reproducibility, and facilitates potential scale-up. The continuous nature of flow reactions allows for better control of reaction parameters, more efficient light utilization, and often shorter reaction times compared to batch processes.

Moreover, these studies align with principles of green chemistry by utilizing visible light, employing recyclable catalysts, and in some cases using molecular oxygen as an oxidant. The ability to perform selective transformations, such as the semi-oxidation of THIQ or the controlled reduction of nitro compounds, underscores the precision achievable with photochemical methods.

In conclusion, these works illustrate how the integration of photochemistry with flow systems and heterogeneous catalysis can lead to more efficient, scalable, and sustainable chemical processes. They make the way for further advancements in continuous-flow photochemistry, potentially revolutionizing various aspects of chemical synthesis, from organic molecule transformations to nanomaterial production. Future research in this area could focus on optimizing catalyst designs and developing more sophisticated flow systems to tackle even more challenging chemical transformations.

6.3 References

(1) Plutschack, M. B.; Pieber, B.; Gilmore, K.; Seeberger, P. H. The Hitchhiker's Guide to Flow Chemistry. *Chem. Rev.* **2017**, *117* (18), 11796–11893. https://doi.org/10.1021/acs.chemrev.7b00183.

(2) Wirth, T. *Microreactors in Organic Chemistry and Catalysis*; John Wiley & Sons, 2013.

(3) Baumann, M.; Baxendale, I. R. The Synthesis of Active Pharmaceutical Ingredients (APIs) Using Continuous Flow Chemistry. *Beilstein J. Org. Chem.* **2015**, *11* (1), 1194–1219. https://doi.org/10.3762/bjoc.11.134.

(4) Skalska, K.; Miller, J. S.; Ledakowicz, S. Trends in NOx Abatement: A Review. *Sci. Total Environ.* **2010**, *408* (19), 3976–3989. https://doi.org/10.1016/j.scitotenv.2010.06.001.

(5) Gómez-García, M. A.; Pitchon, V.; Kiennemann, A. Pollution by Nitrogen Oxides: An Approach to NOx Abatement by Using Sorbing Catalytic Materials. *Environ. Int.* **2005**, *31* (3), 445–467. https://doi.org/10.1016/j.envint.2004.09.006.

(6) Forzatti, P. Present Status and Perspectives in De-NO*x* SCR Catalysis. *Appl. Catal. Gen.* **2001**, *222* (1), 221–236. https://doi.org/10.1016/S0926-860X(01)00832-8.

(7) Gutmann, B.; Cantillo, D.; Kappe, C. O. Continuous-Flow Technology—A Tool for the Safe Manufacturing of Active Pharmaceutical Ingredients. *Angew. Chem. Int. Ed.* **2015**, *54* (23), 6688–6728. https://doi.org/10.1002/anie.201409318.

(8) Vaccaro, L.; Lanari, D.; Marrocchi, A.; Strappaveccia, G. Flow Approaches towards Sustainability. *Green Chem.* **2014**, *16* (8), 3680–3704. https://doi.org/10.1039/C4GC00410H.

(9) Movsisyan, M.; Delbeke, E. I. P.; Berton, J. K. E. T.; Battilocchio, C.; Ley, S. V.; Stevens, C. V. Taming Hazardous Chemistry by Continuous Flow Technology. *Chem. Soc. Rev.* **2016**, *45* (18), 4892–4928. https://doi.org/10.1039/C5CS00902B.

(10) Saha, K.; Agasti, S. S.; Kim, C.; Li, X.; Rotello, V. M. Gold Nanoparticles in Chemical and Biological Sensing. *Chem. Rev.* **2012**, *112* (5), 2739–2779. https://doi.org/10.1021/cr2001178.

Appendix

Journal permissions

This dissertation includes manuscripts and images that have been republished with permission from the original publishing journals.